Universidad de Huelva

Departamento de Física Aplicada

Near barrier scattering of ^{8}He from heavy targets

Dispersión de ^{8}He en núcleos pesados a energías en torno a la barrera de Coulumb

Memoria para optar al grado de doctora
presentada por:

Gloria Marquínez Durán

Fecha de lectura: 5 de febrero de 2016

Bajo la dirección de los doctores:

Ismael Martel Bravo

Ángel Miguel Sánchez Benítez

Huelva, 2016

Universidad de Huelva

DISPERSIÓN DE ^{8}He EN NÚCLEOS PESADOS A ENERGÍAS EN TORNO A LA BARRERA DE COULOMB

Gloria Marquínez Durán

Tesis doctoral

2016

Universidad de Huelva

NEAR BARRIER SCATTERING OF ^{8}He FROM HEAVY TARGETS

Gloria Marquínez Durán

PhD Thesis

2016

Universidad de Huelva

DISPERSIÓN DE ^{8}He EN NÚCLEOS PESADOS A ENERGÍAS EN TORNO A LA BARRERA DE COULOMB

Gloria Marquínez Durán

Tesis doctoral

Programa de doctorado: "Tecnología e Instrumentación Nuclear"

2016

Directores:

Ismael Martel Bravo
Departamento de Física Aplicada
Universidad de Huelva

Ángel Miguel Sánchez Benítez
Departamento de Física Aplicada
Universidad de Huelva

Prólogo

La presente tesis recoge los resultados obtenidos del estudio de la dispersión elástica del núcleo ^{8}He en un blanco de ^{208}Pb a energías en torno a la barrera de Coulomb ($\sim$19 MeV).

El ^{8}He es el más ligero de los denominados núcleos "skin" y tiene el mayor ratio de neutrones a protones del núcleos estables frente a la emisión de partículas. Comparado con el ^{6}He, estudiado previamente por la colaboración de la que el Grupo de Estructura de la Materia de la Universidad de Huelva forma parte, el ^{8}He tiene más neutrones de valencia pero se encuentra más fuertemente ligado. Las energías de ligadura para $1n$ y $2n$, S_n y S_{2n} respectivamente, son similares, mientras que en el caso del ^{6}He los procesos $2n$ se encuentran energéticamente favorecidos. Se espera que las diferencias entre ambos isótopos de Helio se reflejen en las secciones eficaces elásticas y de reacción, obtenidas a partir de la dispersión con núcleos pesados a energías cercanas a la barrera.

La dipersión de ^{8}He en núcleos pesados a energías en torno a la barrera coulombiana no ha sido estudiada en profundidad y, actualmente, sólo algunos conjuntos de datos están disponibles. Existe todavía falta de información en lo referente a aspectos colectivos como el acoplamiento entre distintos canales de reacción. Teniendo en cuenta que S_n y S_{2n} son similares, es importante investigar la competición entre las transferencias de uno y dos neutrones y el mecanismo de ruptura directa. Además, falta información acerca de los potenciales ópticos que describen la dispersión elástica así como su dependencia con la energía.

Como consecuencia del interés y las peculiaridades del ^{8}He, se llevó a cabo el experimento E587S en GANIL (Caen, Francia) en 2010, con el objetivo de estudiar su estructura y dinámica a través del proceso de colisión con un blanco de ^{208}Pb a dos energías, 22 y 16 MeV, por encima y por debajo de la barrera respectivamente.

A continuación, se presenta una breve descripción de los contenidos de la presente tesis.

El capítulo 1 contiene una introducción a las reacciones nucleares y al estudio de núcleos exóticos y su producción, enfatizando en los núcleos ligeros y ricos en neutrones. Se presta especial atención al núcleo de ^{8}He, al ser el objeto de estudio de la tesis. Se

resumen además algunos trabajos previos realizados en torno a la barrera y se presenta la propuesta del experimento E587S. Se incluye además información básica acerca de los modelos teóricos empleados para la interpretación de las distribuciones angulares experimentales.

El procedimiento experimental de las medidas llevadas a cabo en el experimento E587S se explica en el capítulo 2, comenzando con la producción de haces exóticos en SPIRAL-GANIL. La sección 2.2.1 se dedica concretamente al diseño del sistema de detección. Las secciones siguiente contienen una descripción del blanco, la electrónica analógica y la adquisición de datos empleada durante el experimento.

El capítulo 3 se dedica al análisis de datos. La sección 3.1 presenta el proceso seguido para obtener los espectros que, adecuadamente calibrados, permiten la identificación de los eventos elásticos y de los fragmentos de reacción. En la sección 3.2 se describen algunas correcciones experimentales mientras que la sección 3.3 se dedica a la determinación de la posición efectiva del haz en el blanco y del sistema de detección, con el objetivo de asignar correctamente los ángulos de dispersión y ángulos sólidos. Finalmente, en las secciones 3.4 y 3.5 se muestra como calcular el ratio entre la sección eficaz elástica y la sección eficaz de Rutherford y como calcular los ratios ^{6}He/^{8}He y ^{4}He/^{8}He respectivamente.

En el capítulo 4 se realiza una interpretación teórica de los resultados. En 4.2 se estudia la sección eficaz elástica a través del Modelo Óptico y de cálculos CRC. En las secciones 4.3 y 4.4 las distribuciones angulares de los ratios ^{6}He/^{8}He y ^{4}He/^{6}He se estudian en base a cálculos DWBA (del inglés Distorted Wave Bron Approximation).

Finalmente, en el capítulo 5 se presenta un resumen de la tesis junto a las conclusiones más importantes.

Preface

The present thesis reports the results obtained from the study of the scattering of the nucleus ^{8}He from the heavy target ^{208}Pb at energies around the Coulomb barrier ($\sim$19 MeV).

^{8}He is the lightest skin nucleus and has the largest neutron-to-proton ratio of the particle-stable nuclei. Compared with ^{6}He, previously studied by the collaboration in which the Grupo de Estructura de la Materia of the University of Huelva takes part, ^{8}He has more valence neutrons, but is more tightly bound. The binding energies for $1n$ and $2n$, S_n and S_{2n} respectively, are similar, whereas in the ^{6}He nucleus the $2n$ processes are energetically favoured. The differences between both helium isotopes are expected to be reflected in the elastic and reaction cross sections obtained for the scattering from heavy targets at near-barrier energies.

The scattering of ^{8}He from heavy targets at Coulomb barrier energies has not been deeply studied and only a few data sets are available. There is still a lack of information concerning collective aspects as the coupling between reaction channels. Since S_n and S_{2n} are similar, it is important to investigate the competition between the single and double neutron transfer channels and the direct breakup. Also, basic information about the optical potentials for describing the elastic scattering, as well as their dependence on energy, is missing.

As a consequence of the interest and peculiarities of ^{8}He, the experiment E587S was performed at GANIL (Caen, France) in 2010 with the aim of studying its structure and dynamics through the collision process with a ^{208}Pb target at energies of 22 and 16 MeV, above and below the barrier respectively.

In the following, a brief description of the contents of the present thesis dissertation is presented.

Chapter 1 contains an introduction to nuclear reactions and the study of exotic nuclei and their production, emphasising the light and neutron rich nuclei. Special attention is paid to the ^{8}He nucleus, as it is the object of study of this work. Some previous works at energies around the barrier are also summarized together with the proposal for the experiment E587S. Basics about the theoretical models used for the

interpretation of the experimental angular distributions are also presented.

The experimental procedure of the measurements performed in the experiment E587S is explained in chapter 2, starting with the production of exotic beams at SPIRAL-GANIL. Section 2.2.1 is specially dedicated to the design of the detection system. The next sections contain a description of the target, the analogue electronics and data acquisition used during the experiment.

Chapter 3 is dedicated to the data analysis. Section 3.1 presents the process followed to obtain the spectra which, adequately calibrated, allows for the identification of elastic events as well as reaction fragments. Some experimental corrections are described in section 3.2. Section 3.3 is devoted to the determination of the effective position of the beam spot on target and of the detection system, in order to properly assign scattering and solid angles. Finally, section 3.4 shows how the normalised cross section and its uncertainty are calculated while section 3.5 is dedicated to the calculation of the ^{6}He/^{8}He and ^{4}He/^{8}He ratios.

In chapter 4 a theoretical interpretation of the experimental results is presented. Section 4.2 is devoted to the study of the elastic cross sections by means of the Optical Model and Coupled Reaction Channels (CRC) calculations. In sections 4.3 and 4.4 the angular distributions of the ratios ^{6}He/^{8}He and ^{4}He/^{6}He are studied through DWBA (Distorted Wave Bron Approximation) calculations.

Finally, in chapter 5 a summary of the thesis is presented together with the most important conclusions.

Contents

1 Introduction

This first chapter is dedicated to introduce the exotic nuclei and, among them, those which exhibit an extended distribution of the valence nucleons and the influence of their characteristics in the reactions they induce. Also, some basics about nuclear reactions and the more relevant concepts about the models used for the interpretation of experimental results are included.

More in detail, section 1.1 presents the atomic nucleus and some basics about nuclear reactions. Section 1.2 is referred to the production of exotic beams and the principal production techniques available nowadays. In section 1.3, an overview of the experimental studies at the driplines is presented. Section 1.4 introduces the halo and skin nuclei while in section 1.5 the most relevant experimental evidences of nuclear halos are summarized.

Section 1.6 treats the specific case of the nucleus of ^{8}He, emphasising in its peculiar structure. Some previous works on ^{8}He are presented in 1.6.1 where it becomes clear that the scattering of ^{8}He with heavy targets at energies around the Coulomb barrier has been surprisingly not deeply studied. Regarding the interesting features of this nucleus, the proposal of experiment which gave rise to this work is also commented.

In section 1.7, the principles of the theoretical models used for the description of nuclear reactions are presented.

1.1 The atomic nucleus and nuclear reactions

The atomic nucleus gathers all the positive charge of the atom, and almost the totality of the atomic mass, in a region with characteristic dimensions of the order of femtometres (1 fm = 10^{-15} m) while the electrons, negatively charged, are found orbiting the nucleus at distances of about 10^{-10} m, thus determining the atomic dimensions. The nucleus consists of A nucleons (Z protons and N neutrons) held together by the strong nuclear force, a short range interaction which compensates the repulsion between the protons due to the Coulomb interaction.

Only some particular combinations of Z and N numbers make a particular nuclide

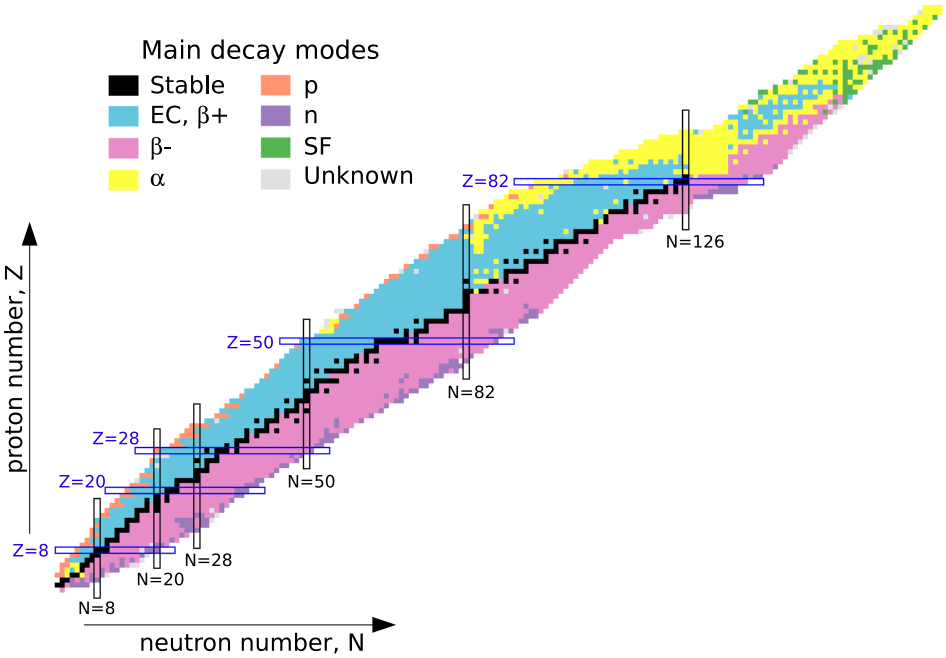

Figure 1.1: *The chart of nuclei. Black squares represent the stable nuclides while the rest of isotopes are depicted in different colours, where each colour represents the most probable type of decay [1].*

particle-emission stable. Nowadays, 256 stable nuclides are known. Other configurations give rise to unstable species which in principle are considered as well defined elements when their half-life is bigger than 10^{-21} seconds [2]. Through radioactive decays these nuclides reach the stability.

A great number of unstable nuclei has been synthesized and studied in laboratories worldwide and up to now around 3000 species have been identified or characterized [3]. All existing nuclides can be represented in a bidimensional plot known as Chart of Nuclei (Fig. 1.1), where the horizontal and vertical axis represent the number of neutrons and protons respectively. The limits of the particle-stability region are defined by the driplines. Driplines are located in the frontier in which the separation energy for one proton S_p (for the left drip line or proton drip line) or one neutron S_n (right or neutron drip line) becomes negative. This cannot be understood as a definition as there are species for which the energy separation for two nucleons is smaller than for one nucleon. In fact, it is more applicable for the neutron drip line than for the proton one, where phenomena as the proton and two-proton radioactivity appear. Exotic nuclei allow for the study of properties which are well established for stable nuclei and which validity should be explored near the drip lines.

One of the most important tools for studying and producing nuclei are nuclear reactions. When to particles collide, many different processes may occur [4]. The most general way to express a nuclear reaction, when only two particles are present in the final partition is the following:

$$A + a \rightarrow B + b \quad \text{or} \quad A(a,b)B, \tag{1.1}$$

where A stands for the target nucleus, a for the projectile, B for the residual nucleus and b is the observed particle. B, b, or both, may be left in an excited state, in which case, it is indicated by B^* or b^*. The energy released during the reaction, Q, can be calculated as the kinetic energy of the particles after the reaction (E_f) minus the energy before the reaction (E_i). The Q-value can be positive (exothermic reaction), negative (endothermic) or zero. Different types or reactions are possible:

- Elastic scattering. In this case $b = a$ and $B = A$, so no internal changes are produced and the Q-value of the reaction is zero. The energy is the same before and after the reaction. As an example:

$$^6He +^{208} Pb \rightarrow^6 He +^{208} Pb \;\; \text{or} \;\; ^{208}Pb(^6He,^6 He)^{208}Pb$$

- Inelastic scattering. B, b or both are raised to an excited state and, consequently, $Q = -E$, where E is the energy needed to excite the particles. For example:

$$^{12}C +^{208} Pb \rightarrow^{12} C^* +^{208} Pb^* \;\; \text{or} \;\; ^{208}Pb(^{12}C,^{12} C^*)^{208}Pb^*$$

- Transfer reactions. Here $b \neq a$ and $B \neq A$ due to an exchange of nucleons between the target and the projectile. As an example, the transfer of two neutrons from ^{8}He to ^{208}Pb is shown:

$$^8He +^{208} Pb \rightarrow^6 He +^{210} Pb \;\; \text{or} \;\; ^{208}Pb(^8He,^6 He)^{210}Pb$$

- Capture reactions. A and a fuse in a compound nucleus, generally in an excited state, which is subsequently desexcited by emitting one ore more gamma rays. For example:

$$p +^{197} Au \rightarrow^{198} Hg + \gamma \;\; \text{or} \;\; ^{197}Au(p,\gamma)^{198}Hg$$

- Fusion-evaporation reactions. In this case A and a fuse in a compound nucleus which is desexcited by emitting particles. For example:

$$^8He +^{208} Pb \rightarrow^{216} Po \rightarrow^{212} Po + 4n \;\; \text{or} \;\; ^{208}Pb(^8He, 4n)^{212}Po$$

- Break-up reactions. In this case, the projectile, generally weakly bound, is broken into two or more fragments due to the electromagnetic and nuclear field created by the target nucleus.

In Fig. 1.2 (top), a scheme is shown where the possible collisions between nuclei have been classified based on the impact parameter, b, which can be defined as the perpendicular distance to the closest approach if the projectile were undeflected. The classical angular momentum of the relative motion projectile-target is the product of the impact parameter and the linear momentum p of the relative motion. Hence, the same reactions can be represented in terms of the angular momentum transfer associated with each mechanism as it can be observed in Fig. 1.2 (bottom).

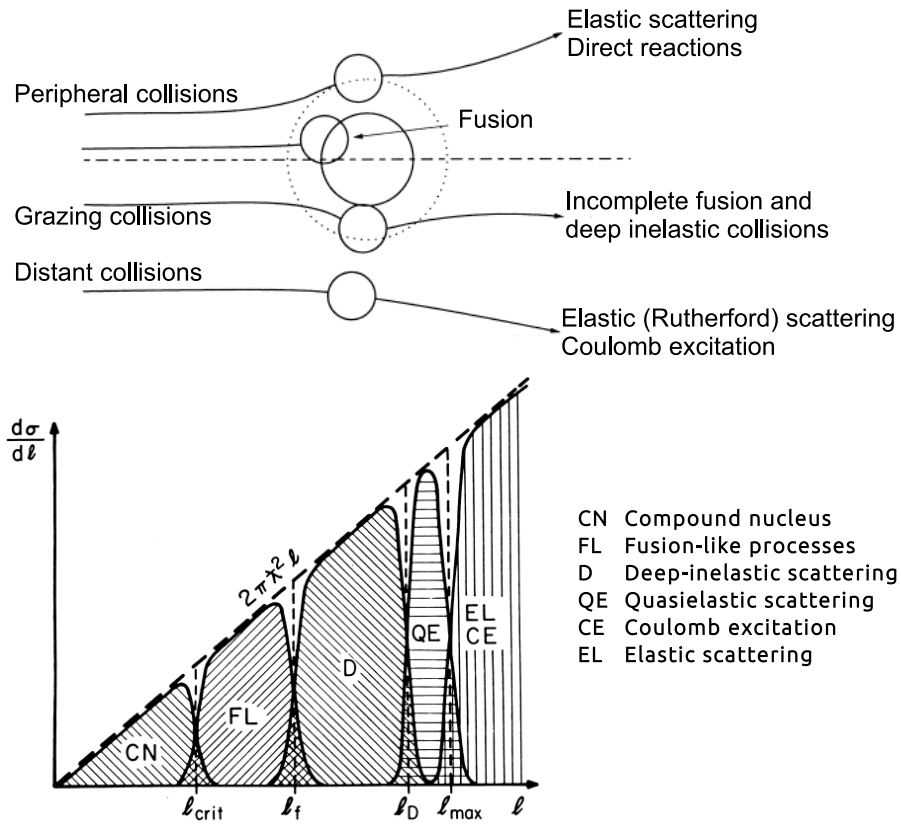

Figure 1.2: *(Top) Classification of the possible nuclear collisions based on the impact parameter. (Bottom) Same mechanisms represented in terms of the relative angular momentum. The peripheral and distant collisions produce elastic scattering and Coulomb excitation and the highest values of angular momentum transfer. Grazing collisions are responsible of inelastic scattering and incomplete fusion or nucleon exchange (known in general as quasielastic reactions) and intermediate values of momentum transfer. For impact parameters between grazing and head-on collision, it is found the deep-inelastic scattering. The head-on collisions, which produce compound nucleus, correspond to the lowest values of angular momentum transfer [5].*

The particles usually involved in a nuclear reaction (except neutrons) are positively charged and the Coulomb interaction make them to repeal each other. At large distances, this interaction plays a major role on the probability of those particles to undergo a reaction. In the other hand, if they are close enough, the strong and attractive nuclear interaction acts, overtaking the Coulomb interaction.

Some basic characteristics of reactions between heavy ions may be understood in terms of a central interaction potential $V(r)$, where r is the distance between the centre of mass of the two colliding nuclei. $V(r)$ consists of both a coulombian and a nuclear contribution, as shown in Fig. 1.3. As the nuclear potential begins to act, the total potential $V(r)$ reaches a maximum, then decreasing and becoming attractive. This maximum is known as the Coulomb barrier for the two interacting nuclei. The colliding nuclei must approach sufficiently for the nuclear reaction to occur. In particular, they must overcome the Coulomb barrier within a classical picture. The scheme in Fig. 1.3 refers to the case in which the orbital angular momentum of the system l is zero. In

the case of $l \neq 0$, a centrifugal potential should be added to $V(r)$, giving rise to what is called a centrifugal barrier. The centrifugal barrier is effectively equivalent to an increase in the height and thickness of the barrier.

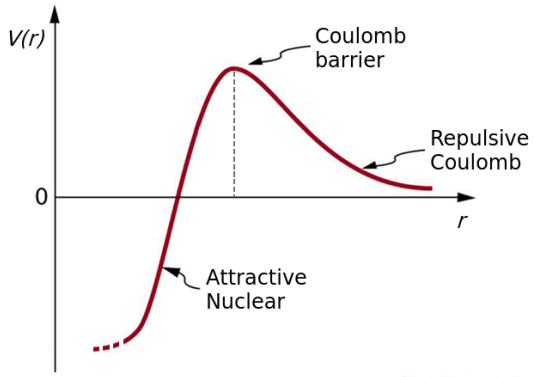

Figure 1.3: *Overall potential $V(r)$ between two colliding nuclei and schematic representation of the Coulomb barrier for angular momentum $l = 0$ (no centrifugal contribution).*

1.2 Production of exotic beams

The methods of production of exotic nuclei are based mainly on nuclear reactions. Once produced, the exotic nucleus can be studied or even used as a projectile in order to study collisions with other nuclei. In general, a new nucleus can be formed by different processes [2] like fusion of two nuclei followed by the emission of nucleons and radiation (fusion-evaporation), transfer of nucleons between the projectile and the target (multinucleon transfer) or other mechanisms as fragmentation, spallation or fission. The fusion-evaporation process is especially useful in the production of neutron-deficient species, while multinucleon transfer has been used to produce nuclides in the neutron-rich region. Transfer and fusion reactions are also used in order to produce superheavy nuclei. The nuclear fragmentation originates in a high energy collision between two heavy nuclei which undergo a process of nuclear rupture into several fragments. If one of these nuclei is a light ion, like a proton, the process is known as spallation. In both, fragmentation and spallation, almost any nucleus with Z and N smaller than those of the two nuclei involved can be produced. Fission produces necessarily neutron-rich fragments due to the large neutron to proton ratio of fissioning nuclei.

In the production process of radioactive nuclei, many different species are usually formed and consequently, a method to select the nucleus of interest is needed. In general, for the production of exotic beams, two complementary methods are used, as shown in Fig. 1.4: the Isotopic Separation On-Line (ISOL) and the In-Flight Separation (IFS) technique.

In an ISOL facility, a primary beam from a driver accelerator irradiates a thick target producing the nuclei of interest, which diffuse out of the target towards the ion source. From the source, the different ions are extracted. A mass separation must

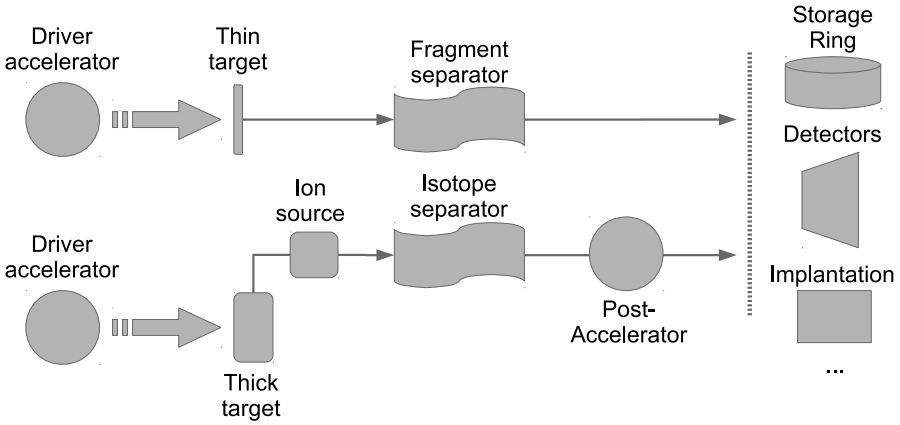

Figure 1.4: *Basic methods of producing radioactive beams: (Up) In-flight technique and (down) ISOL technique.*

be carried out using the mass-charge ratio. Once the ions of interest are separated they are post-accelerated. The main advantage of the ISOL technique is the high yield of radioactive nuclei produced, which is a consequence of the use of thick targets and light beams as primary beams, as they can be produced with high intensities. However, this technique is limited by the so-called release time or time passed between the moment in which the radioactive species are produced and the moment of their extraction from the source. For this reason, only those species with a mean life of the order of milliseconds or more are produced in ISOL facilities.

In the In-Flight method, a primary heavy beam impinges on a thin target producing radioactive nuclei by fragmentation or fission. The kinetic energy of the reaction products, already ionised, is of the same order of magnitude than the primary beam and, thus, large enough to escape from the target. However, the reaction fragments are produced with a large momentum spread. As much as possible of the beam is introduced in a fragment separator (analysing magnet) where a particular isotope is selected. The energy after the separator is usually high enough and no post-acceleration is needed [6], even though, it depends on the experiment. Unlike the ISOL technique, this method allows for the study of very short lived nuclei.

1.3 Experimental studies at the driplines

For the study of dripline nuclides, different experiments are usually performed in order to obtain as much information as possible, information that has to be properly combined to extract relevant nuclear properties. In Fig. 1.5 a summary of the experimental data commonly used to obtain information about exotic nuclei is presented. Due to the low intensities achievable with radioactive beams in comparison to stable beams, a remarkable effort has been made in order to develop new experimental techniques.

The experiments carried out in order to study elastic scattering and obtain interaction and reaction cross sections provide information about nuclear size and density distributions. These are important properties used in order to establish nuclear po-

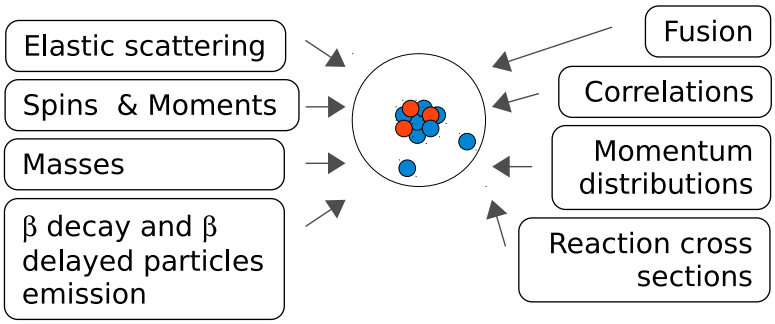

Figure 1.5: *Experimental data commonly used for obtaining nuclear properties.*

tentials or single particle configurations [7].

The development of radioactive beams allowed for the determination of nuclear sizes for unstable species, mainly through the measurements of interaction cross sections. Owing to those experiments, halo and skin structures, which are described in the next section, were discovered near the driplines [8, 9]. It was observed how common properties of the nucleon density in stable nuclei were not valid for exotic ones. The measurement of nucleon removal cross sections can provide more information about the wave function of the valence nucleon in halo-like nuclei [10]. Removal cross sections provide a measure of the total breakup yield, giving information about the structure [11]. In-depth information on nuclear matter distributions can be obtained from proton scattering at energies of about several hundred MeVs, due to the existence of a formalism which can correlate differential cross sections and matter distributions [12].

The measurement of the momentum distribution of fragments produced in the breakup of radioactive beams provides information which in certain cases indicates the presence of halo structures [13] as, in general, a narrower momentum distribution should correspond to a nucleon with a wider density distribution.

Near the driplines a gradual reduction of the binding energy of nucleons and clustering phenomena may produce β-delayed particle emission or particle radioactivity, when the nucleon separation energy becomes negative. These processes provide information about decay properties difficult to obtain from reaction studies and constitute a meaningful tool to study nuclear structure [2, 14].

Ground state properties such as mass, binding energy, spin or moments, which are important observables for the study of nuclear structure, can be determined by using stopped low-energy beams generally at ISOL facilites [15]. Laser spectroscopy techniques are helpful in the determination of nuclear spin, moments and charge radii. Mass spectrometers have been developed within the last years, as ISOLTRAP or MISTRAL at ISOLDE, for mass measurements of short-live isotopes.

In general, when moving away from stability, the nuclear structural features change in comparison with nuclides near the valley of stability. As it has been mentioned, the reduction of binding energy produces β-delayed particle emission or particle radioactivity. Moreover, in these regions, new magic numbers replace the ones valid for stable nuclei [16]. New phenomena as neutron halos and skins appear as the asymmetry between the number of neutrons and protons increases. In the next section, a more complete description of halo and skin structures is presented.

1.4 Halo and skin nuclei

The first evidences of the existence of halo nuclei were described by Tanihata *et al.* [8] in 1985, during systematic measurements of interaction cross sections and nuclear radii in the light *p*-shell region. In these studies, the case of the neutron rich isotope ^{11}Li was presented, which showed a similar size to the heavy nucleus ^{197}Au. It was observed that, as it had been later suggested [17], ^{11}Li could be described as a ^{9}Li nucleus and two weakly bound neutrons orbiting far from the core. Later, the halo structure has been found in isotopes of He, Li, Be and some other light nuclei.

The most important feature of the halo nuclei is its spatial extension, abnormally large compared to stable nuclei. The wave function must have a cluster structure in such a way that they can be described as an internal core and one or more nucleons making up the halo. These nucleons have a wave function extending out of the classically allowed region, more than stable nuclei. In Fig. 1.6 an schematic comparison of the sizes of ^{208}Pb, ^{48}Ca and ^{11}Li is shown.

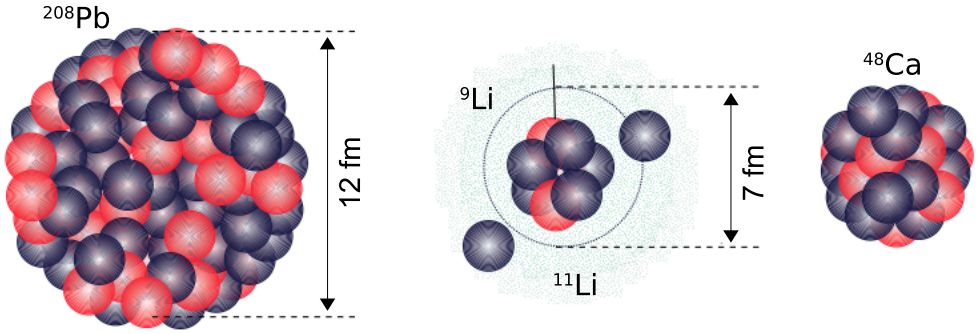

Figure 1.6: *Comparison in size among one of the most studied halo nucleus ^{11}Li and the isotopes ^{48}Ca and ^{208}Pb [18]. The RMS (Root Mean Square) matter radius is similar for ^{11}Li and ^{48}Ca and the radius for the neutrons in the halo is comparable to the more external neutrons in ^{208}Pb.*

Halo nuclei are weakly bound systems. This characteristic is reflected in the value of the energy separation for the nucleons in the halo, below 2 MeV, much less than the typical 8 MeV shown by stable nuclei [1]. Due to the low binding energy of the valence nucleons, halo nuclei have a few or no bound excited states. For this reason, very little information can be obtained from gamma spectroscopy. Therefore, further information should be extracted from the angular distributions of the fragments produced in the collision with other nuclei or from the study of its β decay.

Among halo nuclei, regarding to the two-body interactions, there are four possible situations for a general n-n-core system [19], as shown in Fig. 1.7. In this figure, n stands not only for a neutron, but some other nuclear three-particle interactions can be considered, whenever two of the three particles are identical. The four configurations are:

- Borromean: both n–n and n–core subsystems are unbound, with virtual-state energies.

- Samba: only the n-core subsystem is bound.
- Tango: while the n-n subsystem is bound, the n-core is virtual.
- All-bound: both n-n and n-core subsystems are bound.

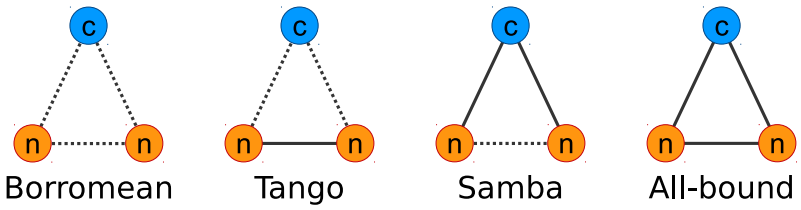

Figure 1.7: *Schemes for the four possible configurations of a n-n-core system, according to the nature of two body interactions.*

For neutron halo nuclei, the all-bound and tango configurations are just hypothetical. The samba configuration is observed, for example in ^{20}C, while a borromean structure is present for example in ^{6,8}He and ^{11}Li.

Making a clear distinction between halo and skin nuclei represents a difficult task. Tanihata *et al.* proposed in [10] to differentiate both kind of nuclei taking as a parameter the slope of the tail of the density distribution, which is related to the separation energy. In [7] this idea is summarized describing the neutron skin as an excess of neutrons in the surface and the neutron halo as not only this excess but also a tail of the neutron density distribution. Comparing the values of 0.3 and 0.5 MeV corresponding to ^{11}Li y ^{11}Be respectively, with the value for ^{8}He, 2.13 MeV, the term skin seems more appropriate for this helium isotope. For the loosely bound nucleons, the wavefunction extends beyond the nuclear potential, behaving as $e^{-\eta r}/r$ where $(\hbar\eta)^2 = 2mB$ being B the binding potential and m the mass of the nucleon, in such a way that for smaller values of B, the wavefunction extends for larger values of the radius. The halo structure in unstable exotic nuclei is then a consequence of the small binding energy of the last nucleons, in comparison with stable nuclei.

1.5 Experimental evidences of nuclear halos

There are various experimental ways to probe and characterize nuclear halos. The combination of information from different experiments gives a more complete picture of them. Due to their extended mass distribution and weakly bound structure, the behaviour of halo nuclei is very different from the behaviour of stable and tightly bound nuclei. In this section, a set of experimental evidences of nuclear halos, found so far, are briefly presented.

- **Interaction cross section.** [8, 9, 10] For halo nuclei, as ^{11}Li, ^{11}Be and to a lesser extent, ^{8}He or ^{6}He, the measured interaction cross sections show a clear enhancement suggesting a large spatial extension. In table 1.1, interaction cross

sections of He isotopes with different targets are shown. Strong interactions between nucleons make them "shadow" each other so, in more compact systems, reduced cross sections will arise.

Target	^{3}He	^{4}He	^{6}He	^{8}He
Be	498±4	485±4	672±7	757±4
C	550±5	503±5	722±6	817±6
Al	850±9	780±13	1063±8	1197±9

Table 1.1: *Interaction cross sections (σ_1) of He isotopes (in mb) from [9].*

- **Momentum distributions in fragmentation reactions with light targets.** [13, 20, 21] A narrow momentum distribution of a nucleon can be regarded as an indication of a halo structure. Measurements of transverse momentum distribution of fragments with halo projectiles as ^{11}Be, ^{11}Li or ^{6}He, turn to be narrower than the ones obtained for stable nuclei. This phenomenon appears as a consequence of Heisenberg's uncertainty principle, whereby it can be understood that a nucleon with a wider density distribution, as it happens in halo nuclei, shows a narrow momentum distribution.

  As an example, in Fig. 1.8 the moment distribution of ^{9}Li fragments from the reaction ^{11}Li (at 800 MeV/nucleon) + C $\rightarrow$ ^{9}Li + X, reported in [22] is shown. As it can be observed, two Gaussians functions are needed for fitting the experimental data, taking into account that the momentum distribution of the projectile-fragments originated in peripheral collisions with heavy ions are well described by Gaussians [23]. The first Gaussian fits the wide peak which involves tightly bound nucleons while the second one fits the narrow peak, corresponding to weakly bound nucleons, i.e. those forming the halo.

- **Coulomb dissociation with heavy targets.** [20, 24] The electromagnetic dissociation (EMD) or Coulomb breakup is also an interesting tool for studying unstable nuclei. EMD occurs due to an excitation of the projectile in the field created by the target. The comparison between the interaction cross sections of halo nuclei on light and heavy targets shows an important enhancement of the EMD cross sections in the case of heavy targets. This effect can be understood as a consequence of the intense electric field created by the target which produces the displacement of the core and the neutrons in the halo in opposite directions. In this way it is generated an intense coupling with the dipole modes of the system at relatively low excitation energies, known as E1 soft mode.

  These effects are amplified at energies around the Coulomb barrier, where the characteristic time of the collision process is comparable with the required time for exciting the collective degrees of freedom and the coupling to the continuum.

- **Elastic scattering.** The elastic scattering cross section of halo nuclei differs substantially from the Rutherford cross section. It gives information about the long tail of the halo nucleon density or the coupling to virtual states and shows signatures of long-range reaction mechanisms.

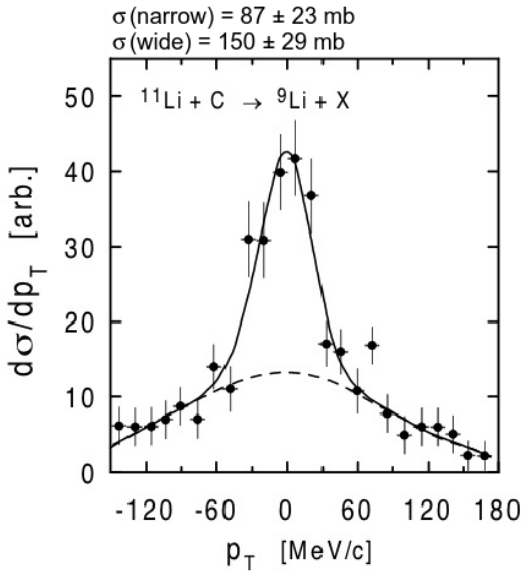

Figure 1.8: *Transverse momentum distribution of* ^{9}Li *fragments from the reaction* ^{11}Li *(at 800 MeV/nucleon) +* $C \rightarrow {}^{9}Li + X$*. From [22].*

In this context, it is important to mention the Coulomb rainbow. This typical feature of the angular distribution of the elastic cross section at energies around the barrier, completely disappears in the case of the scattering of halo nuclei owing to the strong coupling to relevant reaction channels. This effect clearly appears in the scattering of light halo systems like ^{6}He [25, 26, 27].

- β **decay.** The well known β decay mechanism can be used as a test for halo structure, providing useful information complementary with the results collected from nuclear reactions [28]. From β decay measurements, the structure of dripline nuclei ^{6,8}He, ^{9,11}Li, ^{14}Be and ^{17}Ne has been studied [29]. The special structure of these nuclei affects the β decay in different ways:

  - The spatial overlap with daughter states could be reduced by the extension of the halo.
  - The core and the nucleon(s) in the halo can decay independently. If the halo is largely extended, the decay might go directly to continuum states, as it has been observed, for example, in the case of the β delayed deuteron emission from ^{6}He [30].

- **Fusion.** Fusion studies have been carried out in order to understand the influence of the weakly bound structure of halo nuclei on fusion cross sections. An enhancement of this cross section can be expected due to the large radii and coupling to low lying resonant states. However, the influence of the breakup channels has been controversial as it could enhance the fusion cross section or decrease it. In [31], it has been found that the coupling to breakup channels enhance cross sections below the Coulomb barrier, while, for energies above, it induces a reduction.

1.6 The ^{8}He nucleus

The ^{8}He nucleus is located in the region of light nuclei in the nuclide chart, at the right side of the valley of stability, where the neutron-rich isotopes can be found (Fig. 1.9). Among the lightest bound nuclei, ^{8}He has the biggest neutron to proton ratio (N/Z) and it is the lightest skin nucleus.

Figure 1.9: *Region of the nuclide chart corresponding to the lightest nuclei.*

The peculiar structure of ^{8}He has attracted the interest of the scientific community in the last years. However, the availability of data related to the elastic scattering at energies around the Coulomb barrier is limited. From previous works [32, 33], excitation functions are known, but angular distributions of the elastic channel and the cross sections for the transfer of 1 and 2 neutrons are available only up to 60° in the laboratory frame. There is also a lack of information about collective aspects as the coupling between reaction channels and some basic information about the optical potentials for the elastic scattering and their dependence with energy is still missing.

For the ^{8}He nucleus, the distinction between transfer channels (1 and 2 neutrons) is difficult. In addition, the fact that the valence neutrons are weakly bound could imply a large cross section for both transfer and breakup processes. From previous works it is known that larger cross section values are found for transfer [32, 33].

The already known resonances for ^{8}He are shown in Fig. 1.10 and summarized in table 1.2. The half-life for the ground state is 119.1 ms, it doesn't have bound excited states and, principally, it decays to ^{8}Li by β^{-}.

E_{level} (MeV)	$J\pi$	$T_{1/2}$ o Γ	Decay mode
0	0+	119.1(*12*) ms	$\beta^{-} = 100\%$; $\beta^{-}n = 16(1)\%$
3.1(*5*)	2+	0.6(*2*) MeV	$n \approx 100\%$; $\alpha < 5\%$
4.36(*20*)	(1-)	1.3(*5*) MeV	$n \approx 100\%$
(6.03(*10*))		0.15(*15*) MeV	
7.16(*4*)	(3-)	0.1(*1*) MeV	

Table 1.2: *Excited states of ^{8}He [1].*

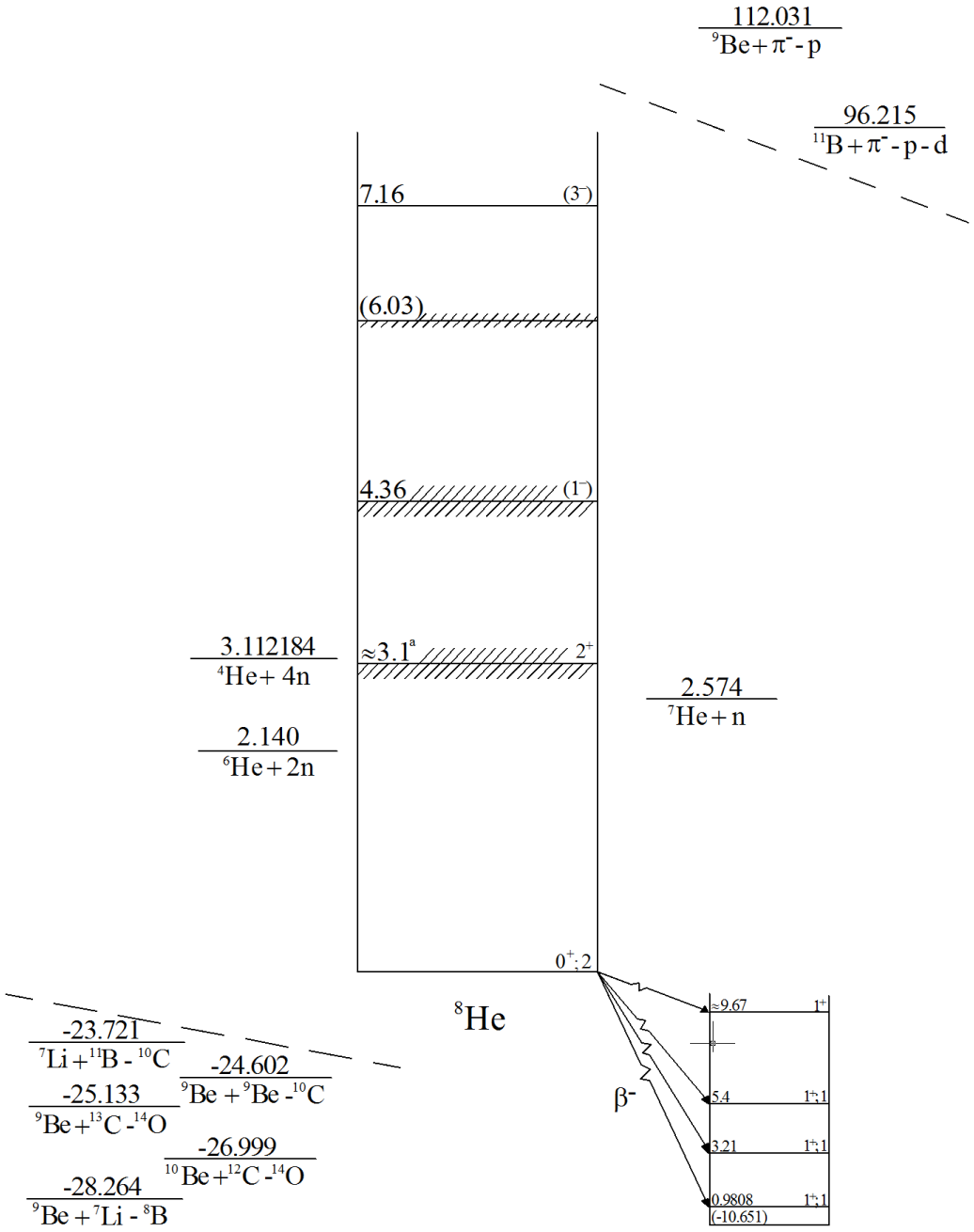

Figure 1.10: ^{8}*He energy level diagram from [34]. Energy values are expressed in MeV, taking the ground state as origin.*

The study of ^{8}He is presented as part of the scientific program carried out by the Grupo de Estructura de la Materia of the University of Huelva, which have already performed experimental studies about reactions induced by ^{6}He on heavy targets at energies around the Coulomb barrier [26, 25, 35]. From the results obtained in the study of ^{8}He, and by comparison with the available data of ^{6}He, the differences and similarities between halo and skin nucleus can be analysed.

The direct comparison between ^{8}He and ^{6}He reveals that the neutron layer is thicker for the first one, being, on top, more tightly bound (Table 1.3). The RMS radius for

the neutron distribution is a 53% larger than for protons, showing the existence of a thick neutron skin [10]. Regarding the energy separation for 1 and 2 neutrons, it can be noticed that, for ^{6}He, S_{1n} is larger than S_{2n}, so that the transfer or breakup of two neutrons are favoured. In the case of ^{8}He, S_{1n} and S_{2n} have similar values (Table 1.4), which can be regarded as a competence between mechanisms. Moreover, the difference in the charge radius for ^{6}He and ^{8}He can be interpreted as a change in the correlations between valence neutrons. It is expected that these differences related to spatial extension and separation energies for the neutrons in the halo/skin, will be reflected in the elastic and reaction cross sections.

Nucleus	R_n (fm)	R_p (fm)	R (fm)
^{4}He	1.63±0.03	1.63±0.03	1.63±0.03
^{6}He	2.59±0.04	1.72±0.04	2.33±0.04
^{8}He	2.69±0.04	1.76±0.03	2.49±0.03

Table 1.3: *RMS radius for protons, neutrons and total for the helium isotopes ^{4}He, ^{6}He y ^{8}He [10].*

Nucleus	S_{1n} (keV)	S_{2n} (keV)
^{6}He	1710.0 *20*	974.8 *4*
^{8}He	2529.0 *8*	2125.8 *5*

Table 1.4: *Separation energies for one and two neutrons for ^{6}He and ^{8}He [10].*

Usually, it is considered that the ^{4}He+4n structure for ^{8}He is the most probable. The possibility of having a ^{6}He+2n structure is lower according to the weak binding energy of ^{6}He as shown e.g. in [36]. More arguments in favour of the α plus four neutrons as the most significant configuration for ^{8}He are found in [10], where the relation between the interaction cross section and the particle-removal cross section, developed by Y. Ogawa et al. at [37], is used. The interaction cross section (σ_I) is defined as the reaction cross section (σ_R) minus the inelastic scattering cross section (σ_{inel}), where σ_R is given by the total cross section (σ_t) minus the elastic scattering cross section (σ_{el}). The inelastic scattering here is defined as the excitation of the nucleus to its bound excited states without emission of nucleons. Following the relations in [37], ^{6}He can be described as a ^{4}He core and 2 neutrons so that the interaction cross sections for ^{6}He and ^{4}He and the two neutrons removal cross section are related as follows:

$$\sigma_{-2n}(^6He) = \sigma_I(^6He) - \sigma_I(^4He), \tag{1.2}$$

where $\sigma_{-2n}(^6He)$ is the two-neutron removal cross section and it is assumed that the wave function for ^{6}He in the ground state can be expressed as:

$$\psi(^6He) = \psi(^4He)\psi(1,2), \tag{1.3}$$

being $\psi(^4He)$ and $\psi(1,2)$ the wave functions for the core and the neutrons in the halo, respectively. Using the cross sections for a ^{6}He beam at 800 MeV/u impinging on a carbon target [9], in Ref. [10] the expression 1.2 is evaluated obtaining two comparable values:

$$\begin{aligned} &\sigma_{-2n}(^6He) = 189 \pm 14\ mb, \\ &\sigma_I(^6He) - \sigma_I(^4He) = 219 \pm 8\ mb, \end{aligned} \tag{1.4}$$

Doing the same operation for ^{8}He, considering a ^{6}He+2n structure, it results:

$$\begin{aligned} &\sigma_{-2n}(^8He) = 202 \pm 17\ mb, \\ &\sigma_I(^8He) - \sigma_I(^6He) = 95 \pm 9\ mb. \end{aligned} \tag{1.5}$$

The difference between the two values in Eq. 1.5 reveals that ^{6}He is not a proper candidate for being the core of ^{8}He. On the other hand, considering ^{8}He as an alpha surrounded by four neutrons in the halo, the following values are obtained:

$$\begin{aligned} &\sigma_{-2n}(^8He) + \sigma_{-4n}(^8He) = 297 \pm 19\ mb, \\ &\sigma_I(^8He) - \sigma_I(^4He) = 314 \pm 8\ mb. \end{aligned} \tag{1.6}$$

In view of the results, it can be deduced that ^{8}He is better described as a central subsystem, ^{4}He, around which the valence neutrons are orbiting. In this approach, it has been taking into account that ^{5}He and ^{7}He are not bound systems.

The data obtained in the experiment reported in [38] is also well described considering ^{8}He as a α+4n system. In this work, the experimental and theoretical results for the scattering of ^{8}He+^{12}C at 60 MeV/nucleon are presented. As the experimental resolution is not enough for resolving the ground and low-lying states in ^{12}C, the angular distribution of the cross section should be considered quasielastic. A phenomenological analysis, based on the few-body eikonal model, where the colliding system is regarded as an α+4n+target six-body problem, is in good agreement with the experimental results (Fig. 1.11).

In [39], a cluster orbital shell model approximation (COSMA) has been generalized to a five-body case (α+4n) in order to describe the ground state wave function of ^{8}He. The calculation of the spatial angular correlations of the four valence neutrons shows that the three configurations with maximum probability are the ones shown in Fig. 1.12.

In [40], arguments in favour of a ^{6}He+2n structure for ^{8}He are given, where it is assumed that the properties of the ^{6}He cluster inside ^{8}He are different from those of a free ^{6}He, since it is concluded that a shrinking of ^{6}He is produced when two extra neutrons are added.

However, the ground state configuration of ^{8}He is still an open question. The $(1p_{3/2})^4$ configuration for the valence neutrons seems to be the most probable as shown

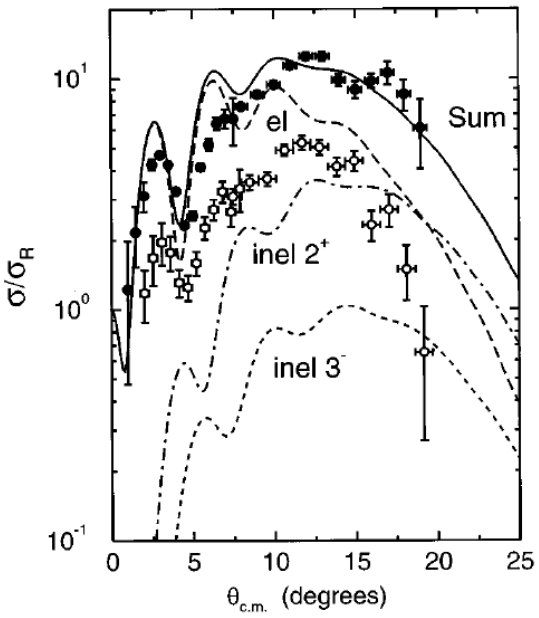

Figure 1.11: *The solid points represent the angular distribution of the experimental cross section for* ^{8}He+^{12}C *at 480 MeV. For comparison, the experimental cross section for the system* ^{9}Li+^{12}C *at the same incident energy per nucleon is shown by the open points, suggesting a noticeable difference in projectile-target interactions. The curve labelled as "el" represent the elastic calculation through the analysis based on the few-body eikonal model. On the other hand, the curves labelled as "inel" represent DWBA calculations carried out in order to include the inelastic excitations of the* ^{12}C *target to its* 2^+ *and* 3^- *states. Finally, the solid curve is the sum of previous curves and it reproduces reasonably the experimental data [38].*

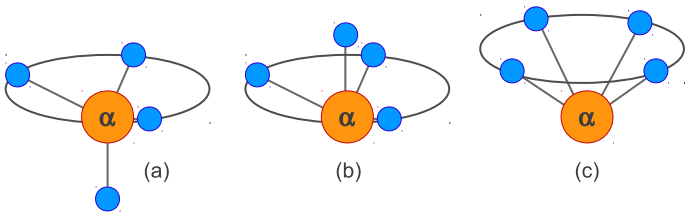

Figure 1.12: *Geometrical configurations for the most probable spatial angular correlations of the four valence neutrons in* ^{8}He. *Configuration (a) shows the most symmetrical position of neutrons in space, while (b) is more alike to* ^{4}n *and (c) configuration resembles* ^{4}n *or a pair of "dineutrons".*

in [41] where, nevertheless, it is considered that valence neutrons can be found in other configurations as $(1p_{3/2})^2(1p_{1/2})^2$ (pointed out in [40]).

In Fig. 1.13, the density distribution for ^{8}He (left) and the density distributions for protons and neutrons in ^{8}He (right) are shown. The neutron layer extends beyond the proton layer indicating the existence of the neutron skin. Moreover, despite having considered ^{4}He as the central subsystem of ^{8}He, the density distributions for ^{4}He and the ^{8}He core are not equal due to the movement of the core with respect to the center of mass of the nucleus. The curves in Fig. 1.13 have been parametrized

using phenomenological distributions, in particular GG (Gaussian-Gaussian) and GO (Gaussian-Oscillator), in which the nuclear density is factorized into the density of the core (ρ_c) and the density of the halo (ρ_h) respectively [42].

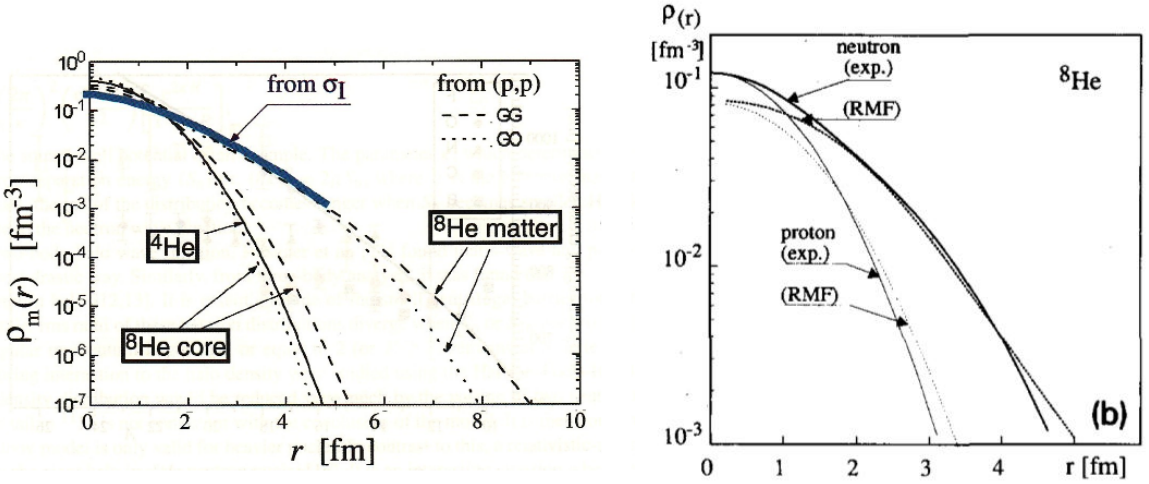

Figure 1.13: *Density distribution of ^{8}He (left) and density distributions for protons and neutrons in ^{8}He (right). Figures from [10].*

1.6.1 Previous works on ^{8}He near the Coulomb barrier

The system ^{8}He+^{208}Pb has been studied at 26 MeV in GANIL (Caen, France) [43], where gamma rays from direct and fusion-evaporation reactions have been observed. A gated γ-ray spectrum for ^{212}Po, produced in the strongest fusion-evaporation channel at 26 MeV, ^{208}Pb(^{8}He,4n)^{212}Po, together with a gated γ-ray spectrum for ^{209}Pb, which is the evidence of neutron-pickup reactions, are shown in Fig. 1.14. A cross section of about 500 mb is reported for the most probable fusion-evaporation channel. In addition, the population of low-spin states in ^{209}Pb suggest a strong one-neutron transfer channel. The cross sections for both reactions turn out to be comparable, being around two times larger for fusion-evaporation.

Later, also at GANIL, reactions induced by ^{4,6,8}He on medium and heavy targets have been measured in [44]. In particular, elastic scattering data of the colliding system ^{8}He+^{63}Cu at an incident energy of 27 MeV is presented in an angular range from 15° to 50° c.m. (Fig. 1.15). By fitting the angular distribution of the elastic cross section for ^{8}He+^{63}Cu, a total reaction cross section of 1862 mb has been obtained. This value is large in comparison with the value for the scattering of ^{4}He on the same target, making evident the weakly bound nature of ^{8}He. The coincidences between charged particles and gamma rays indicate a large production of ^{64}Cu, consistent with neutron transfer mechanisms.

In [33, 45] a stack of ^{197}Au targets separated by Al foils has been bombarded with ^{8}He beams at 18.7, 20.1 and 29.4 MeV at GANIL producing ^{198,198m,199}Au by one or more neutron transfer and Tl isotopes by complete fusion. In [33], the authors claim for a first model independent estimation for the lower limit of the ratio σ_{2n}/σ_{1n}, consid-

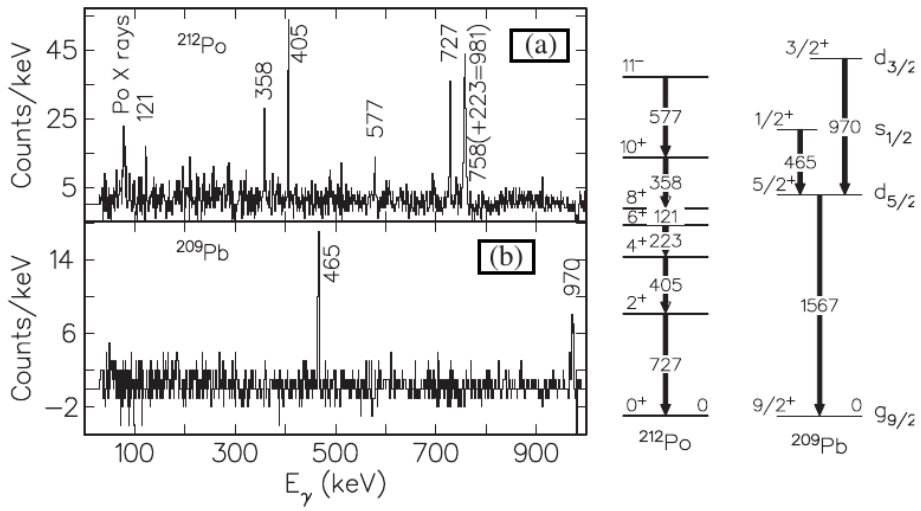

Figure 1.14: *Gated γ-ray spectra for (a) ^{212}Po produced in fusion-evaporation reactions and (b) ^{209}Pb from neutron-pickup reactions from [43]. The partial level schemes are also shown.*

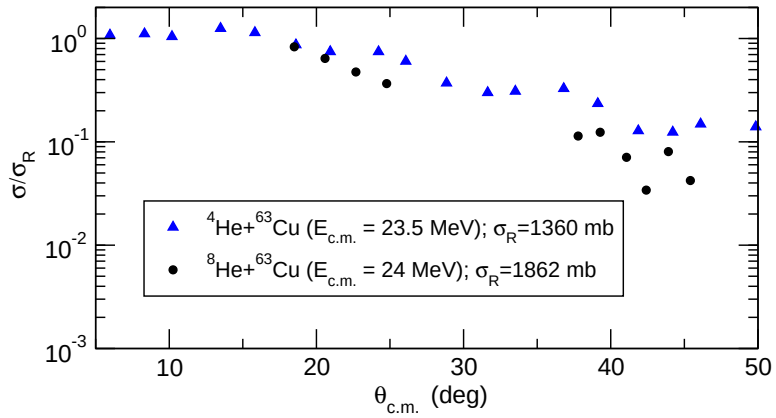

Figure 1.15: *Angular distributions for the elastic channels for the systems ^{8}He+^{63}Cu and ^{4}He+^{63}Cu from [44].*

ering that the sum of the cross section for producing each gold isotope must be equal to $\sigma_{2n}+\sigma_{1n}$. ^{198}Au can be produced by both 1n- and 2n- transfer and ^{198m,199}Au just by two-neutron transfer. In Fig. 1.16 lower limits on σ_{2n}/σ_{1n} for different bombarding energies are presented. Also in this study, a comparison between the total transfer cross section for ^{6}He and ^{8}He is presented, showing comparable values at energies close to the barrier and a larger cross section for ^{8}He above the barrier. Moreover, in [45] the complete fusion process is studied. Fusion and neutron transfer (σ_f,σ_n) excitation functions are shown in Fig. 1.17. Even at energies above the barrier, it is noticeable that neutron transfer processes are dominant. The experimental data relative to fusion are well described by a coupled-channels calculations in which the coupling to neutron transfer processes is considered. In fact, this agreement shows that the breakup process is not as important as it is for weakly bound nuclei.

A comparison between the fusion cross sections at different energies for the systems ^{4,6,8}He+^{197}Au is also presented in [45]. It can be noticed how, at energies below the

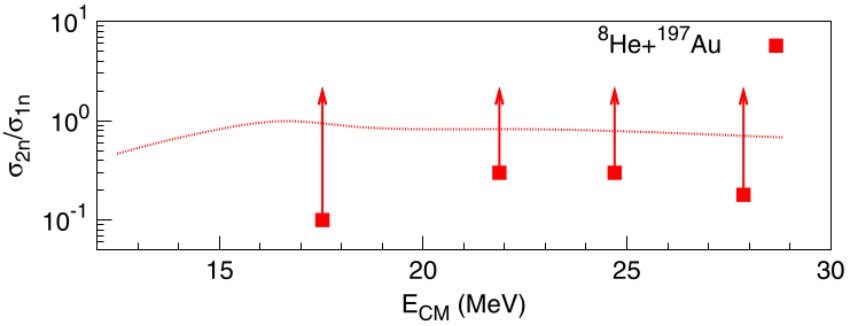

Figure 1.16: *Lower limits for the ratio σ_{2n}/σ_{1n} at different collision energies and coupled-channel calculations for the system ^8He+^{197}Au from [33]. The details for coupled-channel calculations can be found at [45] where they have been performed in order to understand the influence of the transfer channels $^{197}Au(^8He,^7He)^{198}Au$ and $^{197}Au(^8He,^6He)^{199}Au$ on the fusion process.*

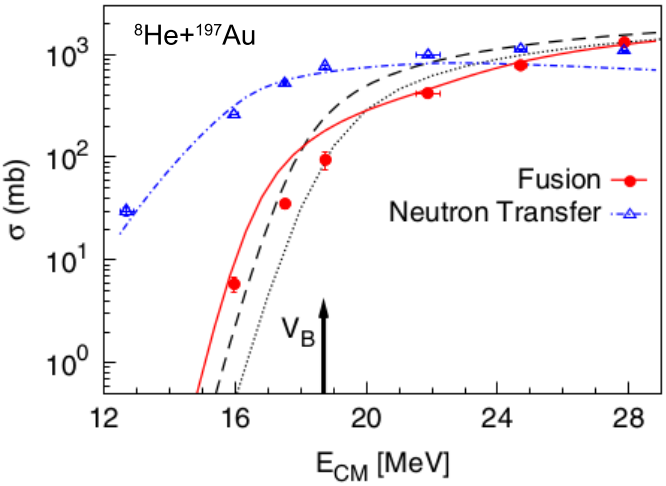

Figure 1.17: *Fusion and neutron transfer excitation functions. Two predictions for the behaviour of fusion are shown with the dotted and dashed curves. The solid line represent a coupled-channels calculation for fusion in which the effects of 1n- and 2n-transfer processes have been taking into account. The dotted-dashed line represent a coupled-channels calculation for transfer [45].*

barrier, σ_f for ^{6}He and ^{8}He are very similar, revealing an important role of neutron-pair transfer before fusion. From the calculations carried out in [45], the transfer of a neutron pair appears to be enhanced over the single neutron transfer as a consequence of pairing correlations.

However, the borromean nature of ^{8}He and the large Q-values, do not allow for the separate measurement of one-neutron (σ_{1n}) and two-neutrons (σ_{2n}) transfer to heavy targets, as the detected residues are the same, considering that both ^{5}He and ^{7}He are not bound. In [32, 33], the system ^{8}He+^{65}Cu has been studied at 19.9 and 30.6 MeV at GANIL by the measurement of coincidences between charged particles, gamma rays and neutrons. The values for σ_{2n}+σ_{1n}, from the gamma rays of the transfer residues, have been estimated to amount to 782±78 mb and 759±114 mb for 19.9 and 30.6

MeV respectively. No ^{67}Cu has been identified after two neutron transfer. In Fig. 1.18 the total (1n+2n) neutron-transfer angular distributions for 19.9 MeV and 30.6 MeV from [32] are presented together with some calculations, while in Fig. 1.19 the elastic angular distributions, obtained with inclusive measurements of ^{8}He, are shown.

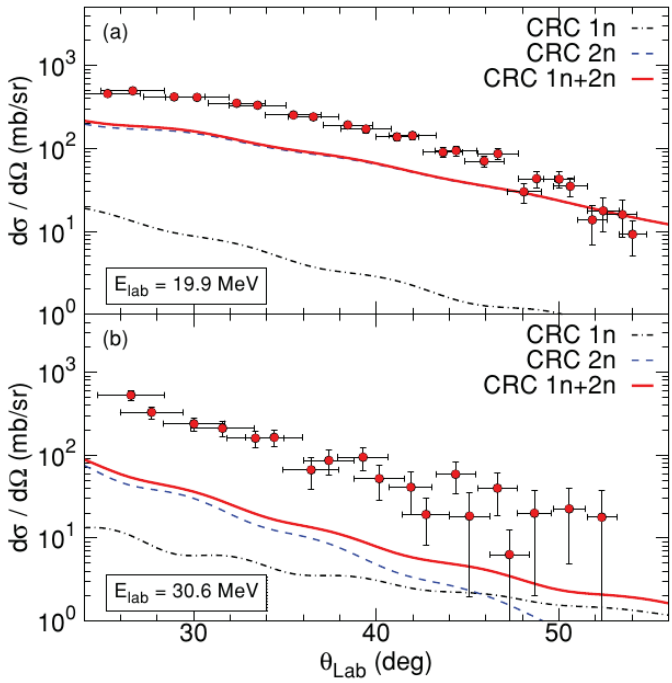

Figure 1.18: *Total neutron-transfer angular distributions for 19.9 MeV and 30.6 MeV and coupled reaction channels calculations for 1n+2n transfer (full line), 1n-transfer (dot-dashed line), and 2n-transfer (dashed line) angular distributions are shown [32].*

1.6.2 Proposal of a new experiment

Despite the experiments described above, the scattering of ^{8}He from heavy targets at energies around the Coulomb barrier has not been deeply studied and only a few scattering data sets are available. Its particular structure should affect the collision process in the presence of a strong Coulomb field, as it is the case of the scattering with a heavy target at energies around the Coulomb barrier. Also, the role of the neutron skin on the dynamics of the scattering process is not clear. Having similar binding energies, it is important to further investigate the competition among the single and double neutron transfer channels, and the direct breakup.

As a consequence of the interesting features of ^{8}He and the lack of information available about its scattering with heavy targets, a proposal of a experiment [46] was presented to the PAC (Programme Advisory Committee) of GANIL (Grand Accélérateur d'Ions Lourds, Caen, France) in 2008 with the aim of studying the scattering of ^{8}He from ^{208}Pb at 16, 18 and 22 MeV, all energies around the Coulomb barrier of the system (∼19 MeV).

The objective of the experiment E587S is the study of the scattering of ^{8}He from

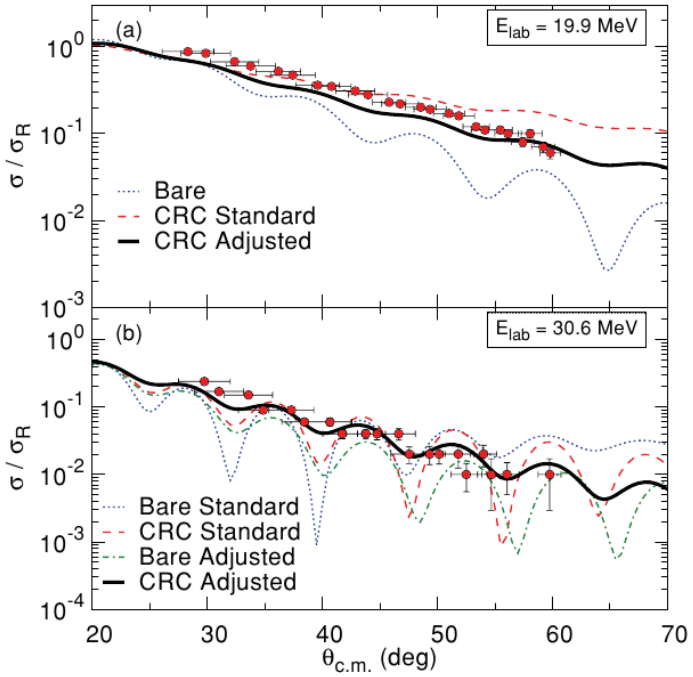

Figure 1.19: *Elastic scattering angular distributions for 19.9 MeV and 30.6 MeV. The coupled reaction channels calculations include the coupling to 1n and 2n-transfer channels. The term adjusted is referred to the modification of the imaginary potential parameters in order to obtain a better agreement with the data [32].*

^{208}Pb by means of the measurement of the angular distributions of both the elastic scattering and the reaction fragments produced in the collision, specially ^{4}He and ^{6}He. The main expected reaction channels (Fig. 1.20) are the following:

- Elastic scattering.
- Direct breakup in ^{4}He and four neutrons.
- Breakup or transfer of one neutron producing ^{7}He which, being not bound, will produce ^{6}He either in its ground state or in an excited state, emitting two neutrons and thus producing ^{4}He.
- Breakup or transfer of two neutrons producing, again, ^{6}He and ^{4}He.
- Tritium production following the reaction $^8\text{He} \rightarrow {}^5\text{H}+\text{t}$.
- Complete fusion of ^{8}He and ^{208}Pb generating ^{216}Po ($T_{1/2} = 0.145(2)\ s$), followed by the evaporation of three or four neutrons producing ^{213}Po ($T_{1/2} = 3.72(2)\ \mu s$) and ^{212}Po ($T_{1/2} = 299(2)\ ns$) respectively, species that will decay by alpha emission to the corresponding lead isotopes.

From the ^{6}He and ^{4}He distributions (excluding the alphas coming from the complete fusion process) it is expected to obtain the influence of the transfer and breakup channels, the role of the coupling to the continuum and relevant information about

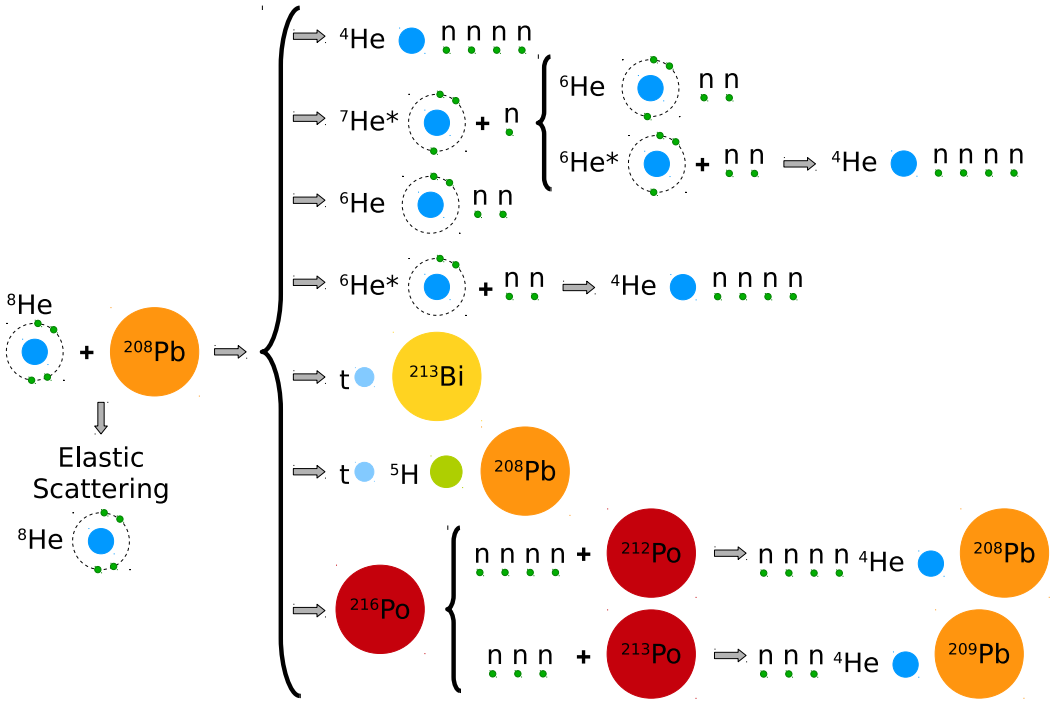

Figure 1.20: *Main reaction channels expected from the interaction of* ^{8}*He with* ^{208}*Pb.*

spectroscopic factors. In [41], calculations have been carried out in order to extract the spectroscopic amplitudes (square roots of the spectroscopic factors) for ^{8}He/^{6}He$_{0+}$, ^{8}He/^{6}He$_{2+}$ and ^{8}He/^{7}He$_{3/2-}$.

As an example of the importance of the coupling to the continuum, in Fig. 1.21 it is represented the angular distribution of the elastic cross section for the ^{6}He+^{208}Pb system at 22 MeV, previously studied by the collaboration.

The direct comparison between the red solid line (generated taking into account the dipolar coupling E1) and the green line (suppressing it), reveals the importance of including the coupling to the continuum. It produces a reduction in the elastic cross section of about a 10%. One of the questions addressed in this thesis is whether this coupling will be relevant also for the colliding system ^{8}He+^{208}Pb.

In Fig. 1.22, three calculations for the quotient between the elastic cross section and the Rutherford cross section for the system ^{8}He+^{208}Pb are shown: *(i)* Optical Model calculations (solid line), *(ii)* a CDCC (Continuum Discretised Coupled Channels) calculation considering the coupling with the breakup channel (dotted line) and *(iii)* a CDCC calculation considering the coupling to the 1n transfer channel (dashed line). It can be observed, for all cases, a strong absorption at backward angles. According to the calculations in Fig. 1.23, the role of the transfer of one neutron is the most important among the considered processes.

The beam time was requested in order to measure the angular distributions of the elastic cross sections at 16, 18 and 22 MeV with a relative uncertainty lower than the 5% in the relevant angular range. The proposal for beam time was made based on the previous experience on experiments with ^{8}He, assuming an intensity of $2{\cdot}10^{5}$ pps, and it is summarized in table 1.5.

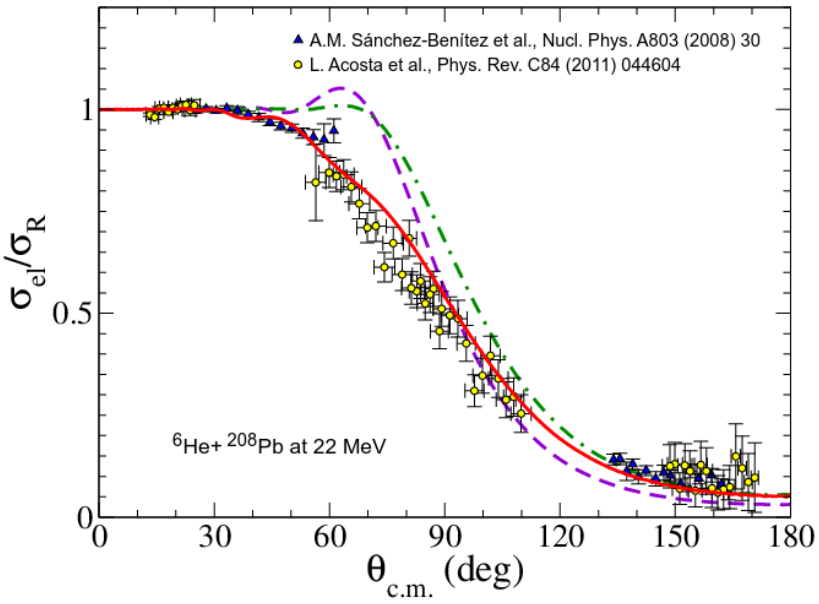

Figure 1.21: *Effect of the coupling to the continuum over the elastic cross section for the system ^{6}He+^{208}Pb at 22 MeV. The experimental data correspond to [26] (depicted with blue triangles) and [25] (yellow circles). While in the green dotted-dashed line the coupling to the continuum has been omitted, in the red solid line it has been introduced.*

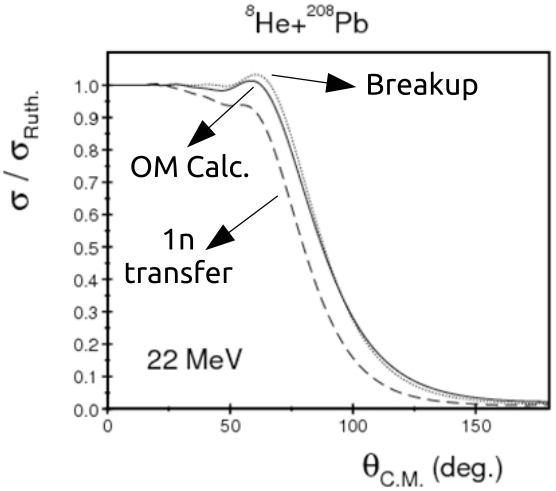

Figure 1.22: *Elastic cross section for the system ^{8}He+^{208}Pb in three different scenarios. See text for details.*

1.7 Theoretical models

In this section, some basics about the models which will be used for the interpretation of experimental results in this work are presented: the Optical Model (OM), the Coupled Reaction Channels (CRC) model and the Distorted Wave Born Approximation (DWBA). These formalisms are exhaustively described in the literature [47, 48] and are implemented in the computing code FRESCO [49] which will be used in chapter

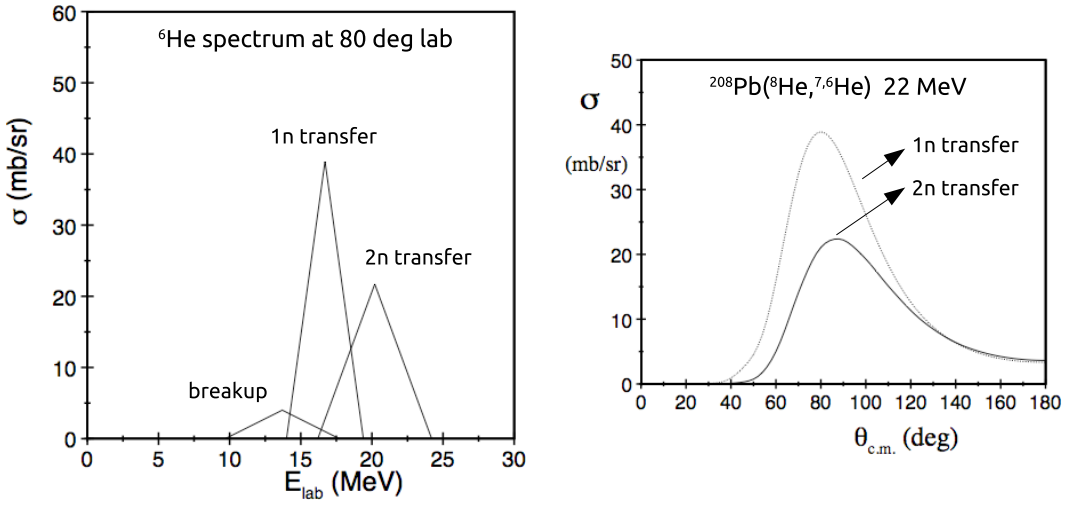

Figure 1.23: *Expected energy distribution of* ^{6}*He fragments at* 80° *(left) and calculations for the* ^{6}*He production cross sections in two different scenarios (right).*

Energy (MeV)	$d\sigma_{elastic}/d\sigma_{Rutherford}$	Intensity (pps)	Requested beam time
16	0.7 (150°)	$2{\cdot}10^5$	6 UT
18	0.5 (125°)	$2{\cdot}10^5$	8 UT
22	0.5 (75°)	$2{\cdot}10^5$	12 UT

Table 1.5: *Summary of the requested beam time for each energy of* ^{8}*He (1 UT = 8 hours of beam).*

4 for the interpretation of the experimental data.

1.7.1 Optical model

The optical model (OM) is one of the most simple models used for describing the elastic scattering. Its name derives from the fact that nuclear scattering is treated in a similar way as the scattering of light by a translucent glass sphere.

The main idea is to replace the complex many-body problem of two interacting nuclei by a simplified interaction of two particles, without structure, colliding through an effective potential $U(r)$. This potential includes an imaginary part which is responsible for the absorption of flux from the elastic channel, i.e., reaction channels different from the elastic scattering. The complication that appears when different reaction channels occur is treated using phenomenological optical potentials, in which case, model parameters are determined by fitting experimental data.

In general, the optical potential is complex, non-local and depends on the angular momentum and spin of nuclei. It is commonly parametrized as follows [48]:

$$U(r) = U_C(r) + U_R(r) + U_I(r) + U_D(r) + U_S(r). \tag{1.7}$$

The meaning of the different parts of Eq. 1.7 is:

- $U_C(r)$: Represents the Coulomb potential and must be included when charged particles are colliding. It is usually expressed in the simple form:

$$\begin{aligned} U_C(r) &= \frac{Z_a Z_A e^2}{2R_c}\left(3 - \frac{r^2}{R_c^2}\right) \quad (r \leq R_c) \\ &= \frac{Z_a Z_A e^2}{r} \qquad\qquad\qquad\quad (r > R_c), \end{aligned} \tag{1.8}$$

  where R_c is the sum of the charge radii of the two interacting nuclei.

- $U_R(r)$: Real potential that represents a potential well with depth V multiplied by a Woods-Saxon form factor, f:

$$U_R(r) = -Vf(r, R, a), \tag{1.9}$$

$$f(r, R, a) = (e^x + 1)^{-1} \quad , \quad x = \frac{r - R}{a}, \tag{1.10}$$

  where R is the radius of the nucleus and a the diffuseness.

  The real part of the optical potential can be derived also from the effective nucleon-nucleon interaction by the Folding Model [50]. In an initial approach, a phenomenological nucleon-nucleus potential v_{aN} can be used for describing the interaction of a nucleon in A with the nucleus a. In this way, a "Single-Folding" potential (U_{SF}) is obtained integrating over the density distribution ρ_A of the nucleus A, following Eq. 1.11.

$$U_{SF}(R) = \int dr_1 \rho_A(r_1) v_{aN}(r_{12}). \tag{1.11}$$

  In the case of the "Double-Folding" potential (U_{DF}), the nuclear matter distribution of both nuclei (ρ_A) and (ρ_a) are taken into account and the interaction between the nucleons in A and a are described by a effective nucleon-nucleon potential v_{NN}.

$$U_{DF}(R) = \int dr_1 \int dr_2 \rho_a(r_1) \rho_A(r_2) v_{NN}(r_{12}). \tag{1.12}$$

  The coordinates used in the folding calculations are explained in Fig. 1.24.

- $U_I(r)$ and $U_D(r)$: Both imaginary parts of the optical potential, represent the absorption effect of flux from the elastic channel:

$$U_I(r) = -iWf(r, R_I, a_I), \tag{1.13}$$

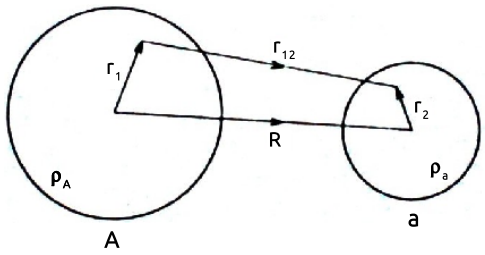

Figure 1.24: *Coordinates used in the folding calculations.*

$$U_D(r) = 4ia_I W_D \frac{d}{dr} f(r, R_I, a_I). \tag{1.14}$$

While $U_I(r)$ acts in the whole volume of the nucleus, $U_D(r)$, as it depends on the derivative of the function f, acts in a region near the surface, where f suffers the largest variations.

- $U_S(r)$: Spin-orbit interaction term:

$$U_S(r) = \vec{\mathbf{s}} \cdot \vec{\mathbf{l}} \left(\frac{\hbar}{m_\pi c^2} \right) V_S \frac{1}{r} \frac{d}{dr} f(r, R_S, a_S), \tag{1.15}$$

where $\vec{\mathbf{s}}$ is the spin operator and $\vec{\mathbf{l}}$ the angular orbital momentum operator. This term is necessary in order to describe polarization effects. V_S, R_S and a_S must be adjusted experimentally. As $U_D(r)$, it is more important at the surface of the nucleus.

The Optical Model is widely used in order to obtain a first description of the elastic cross sections.

1.7.2 Coupled Reaction Channels model

The Coupled Reaction Channels (CRC) model is an generalization of the Coupled Channels (CC) model that includes transfer reactions, i.e., reactions in which one or more nucleons are transferred between projectile and target. The complication introduced by CRC arises from the fact that the exit channel is not represented by the same partition as the entrance channel.

The CC technique is used to describe inelastic scattering and its effect on elastic scattering. In this case, the most relevant are chosen, allowing to solve the Schrödinger equation as a finite set of equations.

The basic ingredients of CC [51] are the potentials describing the elastic scattering in the entrance and exit channels and the coupling potentials which link each channel to each other where the transitions are allowed.

Once the relevant channels are selected, the Hamiltonian can be written as [52]:

$$H = T_R + h(\xi) + V(\vec{R}, \xi) \tag{1.16}$$

where $T(R)$ is the kinetic energy of the relative motion, $V(\vec{R}, \xi)$ the interaction potential between projectile and target and $h(\xi)$ the internal Hamiltonian of the projectile. For simplicity, an structureless target has been considered. For solving the Schrödinger equation, represented by:

$$[H - E]\Psi(\vec{R}, \xi) = 0 \tag{1.17}$$

the wave function may be expressed as a linear combination of the considered channels:

$$\Psi(\vec{R}, \xi) = \phi_0(\xi)\chi_0(\vec{R}) + \sum_{n>0}^{N} \phi_n(\xi)\chi_n(\vec{R}) \tag{1.18}$$

where wave functions χ_n represent the relative motion between projectile and target. $n = 0$ stands for the ground state of the projectile. Projecting over the internal states $\phi_n(\xi)$, a set of coupled equations for the $\chi_n(\vec{R})$ functions are obtained:

$$[E - \varepsilon_n - T_R - V_{n,n}(\vec{R})]\chi_n(\vec{R}) = \sum_{n' \neq n}^{N} V_{n,n'}(\vec{R})\chi_{n'}(\vec{R}) \tag{1.19}$$

being $V_{n,n'}(\vec{R})$ the coupling potential between n and n' states.

When unbound states are involved, as they represent a continuum set of non normalizable states, a process of discretisation or binning of the continuum must be carried out, leading to the Continuum Discretised Coupled Channels (CDCC) technique.

To perform a CRC calculation, the entrance and exit channels optical potentials are needed. It is important to remind at this point that, in this case, these potentials are not the same. Usually, the exit channel potentials for the transfer reaction $A(a, b)B$ are those which describe appropriately the $b+B$ elastic scattering, if data are available, which is not the common situation for exotic nuclei since, usually, one of the two nuclei is not bound. In CRC the coupling will affect both the entrance and exit channels. In addition, some more information is required for a CRC calculation in which a particle x is transferred in such a way that a=b+x and B=A+x:

- The potentials which bind the particle being transferred to the core of the projectile and the target, in order to calculate the internal wave functions of a and B.

- The spectroscopic factors which describe a and B as b+x and A+x respectively. This information is usually taken from spectroscopic measurements or from models on the structure.

1.7.3 Distorted Wave Born Approximation

The DWBA method can be understood as a first approximation of the equations derived from CC and CRC. The DWBA is valid essentially when the elastic scattering is the dominant process between the colliding nuclei and other reaction channels are regarded as perturbations. For its application, it is important to use reliable optical potentials which properly reproduce the elastic scattering cross section, as the distorted waves are generated from this potential.

In contrast to CC calculations, in which an additional channel will in principle vary the coupling potentials, in DWBA the coupling does not affect the elastic scattering.

2 Experimental procedure

This chapter presents the most relevant information regarding the realization of the experiment.

Section 2.1 treats the radioactive beam production in SPIRAL-GANIL, emphasising in the production of Helium beams. In section 2.2 the detection system is presented. Special attention is paid to its design and the conditions imposed during the process in section 2.2.1, while in section 2.2.2 the simulations carried out in order to study the performance of the detection system are commented. Section 2.3 presents the rest of equipment crucial for the realization of the experiment as the reaction chamber or the collimation and beam diagnostics system. The target used in the experiment is described in section 2.4 while section 2.5 is devoted to the analogue electronics and data acquisition. The schematics of data flow and trigger organization is explained. Finally, in section 2.6 some comments can be found on the neutron detectors installed with the aim of study the coincidences between charged particles and neutrons.

The beam time for the experiment E587S was scheduled on September and October 2010. Despite the proposal of studying ^{8}He at three different energies around the Coulomb barrier, the GANIL PAC granted enough time for the measurements at 16 and 22 MeV, carrying out the data taking from 30^{th} September to 3^{rd} October and from 4^{th} October to 7^{th} October respectively. The data taken lasted four days per energy. The whole experiment, including the set-up and tune-up of both the mechanics and the electronics and the calibrations, extended from the 6^{th} September to the 24^{th} October.

2.1 Radioactive beams production in SPIRAL-GANIL

GANIL (Grand Accélérateur Nacional d'Ions Lourds) [53] is a big accelerator facility located in Caen, in the region of the Lower Normandy. GANIL is dedicated to the research, in a large number of fields, by means of ion beams, either stable or radioactive [54]. International collaborations carry out experimental studies of the maximum scientific relevance in this laboratory. The study of nuclei far from the valley of stability has become a major activity in GANIL due to the various cyclotrons which compose SPIRAL and allow the realization of several experiments at the same time.

At SPIRAL, by means of the ISOL technique [55], a primary beam, accelerated by CSS1 and CSS2 accelerators (Fig. 2.1), impinges a production target generating radioactive species through several nuclear reactions. At SPIRAL, the stable ion sources (primary sources), produce a wide spectra of high intensity primary beams, from ^{238}U to ^{12}C, which are accelerated in the range between 24 and 95 MeV/nucleon [55]. After their production, radioactive atoms diffuse out of the target, which is kept at high temperature (around 2300 K) by an external circuit, escaping from its surface and travelling to the ion source, by means of thermal diffusion, through a transfer tube. The ion source is an ECR (Electron Cyclotron Resonance), NANOGAN III model [56] developed for the SPIRAL project. ECR sources achieve a high charge state of the injected atoms. For this purpose it is used a practically neutral plasma where RF waves are injected resonantly interacting with the electrons in the plasma, accelerating them up to high energies. These plasma electrons collide with the atomic electrons of the radioactive atoms producing a positive ionization and generating a charge distribution depending on the atom, with charge states corresponding typically to q/m ratios from 0.09 to 0.40.

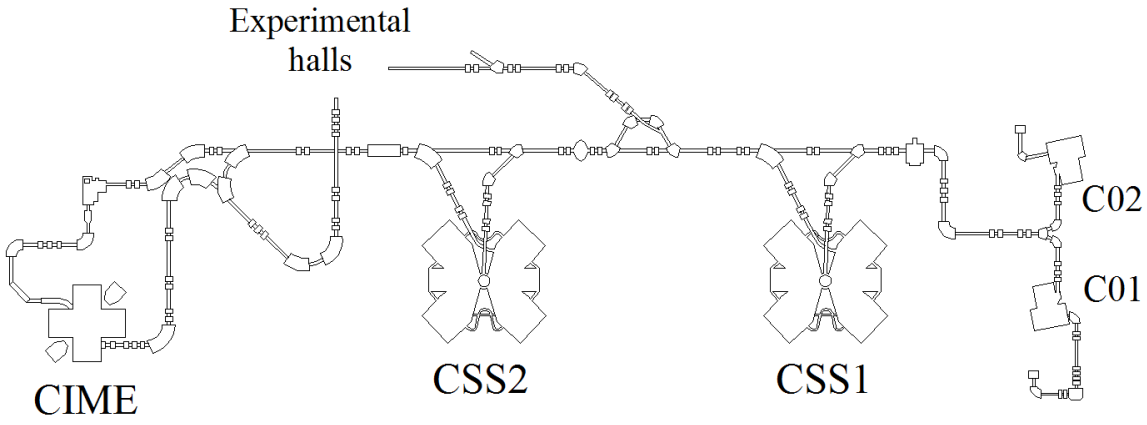

Figure 2.1: *Scheme of the particle accelerator system at GANIL.*

After extracting the ions from the ECR source, the low energy radioactive beam is filtered using a mass separator (magnetic dipole analyzer) with a resolution of $\Delta m/m = 4 \times 10^{-3}$. After this process, the beam can be used directly or injected in the CIME compact cyclotron [57], which accelerating capabilities vary from a minimum of 1.7 MeV/u and a maximum of 25 MeV/u. Its exist also the possibility of using the stable beam accelerated by CSS1 and CSS2.

In particular, the ^{8}He radioactive beam is produced by the fragmentation of a primary beam of ^{13}C at 75 MeV/u. For the production of ^{6}He and ^{8}He, in SPIRAL-GANIL, it is used a specific carbon target, specially developed for the production of those isotopes (Fig. 2.2). The device consists of two different parts. The first part, the production target, is followed by the second one, known as the diffusion target. The ^{13}C beam collide with the first part of the target producing both its fragmentation and the fragmentation of the target nuclei. Those carbon atoms which do not interact, stop in this first part raising up its temperature as they deposit their kinetic energy.

Helium nuclei resulting from fragmentation of the ^{13}C beam stop in the second part of the target. On the other hand, the helium produced from the fragmentation of the

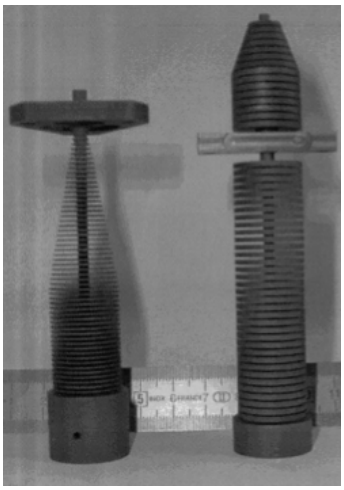

Figure 2.2: *Production target at SPIRAL (left) and special target design for helium beams (right).*

target, are stopped in the first part but manage to reach the second part due to the high temperature in the production target. By means of an external electric current, which is driven within the diffusion target, a high temperature is achieved allowing the produced helium to escape. In table 2.1, the characteristics of the different ^{8}He beams available at SPIRAL-GANIL are summarized. For the study of nuclear reactions at low energies, around 3 MeV/u, ^{8}He with a 1+ charge state is usually used as its production is one order of magnitude larger than for the 2+ state [55].

Charge state	Available intensity on target (pps)	Min E (MeV/u)	Max E (MeV/u)
+1	$3{\cdot}10^5$	2.3	3.8
+1	$1.5{\cdot}10^5$	2.5	4.1
+1	$5.2{\cdot}10^5$	3.5	4.1
+1	$1.8{\cdot}10^5$	3.8	4.1
+1	$3.5{\cdot}10^5$	3.7	3.8
+2	$2{\cdot}10^4$ to $3{\cdot}10^4$		15.4

Table 2.1: *Available intensities for the production of ^{8}He beams at SPIRAL-GANIL [53].*

Once the beam is accelerated till the required energies, it is driven towards the experimental areas. There are ten experimental areas (Fig. 2.3) dedicated to multidisciplinary investigations with stable and radioactive beams at low and medium energies. The E587S experiment was carried out at the G2 area, in particular at the G21 line. The G2 area is subdivided into lines G21 and G22. G21 has been developed for the projects N-Wall [58] ("Neutron Wall", a wall made up of liquid scintillators devoted to neutron detection) and EXOGAM [59] (high efficiency gamma spectrometer). G22 is a more general line. The working area reserved for the experiment, where the reaction chamber and diagnostic systems were installed, corresponds to the place of EXOGAM, before the neutron wall and over the platform of the gamma spectrometer (Fig. 2.4).

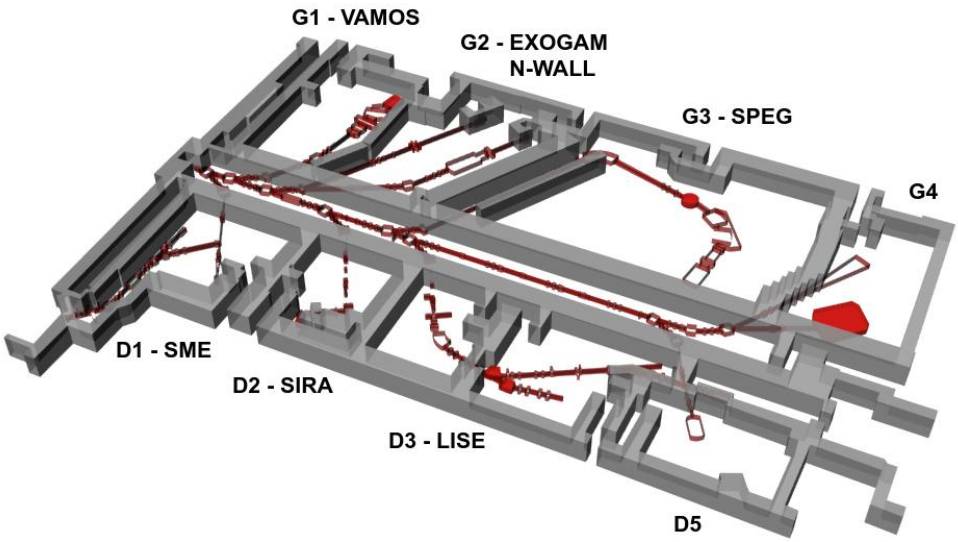

Figure 2.3: *Scheme of the experimental areas at SPIRAL-GANIL. The experiment E587S was carried out at the G2 area, G21 line.*

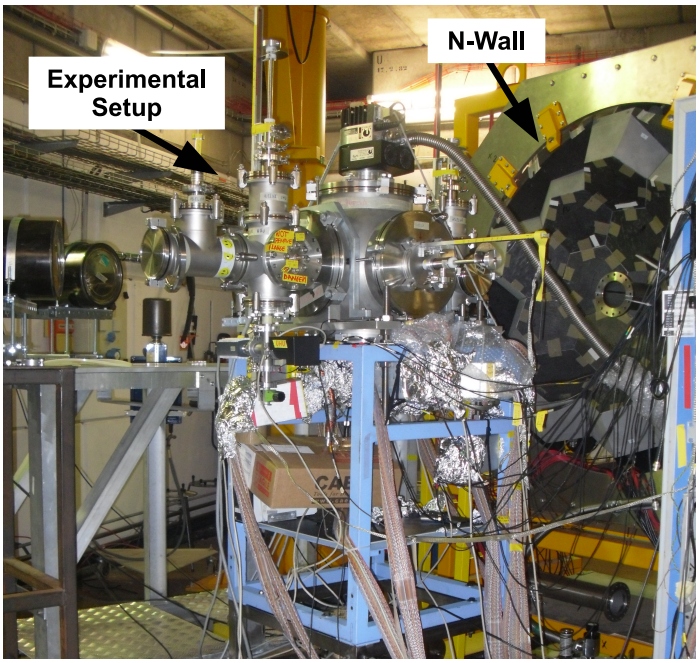

Figure 2.4: *Location of the experimental setup in the G21 experimental hall, next to the N-Wall neutron detector.*

2.2 Detection system

In the last years, the development of facilities capable to produce radioactive ion beams have made possible the study of nuclear properties out of the valley of stability. However, the low intensities available for these beams, in comparison with the ones achieved for stable beams, make necessary the development of particle detection systems with large solid angle, high granularity and a large covered angular range. These detectors must provide efficient particle identification capabilities as well as a wide

energy range of operation, good energy resolution and high granularity for angular correlation measurements. For this purpose, the group of "Estructura de la Materia" at University of Huelva developed a detection system [60], which is described in this section. It was used, for the first time, for the experiment E587S at GANIL.

2.2.1 Design of the detection system

Silicon detectors present excellent characteristics for the detection of charged particles at moderate counting rates (few kHz/cm^2), with an intrinsic efficiency of almost 100%, and a good energy resolution. With the present technology it is possible to manufacture Double-Sided Silicon Strip Detectors (DSSSD) with small strip pitch (less than 100 μm) and large active area ($> 60 \times 60$ mm^2). Therefore they have become widespread used devices for the construction of the charged particle detector arrays needed at radioactive beam facilities.

A number of silicon detector arrays such as MUST2 [61, 62] and TIARA [63] have been built in the last years mainly dedicated to the study of nuclear reactions with light targets in inverse kinematics. The developed detection system, which has been called GLORIA, as the acronym of GLObal ReactIon Array, is foreseen for the detection of reaction fragments produced in direct reactions with heavy targets at energies around the Coulomb barrier. In particular, GLORIA consists of 12 DSSSD (Double-Sided Silicon Strip Detectors) arranged in six particle telescopes.

The use of particle telescopes, a configuration in which the detectors are arranged in ΔE-E pairs, allows for the distinction between different reaction channels. Telescopes are usually designed in such a way that the particles of interest leave part of their energy in the ΔE detector and are completely stopped in the E detector. In this way, some energy is deposited in each detector, producing signals to be processed in the electronic chain simultaneously and independently, digitalized and stored in data files.

The energy loss in silicon depends on the charge and mass of the incident particle following the Bethe-Bloch's formula [64]:

$$S = -\frac{dE}{dX} = \frac{4\pi e^4 z^2}{m_e v^2} NZ \left[\ln \frac{2m_e v^2}{I} - \ln\left(1 - \frac{v^2}{c^2}\right) - \frac{v^2}{c^2} \right], \tag{2.1}$$

where:

v, ze are the velocity and the charge of the incident nucleus,

N, Z are the density (atm/mol) and the atomic number of the material,

m_e the mass of the electron and,

I is the average excitation and ionization potential of the material.

According to Eq. 2.1, the energy loss of a charged particle in a given material is proportional to the square of its charge and inversely proportional to its velocity at each point of the trajectory inside this material.

When the ΔE detector is thin, so that its thickness is small enough compared to the total thickness of the telescope, also the deposition of energy is small in comparison

with the total energy of the particle. In this case, if the energy deposited in ΔE is plotted versus the total energy, two-dimensional spectra called mass-spectra are obtained. In these plots, events corresponding to same charge and mass, but different energy, occupy a hyperbola-shaped geometric place. Therefore, by means of particle telescopes, the identification of reaction fragments is possible thanks to the mass and charge separation of the incident particles.

The six telescopes in GLORIA consist of a first stage of 40 μm thickness and a second stage of 1 mm. The double segmentation of these detectors provide precise information about the position of impact. The DSSSD detectors are based on the model W1 (DS) type 9G delivered by Micron Semiconductor [65]. In this particular model the standard aluminium layer has been replaced by a metallic grid, which occupies only 3% of the total active area, improving the lower energy detection limit. They are fabricated on 4-inch technology, having 16 junction elements (X position) and another 16 ohmic elements (Y position). Detector elements (strips) have a total length of 49.5 mm, 3 mm width and an inter-strip pitch of 100 μm). The detector has a total surface of 50 x 50 mm^2, resulting altogether in 256 pixels of 9 mm^2 area. The wafer is packaged in the standard FR4 transmission frame allowing for assembling several silicon layers in ΔE/E configuration for particle identification, as shown in Fig. 2.5. The double X-Y segmentation provides heavy-ion impact-position information and thus the scattering angle, asumming a point-like beam on target.

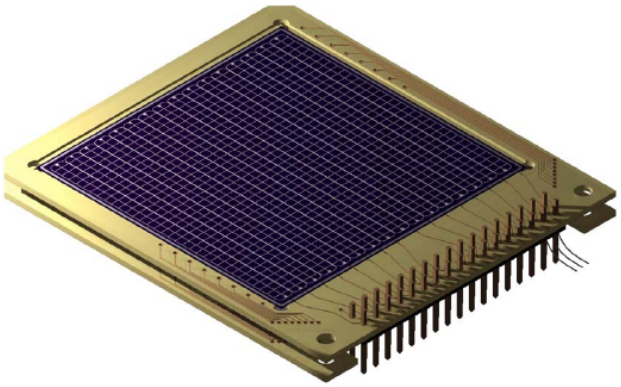

Figure 2.5: *Assemblage of two DSSSD detectors in ΔE/E configuration for particle identification [66].*

During the process of design, several conditions were imposed:

- A good angular resolution, lower than 2.5° was adopted since at Coulomb Barrier energies the cross sections for relevant processes present slow variation with the scattering angle.
- The maximum possible angular range, at least between 15° and 165°. The availability of angular distributions of the cross sections for different processes allows the extraction of relevant physical magnitudes.
- It must exist an overlapping in the angular range covered by adjacent telecopes in order to obtain continuous angular distributions. In this way, as the experimental

data for contiguous telescopes must be similar in the overlapping region, it can be analysed if the data is being properly treated.

- Symmetric position of telescopes, allowing a direct comparison of the number of particles registered in symmetric positions with respect to both the beam and the reaction plane.

The final position of telescopes corresponds to an optimization process in which the previous conditions have been taken into account, as well as the possibility of locating and manipulating the target inside the system (Fig. 2.6). The angular range covered by each telescope and the corresponding solid angles, for the final arrangement of the system are presented in table 2.2.

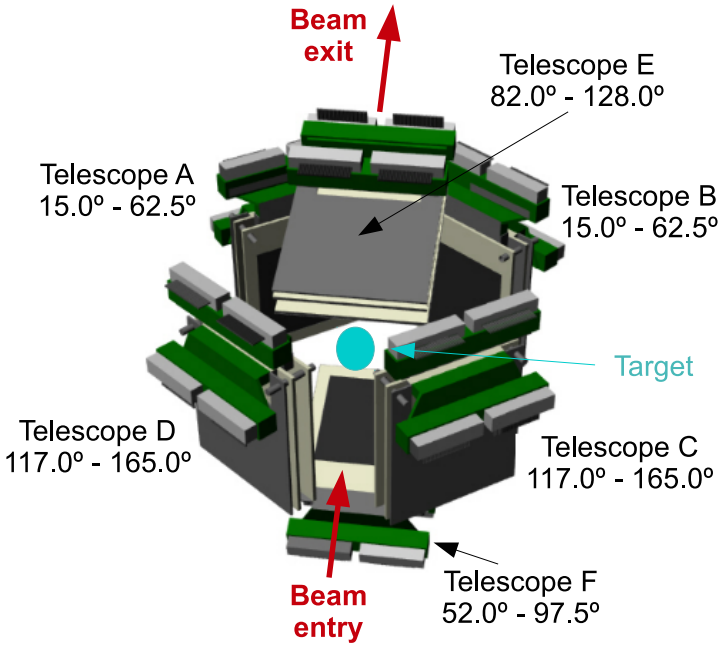

Figure 2.6: *3D drawing representing the relative position of the telescopes as well as the position of the target inside the device.*

Telescope	θ_{center} (deg)	Angular range (deg)	Solid angle (msr) / %4π
Forward A≡1	38	15.0 - 62.5	547.2 (±8.0) / 4.35
Backward C≡3	142	117.0 - 165.0	547.2 (±8.0) / 4.35
Forward B≡2	38	15.0 - 62.5	547.2 (±8.0) / 4.35
Backward D≡4	142	117.0 - 165.0	547.2 (±8.0) / 4.35
Top E≡5	75	82.0 - 128.0	547.2 (±8.0) / 4.35
Bottom F≡6	105	52.0 - 97.5	547.2 (±8.0) / 4.35

Table 2.2: *Angular range and solid angle covered by each telescope, calculated for a point-like source in the nominal target position.*

The position of detectors is kept fixed thanks to a dedicated metallic structure. All telescopes are always tangent to a sphere with a radius of 60 mm, centred in the position of the target (centre of the detection system), in such a way that detectors are always perpendicular to the vector which connect its centre and the centre of the system. The target frame is fixed to the same structure and, therefore, the angular uncertainty is mainly dominated by the pixel geometry and the beam spot size at the reaction target. With the present configuration a geometrical angular resolution of $\pm 2.5^{\circ}$ can be achieved with spot sizes up to 4 mm diameter and a beam divergence around 1°. A suitable collimation system was designed to keep optimal working conditions.

The supporting structure has been designed by means of assisted 2D and 3D drawing software and specific software for mechanical design ([67],[68]). The rigidity of the structure, and the fact that all its components are screwed together, guarantee that the distance between telescopes and their relative position is maintained under control, not varying due to use or time. And additional advantage of the design of the structure is that the telescopes are attached in its outer side, allowing the use of different detectors (as far as they have the same active area) or telescopes with more stages.

In Fig. 2.7, the sequence of assembling and cabling of the detectors is shown. As it can be understand from this figure, all this process can be done out the reaction chamber, representing a great advantage regarding to the handling of the detectors. Once the whole device has been mounted and cabled externally it can be introduced within the chamber.

2.2.2 Monte Carlo simulations of the detection system

Monte Carlo simulations were performed by means of GEANT4 [69, 70, 71] and the NPTool packages [72]. The complete geometry of GLORIA including the target ladder and the six DSSSD two-stage detector telescopes was implemented. For a first analysis of the detector response a simple elastic scattering event generator have been used. For the energy distribution, a Gaussian shape with a large width to cover a wide range of energies have been chosen.

A bi-dimensional spectra ΔE vs. E_{total} for a central pixel of a forward DSSSD telescope at 21° is shown in Fig. 2.8 and Fig. 2.9. The banana-like regions correspond to various test isotopes from hydrogen to ^{13}C. The hydrogen isotopes show the typical back bending due to the particle punch-through effect at the second stage of the telescope.

The quality of the mass discrimination achieved by a particle detector system can be accounted for by using the "Figure of Merit (FoM)" (Eq. 2.2), as defined in [73]:

$$FoM = \frac{E_c}{FWHM_1 + FWHM_2} \tag{2.2}$$

being E_c the separation energy between the centroids of two adjacent peaks and $FWHM_1$ and $FWHM_2$ the corresponding full widths at half maximum. A detector

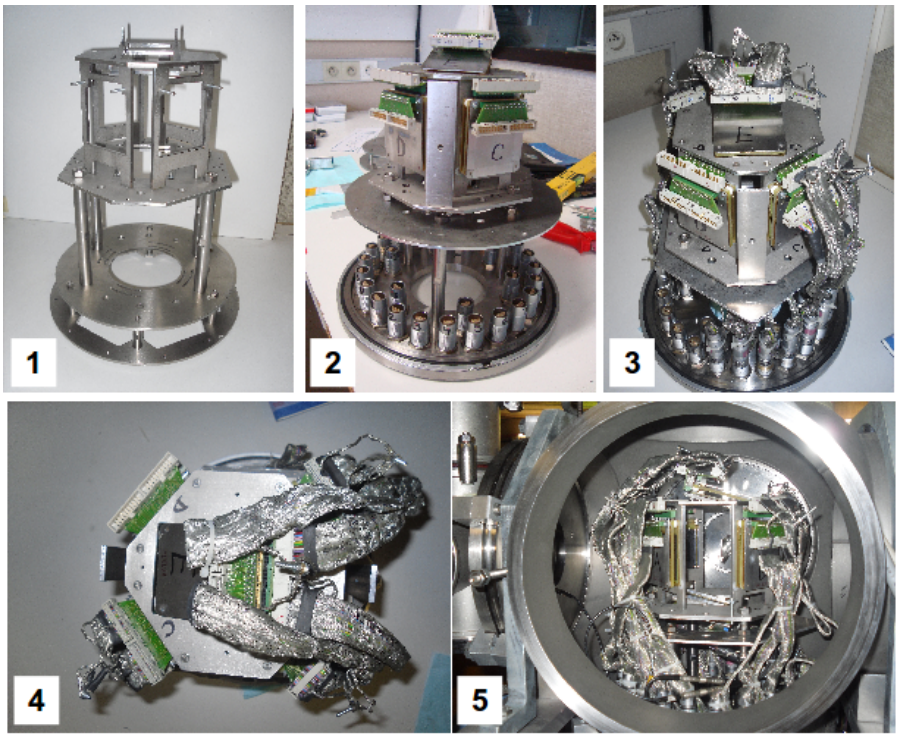

Figure 2.7: *Assembly sequence and cabling of the detector. In the first picture (labelled as 1) it is shown the stainless-steel structure for supporting the detectors mounted over the auxiliary structure needed to fix the whole device inside the chamber. In picture 2, all detectors has been attached to its supporting structure and the auxiliary structure has been fixed to the flange. In 3 and 4, two pictures showing the process of cabling are shown and, finally, in picture 5 the whole device, already cabled, has been introduced into the chamber.*

system will exhibit good identification capability when FoM > 0.7.

We have studied the value of the FoM for the case of the carbon isotopes for the telescope. The region marked with a red square (an energy slice in the carbon mass region, centered at 55 MeV and with an energy width of 100 keV) in Fig. 2.9 has been projected onto the ΔE axis. The resulting ΔE energy spectrum is presented in Fig. 2.10. The distribution has been analysed using a two-Gaussian fit and the result is shown with a blue line. For the present case we obtain a value of FoM of 0.9 for ^{12}C/^{13}C identification. It should be noticed that in routine data analysis a better isotope separation can be expected by the use of dedicated polygonal cuts, or with a suitable mathematical transformation (rotation) of variables [74].

In Fig. 2.11 the angular distributions of the emitted and detected particles are shown. The simulated geometrical efficiency of the detector array, defined as the ratio between emitted and detected particles, as a function of the observation angle, is shown in Fig. 2.12. The angular overlap between DSSSD detectors is around 10° and the simulations confirm that the array can provide a full angular coverage from 15° to 165°. The overlapping angular regions between DSSSD telescopes are localized as a sudden increase in the geometrical efficiency around 15°-52° (forward and top detectors), 82°-98° (top and bottom detectors) and 128°-165° (bottom and backward

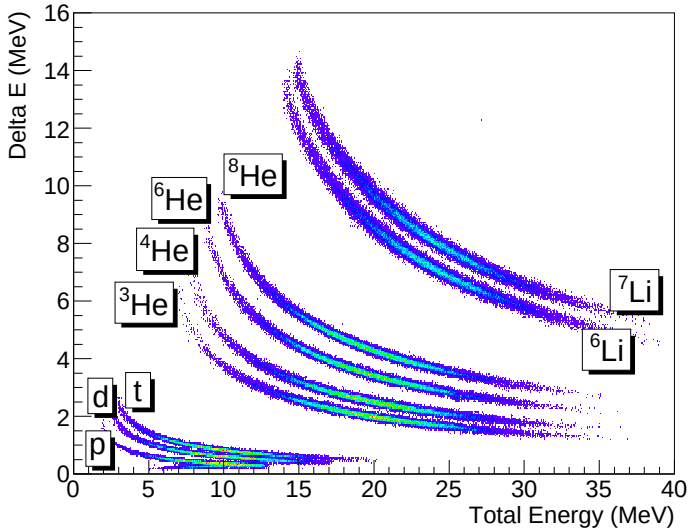

Figure 2.8: *Monte Carlo simulation of the detector response for light ions from protons to ^{7}Li. In particular the expected mass spectrum for a central pixel (21° Lab) of a forward DSSSD telescope is shown.*

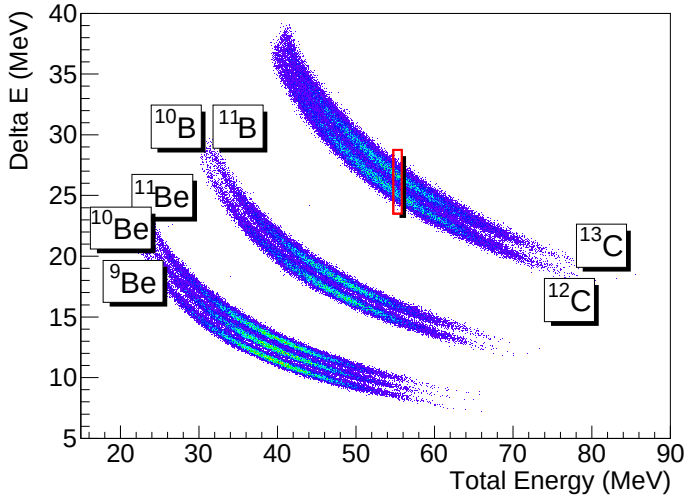

Figure 2.9: *Monte Carlo simulation of the detector response for light ions from ^{9}Be to ^{13}C. The expected mass spectrum for a central pixel (21° Lab) of a forward DSSSD telescope is shown. The region marked with a red square has been used for the evaluation of the mass resolution (Figure of Merit, FoM) of the device. See text for explanation.*

detectors). Pixel solid angles vary between 2.0 and 2.5 msr along a given telescope.

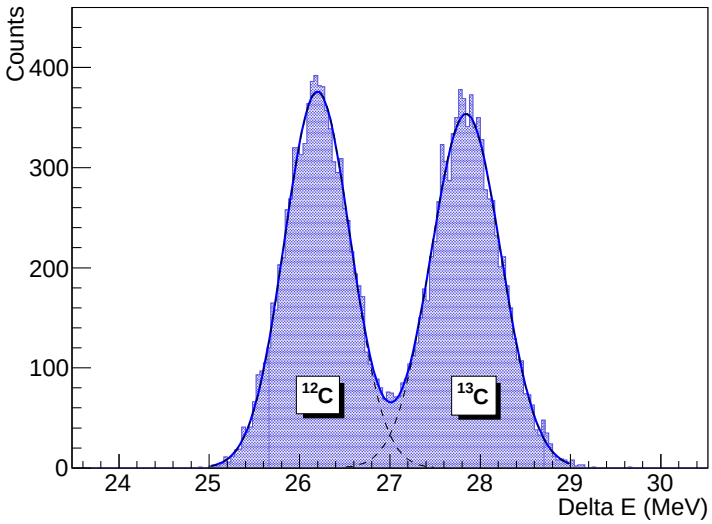

Figure 2.10: *Projection of the energy slice in the carbon mass region marked with a red square in Fig. 2.9 onto the ΔE axis centred at 55 MeV and an energy width of 100 keV. See text for discussion.*

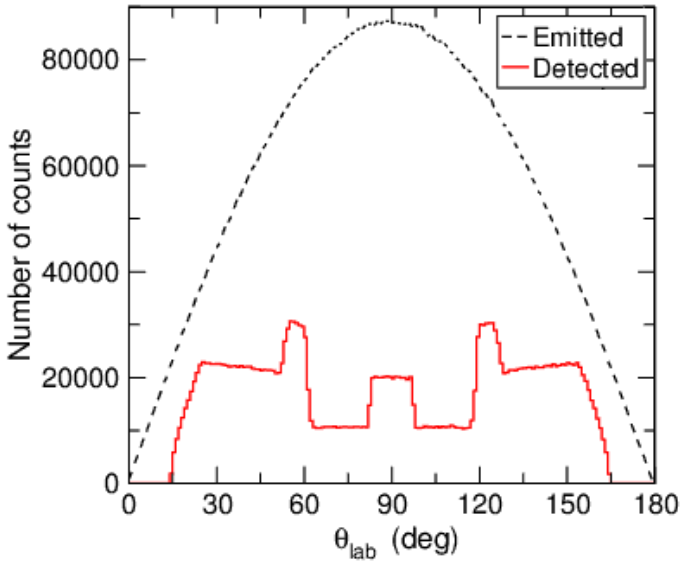

Figure 2.11: *The angular distribution of the emitted particles produced by the event-generator is shown with a black dashed line, whereas the corresponding distribution of the detected particles is shown with a red line.*

2.3 Reaction chamber and diagnostic systems

The detection system was mounted on a standard 250 DN LF reaction chamber. The LF sealing, based on viton rings and metallic claws, has the disadvantage of a limited vacuum, of around 10^{-7} mbar which is, anyway, enough for the experiments for which the system is devoted. At both sides of the reaction chamber, collimators and beam

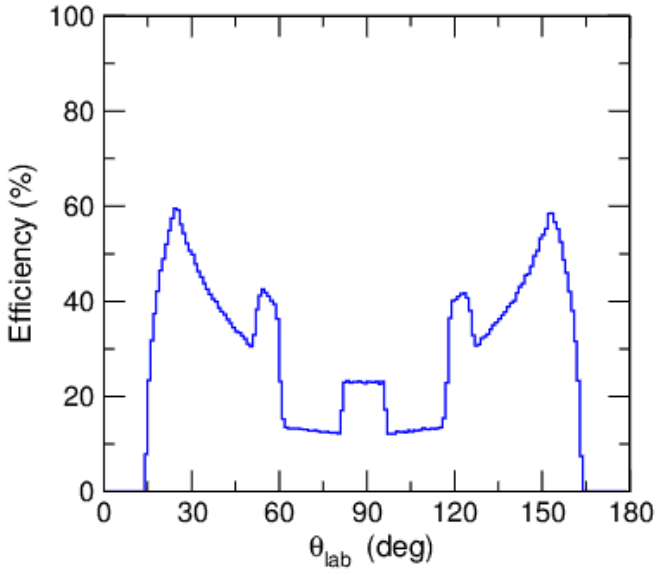

Figure 2.12: *Angular distribution of the geometrical efficiency.*

diagnostics systems were installed with the aim of monitoring the beam properly during the beam tunning phase, in order to quickly optimize its transmission and focusing on the target. In Fig. 2.13 a sketch of the detection system together with beam diagnostic systems S1, S2 and S3 is shown.

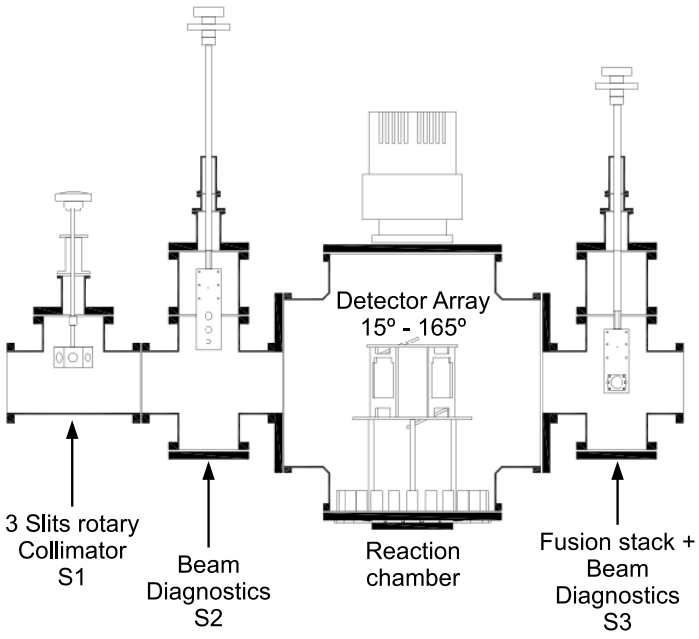

Figure 2.13: *Sketch of the reaction chamber, where the detection system is installed, together with the beam diagnostic systems S1, S2 and S3.*

The S1 system placed at the entrance of GLORIA consists of a rotary cylindrical frame with three circular collimating holes of 20 mm, 15 mm and 8 mm diameters, respectively. At a distance of 225 mm downstream it is placed the S2 system, which

is made of a rectangular frame with collimating holes of 1 mm, 5 mm, 10 mm and 30 mm diameter. At the same frame and centred over the 1 mm hole, there is a standard single-pad detector of 500 μm thickness (PIP) from CANBERRA [75]. S2 can be both rotated and displaced vertically, so that for beam tuning it is possible to choose among the three collimators, the 1 mm diameter collimator covering the silicon detector or, by rotating the frame, the full detector area of 2 cm diameter.

The target holder is placed 355 mm from S2, having room for five different target foils of 2 cm diameter and a Faraday Cup (FC) at the end. It is provided with a push-pull and free rotary system for alignment and positioning. The S3 system is placed 255 mm from reaction target. It consists of a rectangular frame with a 1 mm diameter hole, covering a PIP detector in similar manner as in S2. It also holds a FC with the additional possibility of installing a secondary reaction target (fusion target) for simultaneous measurement of fusion cross sections.

By adjusting the collimators placed at S1, S2 and S3 the beam operator can tune the pilot beam and check the beam size and divergence. By setting the S1 opening at 8 mm and the S2 opening at 5 mm, the operator can optimize beam intensity using the FC placed at the target frame. This configuration would correspond to a beam divergence below 1° and a maximum spot size of 4 mm at target position. Fine alignment of the pilot beam is provided by the FC at S3. By measuring the FC yield at S2 and S3 for each of the collimators at S1 and S2, the beam size at target position can be deduced. In this way, the transmission and alignment of the beam can be optimized.

For tuning the radioactive beam, the intensity must be reduced until it reaches a value representing no risk for the PIP detectors. This depends on the ionization produced by the beam on the detector [75]. When the signal is lost at the FC, the PIP detector at S2 can be set facing the beam protected by the 1 mm collimator. By further reduction of the beam intensity S2 can be rotated so the full active area of the PIP detector can face the beam. In this way a direct measurement of RIB intensity and energy is performed. By using the corresponding collimated PIP detector at S3, the RIB beam is driven through the exit of the chamber. Rotating S2 and S3, PIP detectors can be both set to face the beam, and by combining collimators at S1 and S2, the size and divergence of the RIB can be obtained.

2.4 Target

For the experiment described, a self-supported ^{208}Pb target was used. Particularly, it was used a thin ^{208}Pb foil with a thickness of 1.1 mg/cm^2, which allows a compromise between statistics and energy resolution. The ^{208}Pb nucleus provide a strong Coulombian field, ideal for the study of the scattering of ^{8}He.

The isotopic composition of the target was the following: ^{208}Pb 98.43 %, ^{207}Pb 1.05 %, ^{206}Pb 0.51 %, ^{204}Pb 0.01 %. The analysis was done by means of the ICP-MS technique (mass spectrometry). This technique allows determining and quantifying most of the elements in the periodic table.

2.5 Analogue electronics and data acquisition

Each DSSSD detector generates a total of 32 charge signals. Including the two PIP detectors for beam tuning a total of 386 electronic channels should be amplified, shaped and digitized. This rather large number of channels can still be handled by using commercially available multipurpose modules.

Front End Electronics (preamplifiers and shapers) have been manufactured by Mesytec GmbH [76]. Junction and ohmic strips of the DSSSD detector (16 strips per side) are connected to one of the four 16-channel preamplifier boards in model MPR-64. The modules are located as close as possible to the reaction chamber in order to improve signal-to-noise ratio. Straight afterwards, energy signals are shaped and amplified using STM-16 modules, which also provide the corresponding trigger for the logic chain when the shaped amplitude exceeds a programmable threshold level. Detectors are biased with four-channel bias modules model MHV4. PIP detectors signals used for beam tuning process are amplified and shaped at MSI8 module.

The slow control of the complete system (shaper gains, thresholds and detector bias) can be remotely operated with a dedicated application [77] implemented within LabVIEW programming environment [78] by means of RS232 connection ports linked in a daisy chain.

Data acquisition is based on VME standard cards, most of them manufactured by Caen SpA [79]: peak-sensing analog-to-digital converters (mod. V785), time-digital-converters (mod. V778) and digital counters/latching-scalers (mod. V830). All these cards are daisy-chained connected and fired simultaneously by the MAIN-TRIGGER. This trigger is also used for starting the analog-to-digital conversion, the time-to-digital conversion process, and the general system data readout. Crate control and trigger management are performed by means of a power PC card model RIO2 from Creative Electronic Systems (CES) [80] which operating system, MBS, runs LYNX-OS system and the TRIVA trigger card developed at GSI [81].

Trigger logic is organized in NIM standards via multipurpose modules, also from Caen SpA: Fan-In-Fan-Out (mod. N454), Dual-Timer (mod. N93B), Constant-Fraction discriminator (mod. N843) and Triple 4-Fold Logic Unit (mod. N405). Trigger signals are individually synchronized by using gate-and-delay GG8020 from ORTEC [82].

GLORIA detector will typically run in the so-called coincident-XY TOTAL-OR configuration, that is, for any DSSSD, all events presenting signal-over-threshold at ohmic and junction strips will be accepted for firing the MAIN-TRIGGER of the data acquisition. The coincident-XY condition, implemented at hardware level, becomes very useful for rejecting unphysical events originated from electronic noise. Nevertheless, the flexibility of the hardware configuration foreseen for trigger management makes possible implementing more restricted options.

The schematics of data flow and trigger organization is shown in Fig. 2.14 .After pulse arrival, the constant-fraction gate produced at each STM module (total sum of the 16 strips) is used as a trigger signal. At the first trigger level ohmic vs. junction event coincidence (coincident XY condition) is required for each DSSSD detector. The

minimum resolving time of the ohmic/junction coincidence in the electronic chain is 3 ns, which is the limit of the coincidence module (N405). This value matches properly the 3 ns jitter expected form the gate-and-delay unit GG8020 and the leading edge resolution of 0.4 ns of the STM-16 module. When coincident events arrive a gate of 25 ns is produced for building the corresponding trigger.

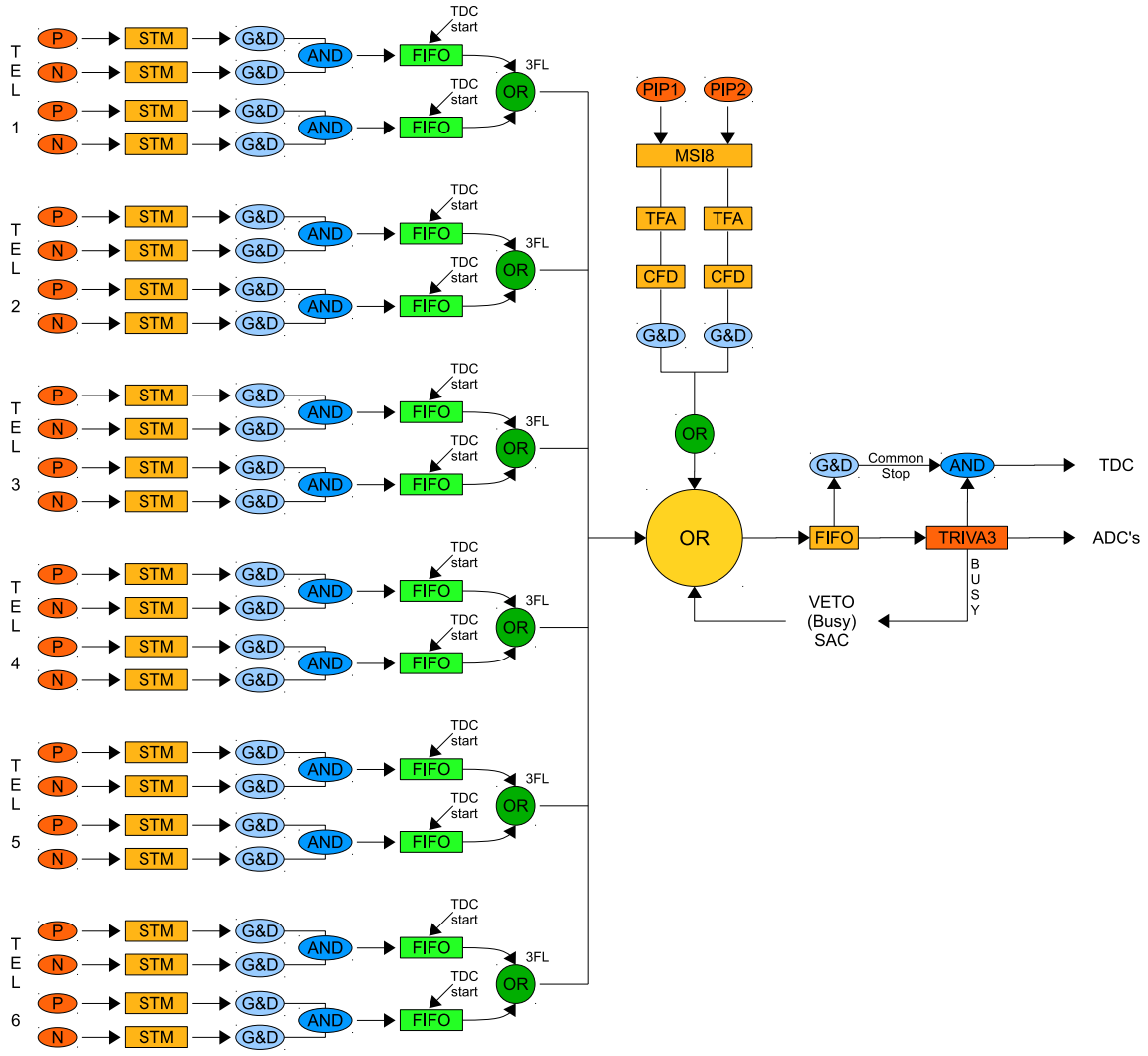

Figure 2.14: *Trigger setup of GLORIA detector array. TEL(n): DSSSD telescope, P/N: DSSSD junction/ohmic side, PIP 1-2: Silicon detectors for beam diagnostics, MSI8: preamplifier and shaper module, STM: STM16 module, G&D: gate-and-delay, AND/OR (3FL): Triple 4-Fold-logic unit in coincidence/sum, FIFO: Fan-in-Fan-Out, TFA: Time-fast-amplifier, CFD: Constant fraction discriminator, ADC: Analog-to-digital converter, TDC: Time-to-digital converter, TRIVA3: Trigger module, SAC: System acquisition. See text for explanation.*

First level triggers are summed to generate a COMMON-OR using another N405 box (the module contains three four-channel logic units with veto), which constitutes the MAIN-TRIGGER used for firing the data acquisition system. The VETO option is used for blocking the readout process when MAIN-TRIGGER is generated. A similar procedure is envisaged for the two PIP detectors. In this case the fast timing output

of the MSI-8 module is first amplified by using N979 module from Caen SpA, and the trigger is generated after filtering with the N843 constant-fraction module.

The MAIN-TRIGGER is send simultaneously to the TRIVA module and to a Dual-Timer, the latter used for adjusting the gate width needed for the analog-to-digital conversion. The TRIVA module initiates the acquisition process and generates the SYSTEM-BUSY gate signal, which is send to block the arrival of signals by vetoing the system COMMON-OR. This gate protects the acquisition during event readout and data processing.

Timing measurements are performed using the so-called common-stop method. First-stage (coincident X-Y) detector-triggers are sent as starting signal for the time-to-digital converter (TDC). The time measurement stops at the arrival of the MAIN-TRIGGER, which is properly delayed by using a gate-and-delay unit to allow all relevant events reaching the acquisition system in time. The TDC module can be operated with a maximum time resolution of 140 ns distributed in 4096 channels (0.03 ns/channel).

Data acquisition software is based on the so-called Multi Branch System (MBS) and Go4 developed at GSI [81]. A dedicated PC connected via Ethernet is used for communication with RIO2 and for data storage. In table 2.3 pulse shaping modules, logic and VME cards included in GLORIA front-end, trigger and data acquisition systems are summarized.

Unit type	Modules (×channel)	Model	Supplier
Preamplifier	6(×64)	MPR64	Mesytec GmbH
Detector bias	3(×4)	MHV4	Mesytec GmbH
Shaper	12(×16)	STM16	Mesytec GmbH
Preamplifier and shaper	1(×8)	MSI8	Mesytec GmbH
Fan-In-Fan-Out	4(×4)	N454	Caen SpA
Dual Timer	2	N93B	Caen SpA
Triple 4-Fold Logic	6(×3)	N405	Caen SpA
Constant Fraction Discriminator	2(×8)	N843	Caen SpA
Fast Amplifier	2	N979	Caen SpA
Gate-and-Delay	3(×8)	GG8020	Ortec
Crate Controller	1	RIO2	CES
Trigger Manager	1	TRIVA3	GSI
Digital counter / Scaler	1(×32)	V830	Caen SpA
Analog-to-Digital Converter	13(×32)	V785	Caen SpA
Time-to-Digital Converter	2(×32)	V775	Caen SpA
Slow Control	1(×2)	MRC1	Mesytec GmbH

Table 2.3: *Summary of pulse shaping modules, logic and VME cards used for GLORIA silicon detector array.*

2.6 Neutron detectors

With the aim of studying the coincidences between the charged particles detected by GLORIA and the generated neutrons, specially in the neutron rich ^{8}He, four neutron detectors from the EDEN system [83] were installed around the reaction chamber.

EDEN (Etude de DEcroissances par Neutrons), was developed at IPN-Orsay (France), and it allows the detection of neutrons and the measurement of their energy through time of flight technique. EDEN consists of 40 modules of NE213 scintillator as the one shown in Fig. 2.15, and it is used mainly for separating neutrons and gammas by means of the shape of the pulse that they generate. The chosen photomultipliers are 4502B and 4512B (new version of 4502B) manufactured by Philips Components. The efficiency of the EDEN detectors is about 1% for 6 MeV neutrons, with a resolution of 60 keV and 500 keV for 1 MeV and 6 MeV neutrons respectively, which implies a length of 1.75 m for the flight path.

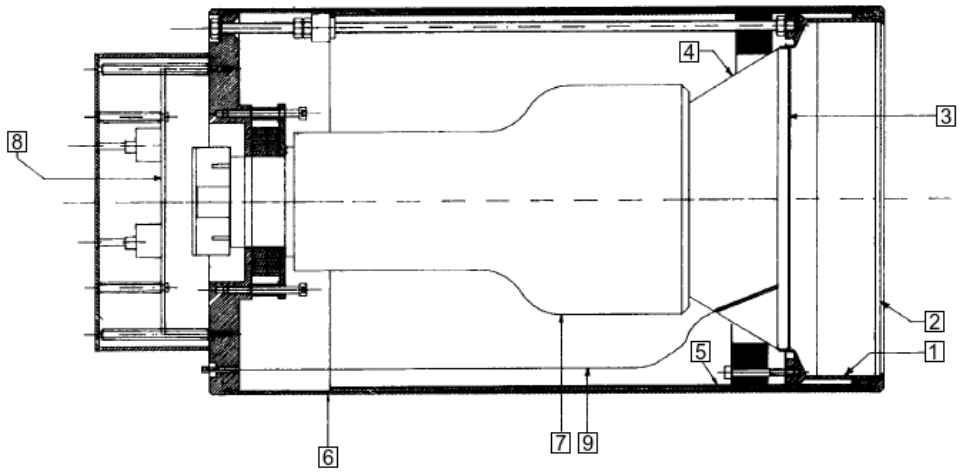

Figure 2.15: *Scheme of a module from the EDEN detection system from [83]. (1) Scintillator cell, (2) Deformable face, (3) Glass window, (4) Light pipe, (5) Metal shielding, (6) Soft-iron shielding, (7) Photomultiplier, (8) Socket, (9) Optical fiber.*

In Fig. 2.16 (left), the output signal of an EDEN photomultiplier us shown for both a neutron and a gamma. As it can be observed, the response of the detector is sensitive to the kind of incident particle. The discrimination between particles is achieved integrating the output signal with two different temporal windows, one which encompass the whole signal and a second one, delayed, which covers just the "slow" tail of the signal. This way, when plotting the result of both integrations, one versus the other (Fig. 2.16, right), the neutron-gamma discrimination is achieved.

In Fig. 2.17, an on-line spectrum taken during the experiment E587S is shown, where it can be observed how the EDEN module is achieving a reasonable discrimination between neutrons and gammas. A detailed analysis of the data obtained from the E587S experiment with EDEN has not been carried out so far. However, Fig. 2.17 bring to light the interest of its combination with the GLORIA detection system for future experiments.

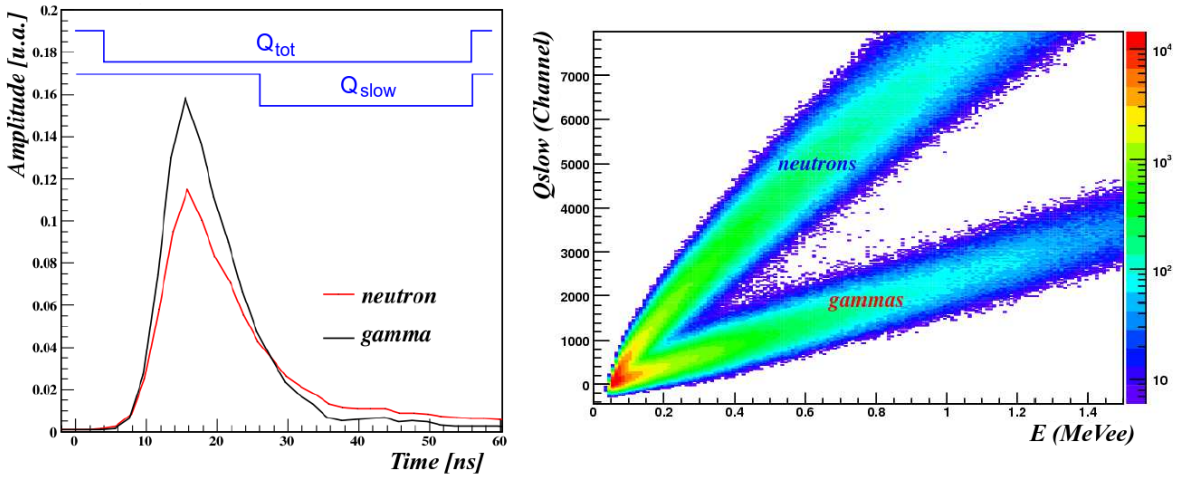

Figure 2.16: *(Left) Integration of the output signal from an EDEN photomultiplier for both a neutron and a gamma, using two different temporal windows. (Right) Charge obtained by integration in the slow temporal window vs total charge [84].*

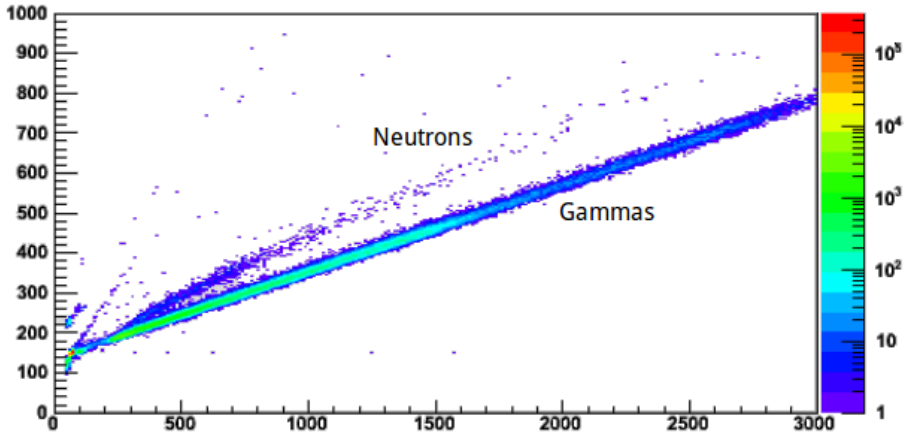

Figure 2.17: *On-line spectrum for one of the EDEN detectors used in the E587S experiment.*

3 Data analysis

In this chapter, the data analysis performed for the E587S experiment is presented.

In section 3.1 the way of obtaining the ΔE-E$_{total}$ spectra, in which the identification of reaction channels is possible, is explained, emphasising the calibration procedure. Once the spectra have been properly generated, the definition of selection windows or integration regions is presented. Three main integration regions have been defined, one for ^{8}He, one for ^{6}He fragments and a third one for ^{4}He fragments. In this way, the total number of ^{8}He, ^{6}He and ^{4}He events detected by each pixel is obtained through the integration of the events within the selection windows defined in the ΔE-E$_{total}$ spectrum related to this pixel.

Afterwards, in section 3.2, an experimental correction due to the efficiency of the detection system is introduced. This correction arises, mainly, from the efficiency of the electronic chains which have been evaluated based on test signals sent to the preamplifiers during all the experiment.

Subsequently, section 3.3 is devoted to the determination of an effective position of the beam spot on target and the detection system. Generally, in experiments previously carried out by the collaboration, stable pilot beams were used in order to normalise the experimental data. If this technique is applied, and if the position of the detection system is the same and also the electronic chains and the beam parameters are maintained, the solid angle dependence can be removed. However, this option was not available for the experiment E587S. This is the reason why a strong effort has been made in order to properly assign not only the scattering angles but the solid angle of each pixel in the setup. The assignment of these angles is the consequence of a process of determination of the effective position of the beam spot on target and the detectors array during the experiment. The main tool used in the search for this position is the simulation of the experimental device, with the aim of reproducing its performance in the experiment. The section 3.3.1 is devoted to cross-check the simulations performed.

In section 3.3.2, a starting point position for the detection system is derived from the comparison in the number of elastic events detected by symmetric telescopes. In section 3.3.3 a study is carried out in order to understand the influence of the rotated position of the target in the experimental data. Once the starting point position has

been determined at both energies, 16 and 22 MeV, the method for obtaining the best effective position is defined in section 3.3.4 and next, in sections 3.3.5 and 3.3.6, this method based on the simulation of several position of the beam spot on target and the detectors array is applied.

Finally, section 3.4 shows how the normalised cross section and its uncertainty are calculated and section 3.5 is dedicated to the calculation of the ^{6}He/^{8}He and ^{4}He/^{8}He ratios.

3.4, it is shown how the normalised cross section and its uncertainty are calculated.

3.1 Obtaining spectra: Identification of reaction channels

The events validated by the implemented detection logic are stored in list-mode (name which gives rise to the .lmd extension of the files) by the acquisition, in data files that can be opened or closed manually or automatically when their size reaches a given value. Each data file is usually called *run*, and it contains the value of each ADC and TDC channel for every registered event, among other possible parameters included in the acquisition.

For the data analysis, the software PAW++ (Physics Analysis Workstation) [85] and ROOT [86] (a framework for data analysis), both developed at CERN international laboratory, have been used. PAW++ uses an specific format called ntuple so, as a first step, the list-mode files are converted to this format. The ntuple is organised as a table in which each row corresponds to a registered event and each column to one of the variables stored (adc channel, tdc channel, etc...). However for the analysis made with ROOT, it is necessary to convert all ntuple files into .root files, through a subroutine called h2root included in the ROOT distribution.

As it was introduced in 2.2.1 the detectors used for the E587S experiment are doubly segmented, having thicknesses of 40 μm and 1 mm for ΔE and E, respectively. The analysis is made for every pixel of the 40 μm detector, so that a ΔE-E$_{total}$ spectrum is obtained for each pixel, associated to the observation angle where it is located. A pixel is defined, as shown in Fig. 3.1, as the intersection between a p strip (vertical) and an n strip (horizontal).

For every spectrum, the number of events related to each reaction channel is integrated using the so-called integration regions or selection windows. Integration regions can be defined for every ΔE-E$_{total}$ spectrum but it becomes difficult, for example, in the case of the elastic channel, and in particular in pixels with associated large scattering angle and therefore small statistics. For this reason, selection windows have been determined in "summed" spectra, i.e., two-dimensional spectra corresponding to the addition of single spectra from pixels with a similar scattering angle. In such a way, the statistics of the summed spectrum is enough to determine the integration region for every reaction channel, and once it has been determined, it is applied to the spectrum of every pixel independently.

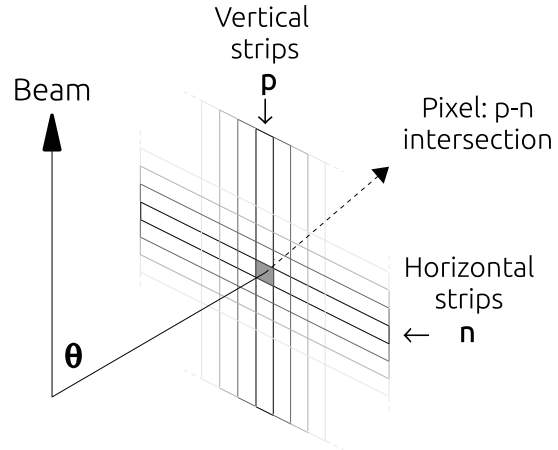

Figure 3.1: *Pixels are defined as the intersection between a p strip and an n strip. This double segmentation which gives rise to pixels, makes possible the obtaining of information about the scattering angle.*

As a step towards the integration of the different events registered in the ΔE-E$_{total}$ spectra, it is important to remove the largest possible number of non-physical events, for example from noise-noise coincidences, or events that despite having a physical meaning, their registered signal was somehow anomalous. In this category, for example, particles that hit the detector in the region between two strips distributing their energy between them can be found. Non-valid events are removed imposing certain conditions at software level while generating spectra.

Energy channels are registered within runs as *ADC* channels. Every *ADC* channel is associated to a specific strip of a specific detector. Basic two-dimensional spectra are generated plotting:

$$(ADC40p) \;\; vs \;\; (ADC40p + ADC1000p), \tag{3.1}$$

where $ADC40p$ stands for the *ADC* channel corresponding to a strip p of a 40 μm detector and $ADC1000p$ stands for a vertical, p strip, of a 1 mm detector. In this way, the spectrum is associated to a full strip. The first condition to impose should be such that the number of events is reduced only to the ones registered by a pixel, making possible to assign to this spectrum the scattering angle of this specific pixel. For this, *ADC* channels associated to n strips of the ΔE detector, namely $ADC40n$, will be used. When a particle passes through a pixel, the p and n strips which define it must register approximately the same value of the deposited energy, so that the first condition is:

$$|ADC40p - ADC40n| < E_{max_{40}}. \tag{3.2}$$

This first condition guarantees that the registered events in the spectrum are related to a specific scattering angle, defined by the intersection of a p and n strips. However, this is not enough for filtering non physical events since, in all cases in which $ADC40p$ is lower than $E_{max_{40}}$ and $ADC40n$ approximately zero (or vice versa), or in those situations in which both *ADC* channels are triggered by noise in low channels, the first

condition is met. For removing non-physical events, a second condition is imposed in addition to the first one:

$$[(ADC40p) > E_{min_p}].and.[(ADC40n) > E_{min_n}]. \tag{3.3}$$

E_{min_p} and E_{min_n} are adjusted to values high enough to remove as much noise as possible without removing physical events.

The distance between the two detectors in the telescopes, around 7 mm, implies that particles crossing one pixel from the ΔE detector may impact in several pixels in the second stage of the telescope, depending on the scattering angle. In this way, to obtain the two-dimensional spectrum related to a pixel in a 40 μm detector, it is necessary to add the spectra obtained considering several pixels in the E detector. In order to generate the spectrum for a specific pixel in E, a condition similar to Eq. 3.2 must be introduced:

$$|ADC1000p - ADC1000n| < E_{max_{1000}}. \tag{3.4}$$

This way of obtaining two-dimensional spectra, as an addition of several, implies the need to calibrate in energy all ADC channels, in such a way that not only the elastically scattered ^{8}He, but also the reaction fragments ^{6}He and ^{4}He, are adequately aligned in energy, making possible the identification of different reactions channels according to the kinematics of the process.

Other effects that should be taken into account at this point are the so-called interstrip effects [87, 88]. There are mainly two of those effects: the "charge-sharing", originated in the case that the charges are collected by two or more neighbouring strips and the "cross-talking", which causes electrically induced signals in these strips which are capacitively coupled. In order to remove interstrip effects another set of conditions is imposed. In particular, the conditions are such that the signals from all the strips different to the ones that are being plotted are kept below a certain value in energy. In this way, the particles which produce a charge shared between neighbouring strips are not considered.

Useful two-dimensional spectra, i.e., those in which integration regions can be applied, are then generated through Eq. 3.1, imposing the mentioned conditions (Eqs. 3.2, 3.3 and 3.4 and the interstrip conditions).

An example of the code written in ROOT in order to obtain the spectrum for a pixel in a 40 μm detector and a specific pixel in the 1 mm detector is presented in appendix A.

3.1.1 Energy calibrations

The calibration of the detection system was carried out, using a triple-alpha source, for both energies, 16 and 22 MeV. The triple-alpha source consists of three alpha emitters, namely, ^{239}Pu, ^{241}Am and ^{244}Cm. The energy (around 5 MeV) and intensity of the emitted alphas are summarized in table 3.1. The calibration procedure followed had the disadvantage that, as there were not enough space between the two stages of the

telescope for introducing the alpha source and ensuring the integrity of the detectors at the same time, E detectors were calibrated facing the source to the ohmic side. This side could introduce significant energy losses due to the usual aluminium metallization and un-depleted silicon layers. For this reason, while the calibration of ΔE detectors has been rather straightforward (for both p and n strips), the calibration of E detectors has been more elaborated.

Nucleus	Emitted alpha energy (keV)	Intensity (%)
^{239}Pu	5156.6	70.77
	5144.3	17.11
	5105.5	11.94
^{241}Am	5485.6	84.80
	5442.8	13.10
^{244}Cm	5804.8	76.90
	5762.6	23.10

Table 3.1: *Characteristic emissions of the triple-alpha source used for calibrations [1].*

For each ADC, a calibration spectrum is obtained, where the three main alpha peaks are present. Fitting each of the three peaks by a Gaussian distribution and following the χ^2 criterion for evaluating the quality of the fit, the ADC channel corresponding to centre of these distributions can be found. Each one of these channels corresponds then to an emitted energy from the triple alpha source in such a way that linear calibration equations can be obtained.

3.1.1.1 Calibration of the 40 μm detectors

The energy loss of the relevant reaction fragments in the ΔE detectors is expected to be around 5 MeV. As the irradiation was performed directly on the junction side, which is windowless (the normal aluminium layer has been replaced by an open grid) [66], no dead layer correction is necessary. In this way, the calibration is obtained directly from the linear fits mentioned above, so that calibration coefficients (a, b, c, d) in equations as $E_{40_p} = a \cdot ADC_{40_p} + b$ or $E_{40_n} = c \cdot ADC_{40_n} + d$ can be defined, being 40_p and 40_n a p and n strips of a 40 μm detector respectively.

3.1.1.2 Calibration of the 1 mm detectors

Unlike 40 μm detectors, the calibration with the triple alpha source of the 1 mm detectors can not be made directly as, during the process of calibration, the source was placed in front of the face where the metallization layer is found and where a dead layer, produced by an incomplete depletion due to an insufficient applied voltage, would appear. As it has been mentioned, both the dead and metallization layers can cause a loss of energy, in principle unknown, of the alpha particles emitted by the triple source. In addition, the E detector should cover much wider energy range, up to

$\sim$15 MeV. Therefore, the calibration has been performed with both the triple alpha source and the corresponding elastic peak. The procedure is explained below following an specific example, the calibration of $ADC361$ from telescope F.

The process of calibration begins obtaining an equation of the type $E_{1000} = a \cdot ADC_{1000} + b$ following the same procedure as for the 40 μm detectors. From this initial calibration, a first estimation of the energy deposited in the 1 mm detectors by the elastically scattered ^{8}He can be obtained as $E_{elas-initial} = a \cdot ADC_{elast} + b$, being ADC_{elast} the ADC channel where the elastic is found.

For $ADC361$, the first calibration performed only with the triple alpha source is the following:

$$E_{ADC361} = 10.11 \cdot ADC361 - 865.13 \ (keV). \tag{3.5}$$

The elastic peak in this ADC is centred in channel 1798 so the value obtained for $E_{elas-initial}$ is 17.310 keV.

The energy of an elastically scattered ^{8}He nucleus when it reaches a particular telescope can be calculated from the beam energy, the kinematics of the reaction and the energy loss in the target, which depends on its thickness and position.

In the case of study, a pixel in the 40 μm detector defined as the intersection of the ADC's 169 (p) and 179 (n), located in an observation angle of 59°, is taken as a reference. Considering the thickness of the target for this angle, the elastically scattered ^{8}He nucleus leaves the target with an energy of 21.068 keV. As the calibration for the ADC's in the thin detector is known, the energy loss of the ^{8}He nucleus when it goes through it can be obtained and it turns to be 3.804 keV.

In this way, the real energy deposited in the E detector ($E_{elast-final}$) can be calculated subtracting the energy deposited in the ΔE detector to the energy of the nucleus calculated just after the target. For the example, the value of $E_{elast-final}$ is obtained as:

$$E_{elast-final} = 21.068 - 3.804 = 17.264 \ keV. \tag{3.6}$$

The difference between $E_{elast-initial}$ and $E_{elast-final}$ is introduced in the constant coefficient of the linear calibration equation in order to reproduce the energy of the elastic peak, giving rise to a new expression $E_{1000-real} = a \cdot ADC_{elast} + b'$, where the new constant can be thus determine as $b' = b + (E_{elast-final} - E_{elast-initial})$. For $ADC361$, $b' = -911.13$ so the final calibration results the following:

$$E_{ADC361} = 10.11 \cdot ADC361 - 911.13 \ (keV). \tag{3.7}$$

3.1.2 Definition of selection windows

The valid events associated to each reaction channel are obtained defining integration regions or selection windows on the ΔE-E$_{total}$ two-dimensional spectra. As it has been

indicated before, selection windows have been determined in "summed" spectra (i.e. two-dimensional spectra obtained from the addition of single spectra of pixels with a similar scattering angle), ensuring enough statistics.

The nuclear scattering with non-polarised ion beams generates a symmetric angular distribution. In such case, reaction fragments emitted with the same θ angle are located over conical surfaces with a semi-opening angle of θ and which vertex is placed in the scattering centre (target). Due to the fact that the detectors in GLORIA are plane surfaces tangent to a sphere centred in the target, reaction fragments corresponding to the same θ will be located in the geometrical intersection between the cone associated to θ and the plane of the detector, i.e., a conic section (see Fig. 3.2).

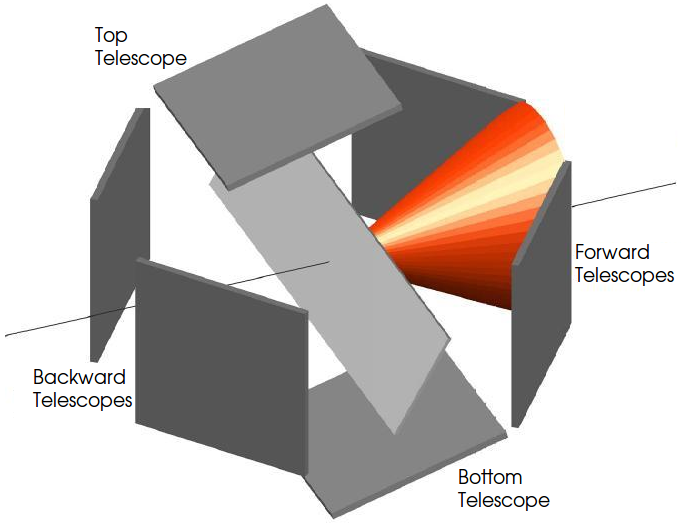

Figure 3.2: *Reaction fragments emitted with the same θ angle are located over conical surfaces which intersection with the planes of the detectors give rise to its positioning in geometric places with the shape of a conic section.*

The angular resolution of each pixel varies from 3° to 4°, depending on its position. The whole angular range covered by the detection system, from 15° to 165°, has been divided then in intervals, each generating over the plane of the detector two conic sections, one associated to the lower limit of the interval and one associated to the upper limit. Between them, some pixels are included in such way that they are considered as the pixels related to the mean θ angle of the interval, and they are used to generate the summed two-dimensional spectra ΔE-E$_{total}$ for this angle. The particular case of a forward telescope is shown in Fig. 3.3, where the pixels have been classified, as a function of their corresponding scattering angle, in 11 groups.

Proceeding like that, around 10 summed spectra are obtained per telescope, from which the selection windows are defined. However, once the selection windows are available, the analysis is carried out pixel by pixel, i.e., applying the window to the ΔE-E$_{total}$ of every particular pixel.

Nevertheless, during the analysis, a recurring effect has been observed, i.e. a double elastic peak have been found in some of the summed spectra. This is due to a non uniform thickness of the 40 μm detectors, so the energy deposited by reaction fragments with the same total energy varies from pixel to pixel. In Fig. 3.4 it can be observed

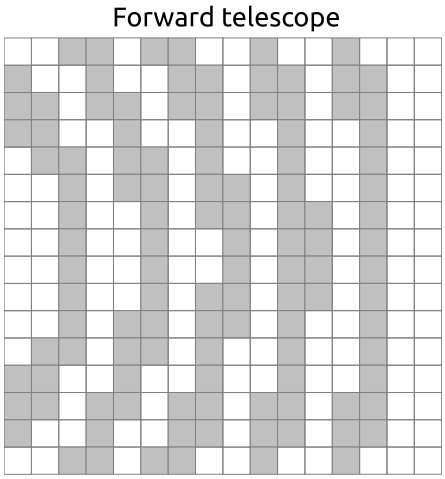

Figure 3.3: *The angular range covered by a forward telescope is divided in intervals, producing eleven groups.*

how, for the pixels of one of the regions between two of the conic sections defined (in particular the second region of the froward telescope A with a mean θ angle of 23°), two different summed spectra should be generated, as the elastic peak appears in a different position. This difference is even more clear if the elastic peak is projected over the vertical axis, as it is shown in Fig. 3.5.

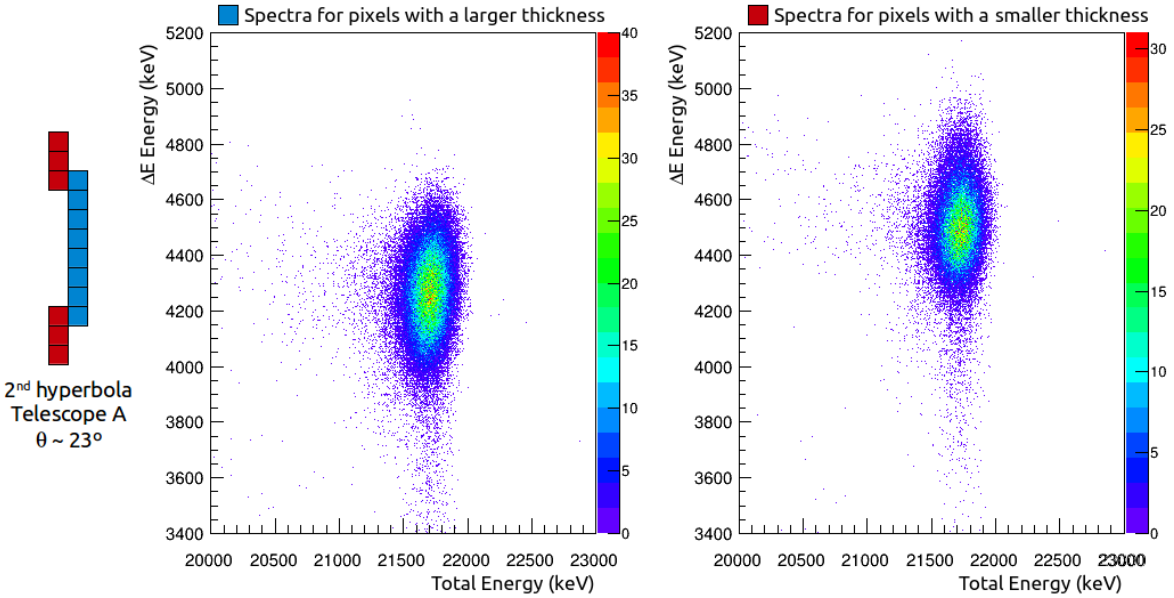

Figure 3.4: *(Left) Summed spectrum generated for the pixels with a larger thickness (depicted in blue in the diagram). (Right) Summed spectrum generated for the pixels with a smaller thickness (represented in red).*

This effect should be taken into account in order to properly define the selection windows. As the effect is related with detectors thicknesses, it will be present at both energies, 16 and 22 MeV.

Once the summed spectra is generated bearing in mind the mentioned effect, three

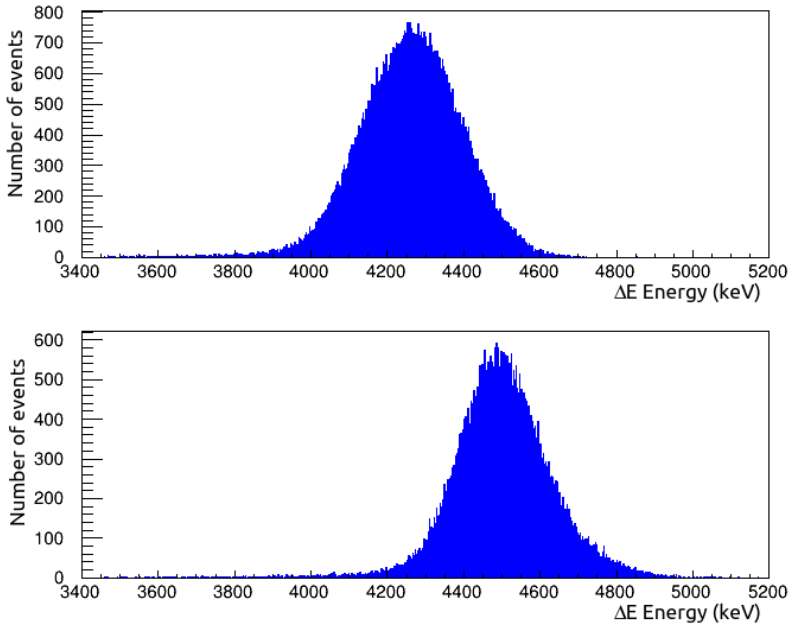

Figure 3.5: *Projection of the elastic peaks shown in Fig. 3.4 onto the vertical axis. A different position of these peaks is found for the two groups of pixels (those with a larger thickness (down) or smaller thickness (up)).*

main integration regions are defined:

- ^{8}He events.
- ^{6}He events.
- ^{4}He events.

In Fig. 3.6, an example of a ΔE-E$_{total}$ mass spectrum obtained for the top telescope E is shown, together with the selection windows corresponding to ^{8}He, ^{6}He and ^{4}He fragments. The mean θ value for the pixels included in this spectrum is 94.5°.

For the two-dimensional spectrum related to each pixel, the integration region is defined using the graphical cut class TCut defined in ROOT. The Tcut object is a closed polygon holding a closed region in the spectrum. Once every selection window is defined in terms of a graphical cut, the events within it are projected over the X axis, generating a monodimensional spectrum. By counting the events on it, the number of events inside the integration region are obtained. Each selection windows has then an associated monodimensional spectrum. In Figs. 3.7, 3.8 and 3.9 the monodimensional spectra obtained after applying the three main selection windows in 3.6 (^{8}He, ^{6}He and ^{4}He respectively) are shown.

The integration process is done for every run (data file) so that the number of ^{8}He, ^{6}He and ^{4}He events for each pixel is a sum over the total number of runs.

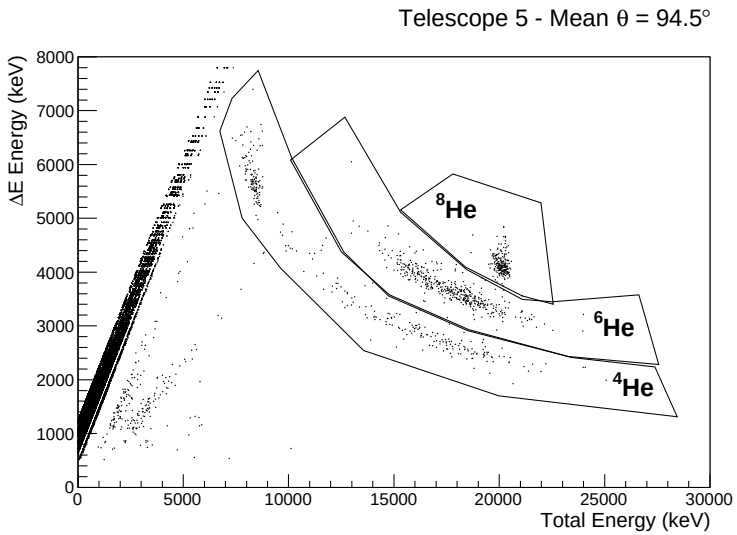

Figure 3.6: *Mass spectrum ΔE-E_{total} obtained for the top telescope (E). Selection windows corresponding to ^8He, ^6He and ^4He reaction fragments are shown.*

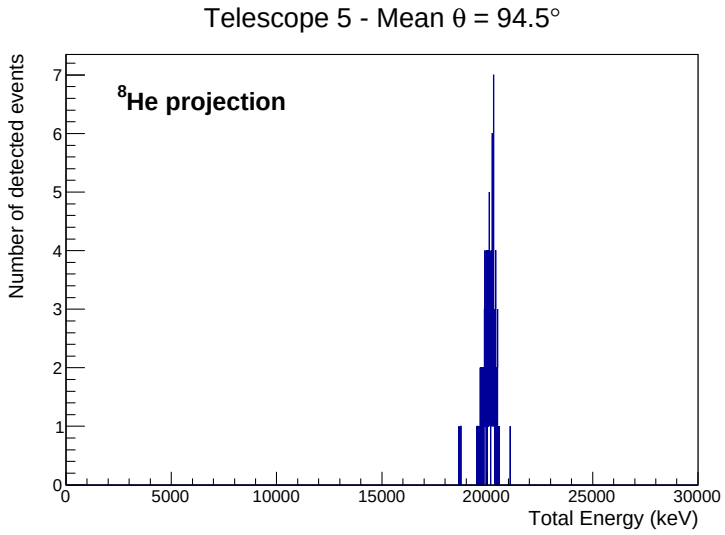

Figure 3.7: *Number of ^8He detected events/8 keV represented versus the total energy. This monodimensional spectrum is obtained through the projection, over the X axis, of the events within the selection window for ^8He defined in Fig. 3.6.*

3.2 Experimental corrections

Once the number of events corresponding to every reaction channel is determined, some corrections should be done as a consequence, mainly, of the efficiency of the detection system. This efficiency depends, essentially, on the intrinsic efficiency of detectors (a 100% can be considered for silicon detectors) and the electronic chain.

Regarding the efficiency of electronic chains, during all the experiment, test signals, coming from a pulse generator module or "pulser", were sent to the preamplifiers with the aim of estimating the efficiency of the electronic chain associated to each telescope.

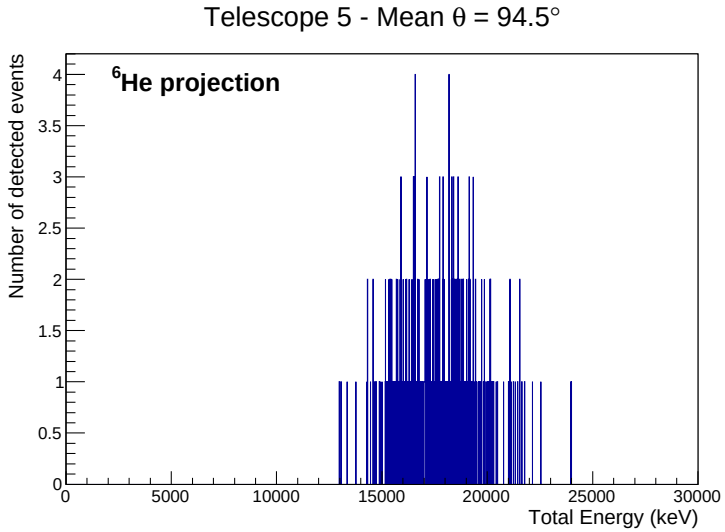

Figure 3.8: *Number of ^{6}He detected events/8 keV represented versus the total energy. This monodimensional spectrum is obtained through the projection, over the X axis, of the events within the selection window for ^{6}He defined in Fig. 3.6.*

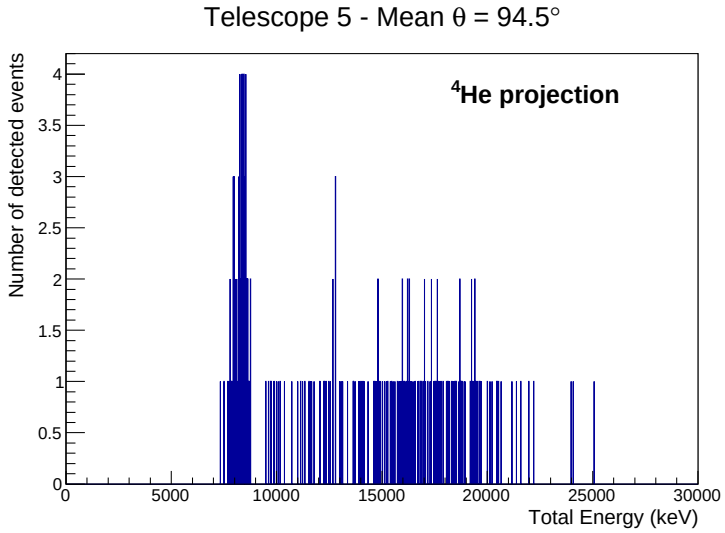

Figure 3.9: *Number of ^{4}He detected events/8 keV represented versus the total energy. This monodimensional spectrum is obtained through the projection, over the X axis, of the events within the selection window for ^{4}He defined in Fig. 3.6.*

As a consequence of the characteristics of those pulser signals, which are kept constant through time and sent to each detector at the same time, it is expected that all the pixels will register the same number of pulser events, in which case, the efficiency of all the electronic chains will be the same. However, the number of pulser events registered by all detectors is not exactly the same and a correction factor must be defined.

The correction due to the efficiency of the electronic chains is calculated as indicated in Eq. 3.8

$$k_p = N_p / N_{p(reference)}, \tag{3.8}$$

where k_p is the correction factor, N_p the number of pulser events in the pixel under study and $N_{p(reference)}$ the number of events in the pixel taken as a reference for the correction of all others (a pixel in telescope E was chosen). The k_p factor, independent of θ, must be taken into account in the calculation of the cross sections. Telescope F did not receive pulser signal neither at 16 MeV nor at 22 MeV.

In Fig. 3.10, the number of pulser events registered by the pixels of each telescope, for the 16 MeV runs, is presented while, for the case of the 22 MeV data, the same representation is shown in Fig. 3.11. As it can be observed, the number of pulser events is similar in all telescopes (except in the bottom one (F) since no test signal was sent) and does not vary importantly within them.

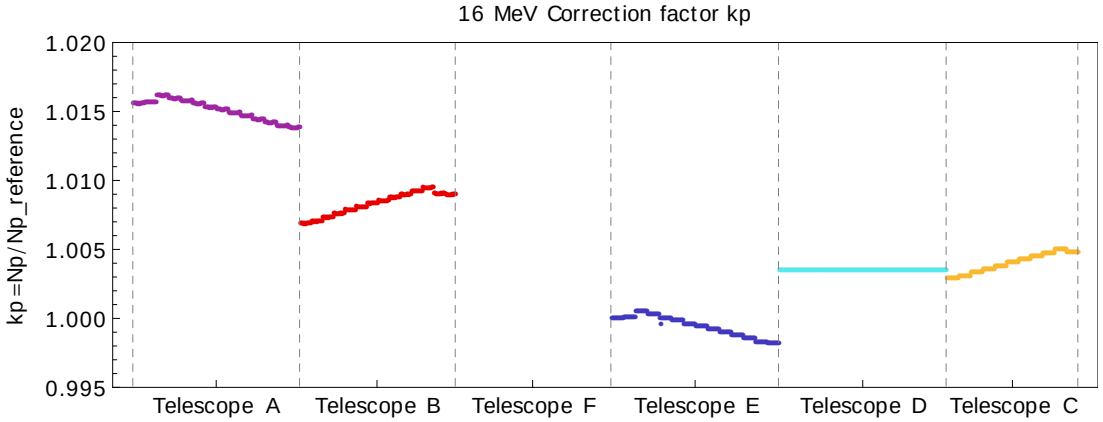

Figure 3.10: *Pulser events registered by every pixel of each telescope, for the 16 MeV runs. For this energy,* $N_{p(reference)} = 2.113.802$ *events.*

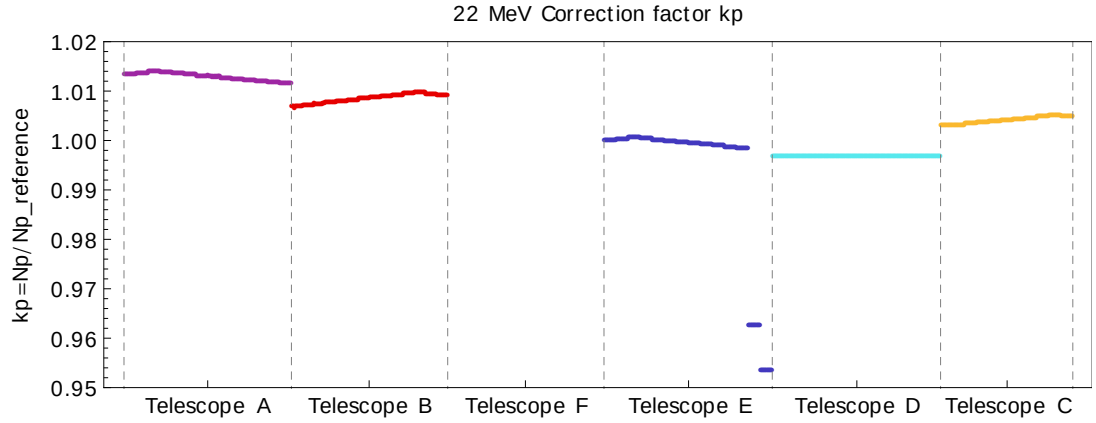

Figure 3.11: *Pulser events registered by every pixel of each telescope, for the 22 MeV runs. For this energy,* $N_{p(reference)} = 4.340.034$ *events.*

For telescope F, the correction due to the efficiency of the electronic chain is calculated afterwards, during the data analysis, in order to achieve the expected overlap with the contiguous telescopes (the forward ones A and B and the top telescope E).

Once the value of k_p has been calculated for each pixel, the number of elastic events it detects, N, is affected by this correction factor as shown is Eq. 3.9.

$$N_{corrected} = N/k_p. \tag{3.9}$$

3.3 Determination of the effective position of the beam-spot on target and the detectors array

For an accurate evaluation of the scattering angles and solid angles, an effective position of the beam spot on target and the detectors array should be considered. The search for this position is based on the idea that, at very forward angles, the ratio $d\sigma_{elastic}/d\sigma_{Rutherford}$ remains around one.

The search for the effective position is based on the following process. Firstly, an starting point position for the setup at each energy (16 and 22 MeV) must be found, taking into account considerations about the number of elastic events detected by the forward telescopes. Based on this position and following a specific methodology explained later in the text, several positions of the beam on target and setup are checked in order to find the best of them.

For the study of each one of the possible positions for the setup, a simulation considering a Rutherford scattering is carried out by means of the GEANT4 code [69, 70, 71], on a NPTool [72] environment, a set of subroutines initially developed for MUST2 and sufficiently tested with experimental measurements [62]. In each simulation, the geometry of the setup, according to the position being tested, must be implement. In this way, a number N_R of detected events is obtained for each pixel and the ratio $d\sigma_{elastic}/d\sigma_{Rutherford}$ can be calculated as the number of experimental elastic events (once affected by the correction due to the efficiency of the electronic chain, i.e. $N_{corrected}$) divided by N_R. For the simulations, in addition to the geometry of the setup, the size and tilted position of the target are taken into account, as well as some beam parameters as its characteristic dimension and energy spread. When defining the position of the different detectors in the simulation, it is also important to bear in mind that the assemblage of the ΔE detectors is not made directly over the supporting structure. Between both surfaces, a plastic washer of 1 mm thickness is introduced in order to guarantee electric isolation. In addition, it has to be taken into account the thickness of the PCB (2 mm in total) as the active silicon surface is place on its centre. Besides, the active surfaces of the ΔE and E detectors are separated a distance of around 7 mm.

The two typical input files for NPTool are shown in Fig. 3.12, where the target and the detector are specified, and in Fig. 3.13, where the beam parameters are described.

In order to cross-check the simulations, the number N_R has been also calculated, for several pixels, numerically, by means of the integration of the Rutherford cross section, as it will be explained afterwards.

For GLORIA detection system, when the position of the beam on target is the

```
%%%%%%%%%%Target%%%%%%%%%%%%%%%%%%%
%Thickness in micrometer
%Radius in mm
%Temperature in K, Pressure in bar
%Material name according to the target library
%%%%%%%%%%%%%%%%%%%%%%%%%%%%%%%%%%%%
GeneralTarget
%%%%%%%%%%%%%%%%%%%%%%%%%%%%%%%%%%%%
Target
        THICKNESS= 1.15
        ANGLE= +30
        RADIUS= 8
        MATERIAL= 208Pb
        NBLAYERS= 50
        X= 0
        Y= 0
        Z= 0
%%%%%%%%%%Detector%%%%%%%%%%%%%%%%%%%
%%Position and R given in mm
%%Angle given in degree
%%Option: 0,1 for Si SiLi and CsI
%%Option: all or sensible for VISualisation
%%%%%%%%%%%%%%%%%%%%%%%%%%%%%%%%%%%%
GaspardTracker
%%%%%%%%%%%%%%%%%%%%%%%%%%%%%%%%%%%%
GPDDummyShape
        X1_Y1=          26.20   57.83   33.50
        X16_Y1=         -23.80  57.83   33.50
        X1_Y6=          26.20   18.40   64.25
        X16_Y16=        -23.80  18.40   64.25
        FIRSTSTAGE= 1
        SECONDSTAGE= 1
        VIS= all
```

Figure 3.12: *Typical NPTool input file regarding the target and the detector. For the target, the thickness in μm, radius in mm, angle of rotation with respect to the vertical plane and material are introduced. For the detector, the position of its four corners is introduced through this file. Other parameters as the distance between the two stages of the telescope and their thicknesses or the energy resolution of the detectors should be also specified.*

nominal, i.e. the beam impinges in the centre of the target, which is the centre of the whole system, the same statistics is expected for symmetric positions, in particular, for the two forward telescopes as well as for the two backward ones (right-left symmetry). In principle, the maximum of events would be expected in the centre of those telescopes in such a way that the strips just above and below the centre would register the same number of events. However, it is necessary to remember the tilted position of the target which introduces itself an asymmetry between the upper and lower halves of these telescopes. This fact must be also addressed.

3.3.1 Cross-check of the simulations

The ratio $d\sigma_{elastic}/d\sigma_{Rutherford}$, as explained before, is calculated for each pixel dividing the number of experimental elastic events already corrected, $N_{corrected}$, by N_R, the

```
%%%%%%%%%%%%%%%%%%%%%%%%%%%%%%%%%%%%%%%%%%%%%%%%%%%%%%%%%%%%%%%%%%%%%%%%%%%%
%%%  Reaction file for 208Pb(8He,8He)208Pb reaction  %%%%%%%%%
%%%%%%%%%%%%%%%%%%%%%%%%%%%%%%%%%%%%%%%%%%%%%%%%%%%%%%%%%%%%%%%%%%%%%%%%%%%%
%%Beam energy given in MeV ; Excitation in MeV
Beam
  Particle= 8He
  Energy= 22.0
  SigmaEnergy= 0.44
  SigmaThetaX= 0.00
  SigmaPhiY= 0.00
  SigmaX= 1.5
  SigmaY= 1.5
  MeanThetaX= 0
  MeanPhiY= 0
  MeanX= 0
  MeanY= 0
%%%%%%%%%%%%%%%%%%%%%%%%%%%%%%%%%%%%%%%%%%%%%%%%%%%%%%%%%%%%%%%%%%%%%%%%%%%%
TwoBodyReaction
  Beam= 8He
  Target= 208Pb
  Light= 8He
  Heavy= 208Pb
  ExcitationEnergyLight= 0.0
  ExcitationEnergyHeavy= 0.0
  CrossSectionPath= ruthe_de100_a145.txt   CS
  ShootLight= 1
  ShootHeavy= 0
%%%%%%%%%%%%%%%%%%%%%%%%%%%%%%%%%%%%%%%%%%%%%%%%%%%%%%%%%%%%%%%%%%%%%%%%%%%%
%ShootLight= 1 -> therefore we shoot light particle
%ShootHeavy= 0 -> therefore we DO NOT shoot heavy particle
```

Figure 3.13: *Typical NPTool reaction file. The relevant characteristics of the beam should be define, as the energy, energy spread, or the parameters SigmaX and SigmaY, related to the size of the beam spot. In this file it is also important to properly indicate the path of the file in which the cross section is specified.*

number of events detected when considering a Rutherford cross section. N_R can be obtained from a simulation, as it has been already mentioned. However, in order to check the numbers obtained, for several pixels, N_R has been calculated also numerically, using a code written in Mathematica [89].

In this code, firstly, for a given position of the setup, for which the simulation is also carried out, the geometric location of these pixels is determined. Subsequently, for each of them, the range covered both in θ and ϕ can be obtained and, once these values are known, the number N_R is calculated as the integral of the Rutherford cross section following Eq. 3.10:

$$N_R = k \int_{\Delta\Omega} \frac{d\sigma}{d\Omega}\Big|_{Rutherford} d\Omega = k \int_{\theta_{min}}^{\theta_{max}} \int_{\phi_{min}}^{\phi_{max}} \frac{d\sigma}{d\Omega}\Big|_{Rutherford} \sin(\theta) d\theta d\phi \qquad (3.10)$$

being θ_{min} and θ_{max} the minimum and maximum values of the range in θ covered by a pixel and ϕ_{min} and ϕ_{max} the minimum and maximum values for the range in ϕ. k is obtained in such a way that, for pixels at very forward angles, the ratio $d\sigma_{elastic}/d\sigma_{Rutherford}$ remains near one.

Once the numbers N_R for the considered pixels are known from both the simulation and the numerical integration of the Rutherford cross section, the ratios obtained are compared in Fig. 3.14. In the left panel of this figure, four pixels in a forward telescope, four in the top telescope and another four in the bottom one, have been considered. As it can be observed, the ratio calculated in both ways, through the simulation and numerically, are consistent. In the right panel, the comparison is focused on the pixels of a whole strip of a forward telescope. Once again the values are equivalent and, as a result, the simulations and the number of events N_R extracted from them are reliable.

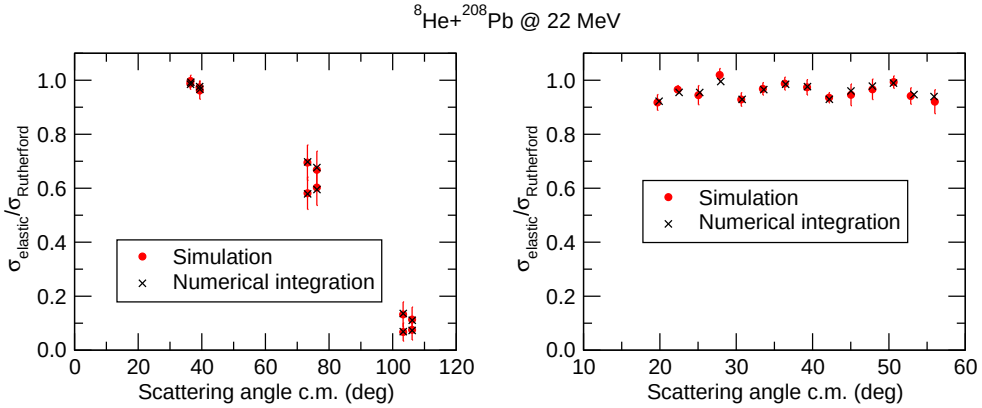

Figure 3.14: *(Left) Comparison, for various pixels in the setup, between the ratio $d\sigma_{elastic}/d\sigma_{Rutherford}$ obtained from the simulation and calculated numerically. (Right) The same comparison carried out for the strips of a whole strip of a forward telescope.*

3.3.2 Guiding the simulations

In order to find a starting point position for the setup, a comparison between the corrected elastic events $N_{corrected}$ detected by the two forward telescopes as well as between the upper and bottom halves of each of them should be carried out. For these studies, the number of events in each pixel have been normalised to the events registered by the pixel with more statistics, at each energy.

Regarding the comparison between telescopes, the colour code used in order to distinguish them, as well as the numeration used for the pixels, is shown in Fig. 3.15.

The results obtained for the pixels in the two first vertical strips at 16 and 22 MeV are shown in Fig. 3.16. As it can be observed, in the case of 16MeV, the forward telescope A detects more elastic events than the symmetric telescope B, a 10% more in average, while, for 22 MeV, the situation is the opposite and the number of events detected by telescope B a 4% larger. The 16 MeV data have been normalised with the number of events detected by the pixel with more statistics at this energy, 15.193 events. The same is done for 22 MeV, where the pixel with more statistics detects 22.209 events.

On the other hand, for the comparison between the upper and lower halves of the telescopes, the colour code and the numeration used for the pixels, is shown in Fig. 3.17.

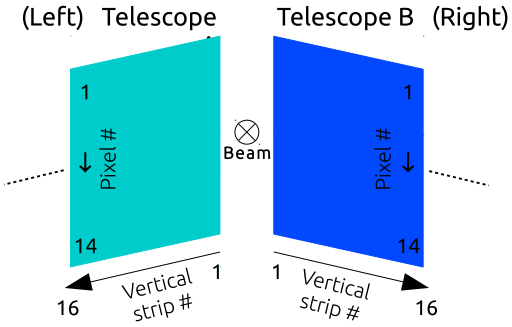

Figure 3.15: *The pixels in both forward telescopes are numbered from 1 (the most upper one) to 14 (the lower one). In order to better understand Fig. 3.16, telescope A is depicted in light blue while B in blue.*

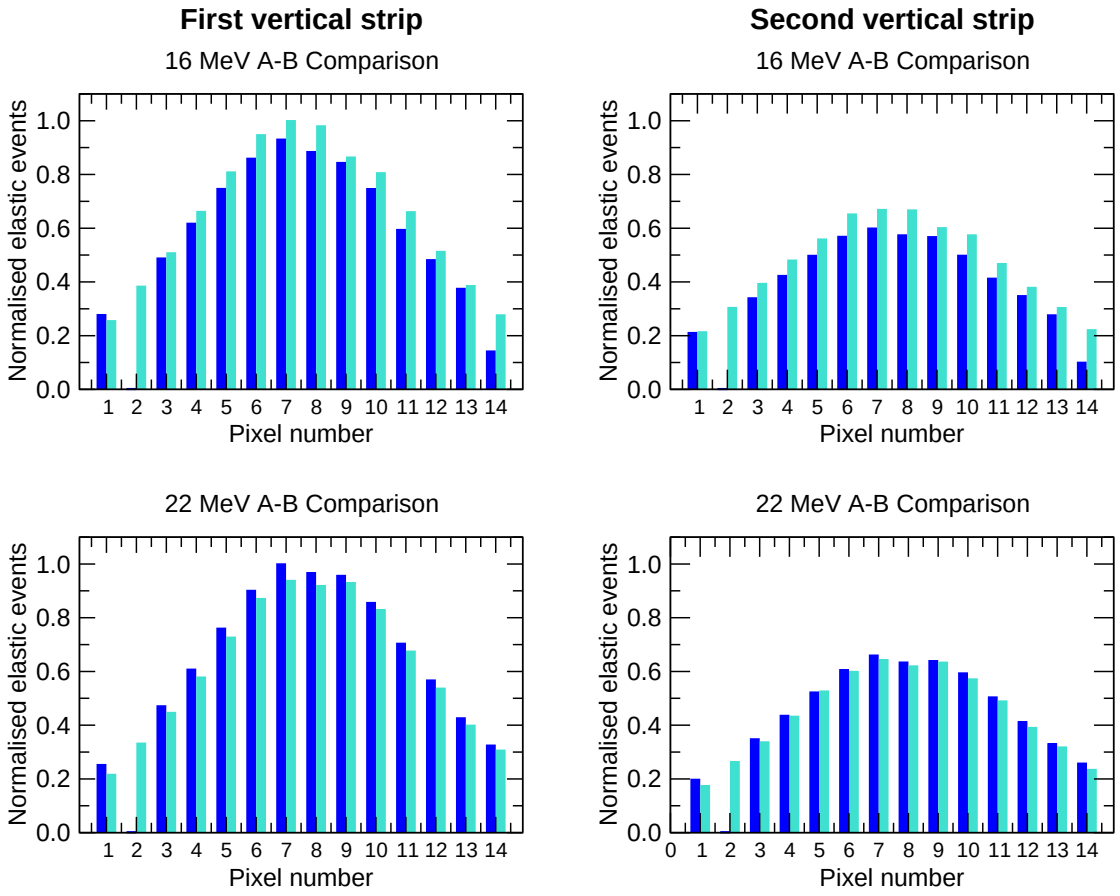

Figure 3.16: *Number of elastic events detected by the two first strips of the forward telescopes A and B in the case of 16 MeV (top panel) and 22 MeV (bottom panel). As mentioned in the text, the data have been normalised with the number of events detected by the pixel with more statistics at each energy. No error bars are included as they are not clearly visible in these bar diagrams. However, they are kept, for all pixels, under a 1.5%.*

For 22 MeV, as it can be observed in the top panel of Fig. 3.18 where the number of detected elastic events is represented for two vertical strips of telescope A, the lower half is detecting systematically more than the upper half as it also happens for telescope B, represented in the bottom panel. In the case of 16 MeV, as shown in Fig. 3.19, the differences between the upper and lower halves are not as clear as for 22 MeV. The value of these up-down differences has been evaluated following Eq. 3.11. For 22 MeV, the differences obtained are presented in the top panel of Fig. 3.20 where it is shown how they increase from around a 4% in the centre of the detector to nearly 40% in the edges. In the case of 16 MeV, however, they are kept, mainly, under a 5%, as it can be observed in the bottom panel of Fig. 3.20.

$$\delta(\%) = 100 \cdot |\frac{N_{up} - N_{down}}{N_{up}}| \tag{3.11}$$

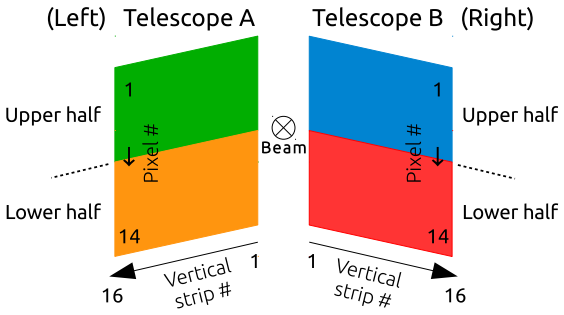

Figure 3.17: *The pixels in both forward telescopes are numbered from 1 to 14 as in Fig. 3.15. In order to better understand Figs. 3.18 and 3.19, the upper and lower parts of telescope A are depicted in green and orange while the upper and lower parts of telescope B are represented in blue and red respectively.*

In order to understand the most probable direction of the expected displacements, in Fig. 3.21 a top view of the setup is represented (left) together with a side view (right) where the origin (centred in the target) and orientation of the coordinate axes are shown. The positive Z axis direction corresponds to the direction of the beam while X is the vertical axis.

As mentioned before, for 16 MeV, telescope A detects more elastic events that telescope B. As it can be understand from Fig. 3.21, this effect should be translated into a displacement of the effective position of the beam on target in the negative direction of Y axis or, which is the same, a movement of the setup in the opposite direction. It can be also explained as a negative turn around the vertical axis (Z over Y) which approaches the beam axis to telescope A. In the case of 22 MeV, a movement of the setup in the negative direction of Y is expected instead. In this point, and in order to understand the differences between the upper and lower parts of the telescopes, mainly at 22 MeV, the influence of the rotation of the target must be introduced.

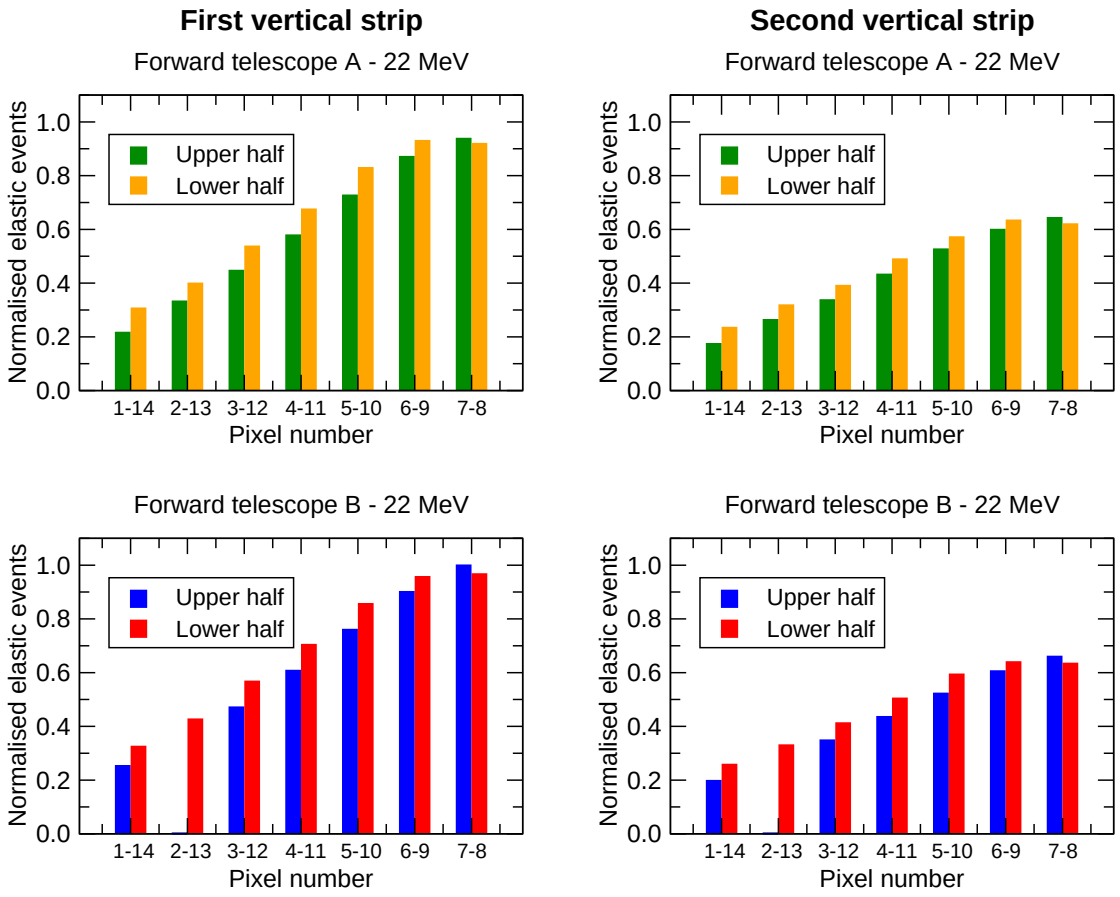

Figure 3.18: *Comparison between the detected elastic events by the upper and lower halves of the two first vertical strips of telescopes A and B at 22 MeV. Pixels in the upper half and in the lower one are represented in blue and red respectively. The data have been normalised with the number of events detected by the pixel with more statistics at 22 MeV, 22.209 events. For all pixels errors are kept under a 1.5%.*

3.3.3 Influence of the rotated position of the target

As it has been mentioned before, the tilted position of the target could imply an asymmetry in the number of events detected by the upper and lower halves of the forward and backward telescopes. Due to the fact that this asymmetry exists in the experimental data, it is important to study the possibility that it is as consequence of the 30° rotation of the target or even a rotation different from the nominal one.

Despite the design of the setup establishes a nominal target rotation of 30°, there is a range of possible values for this turn, between 15° and 45°, in which the target do not produce shadow in the detectors. Therefore, with the aim of determining if the differences between the upper and lower halves of the telescopes are due to the target rotation (the nominal one, or a different one within the possible range), five simulations are carried out for five possible turns: 15°, 22.5°, 30°, 37.5° and 45°. Positions out of this range are not considered as no shadowing is observed in the experimental data. In all the simulations no other movements of the setup are considered.

From these simulations, the differences in % between the number of elastic events

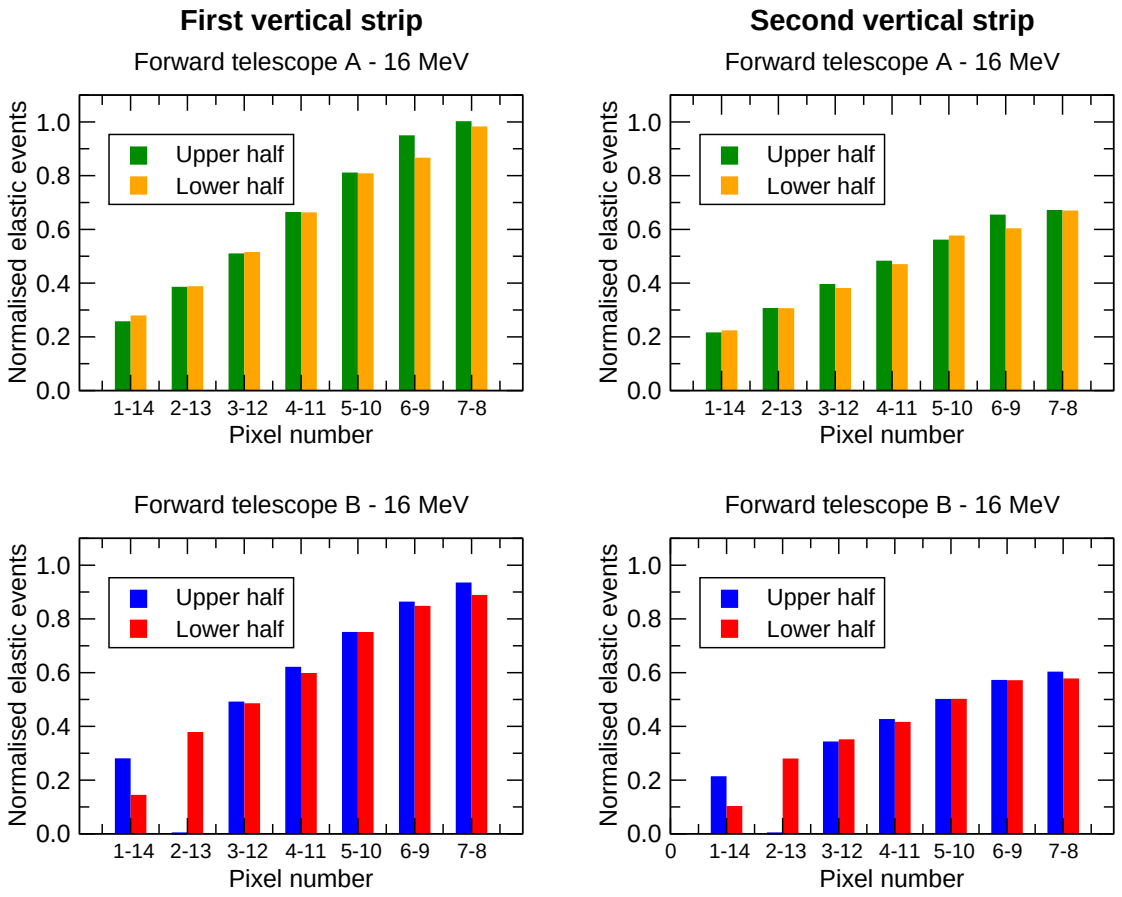

Figure 3.19: *Comparison between the detected elastic events by the upper and lower halves of the two first vertical strips of both telescopes A and B at 16 MeV. Pixels in the upper half and in the lower one are represented in blue and red respectively. The data have been normalised with the number of events detected by the pixel with more statistics at 16 MeV, 15.193 events. For all pixels errors are kept under a 1.5%.*

detected by the pixels in the upper and lower halves of the forward telescopes are evaluated following Eq. 3.11. As an example of the results obtained, in Fig. 3.22 the up-down differences for the set of pixels corresponding to the first vertical strip of telescope B are shown in the top panel while the differences for the pixels in the second strip are presented in the bottom panel. Again, the numeration of pixels is such that 7 and 8 are the ones located in the centre of the telescope while 1 and 14 are the outermost ones.

The main conclusion extracted from Fig. 3.22 is that the differences are kept, mainly, under a 3%, regardless of the rotation of the target. However, as it can be observed, there are not clear tendencies in the evolution of these differences within the telescopes, for any of the simulations. This can be explained, partly, as a consequence of a tangled combination of effects. As an illustration, it is worth to mention that, as the target decreases its rotation (it becomes more vertical), the solid angle of the pixels in the upper half of the detectors increases, while the target moves away from them. However, the effect is the opposite for the pixels in the lower half.

In general, from the analysis of the influence of the rotation of the target, two

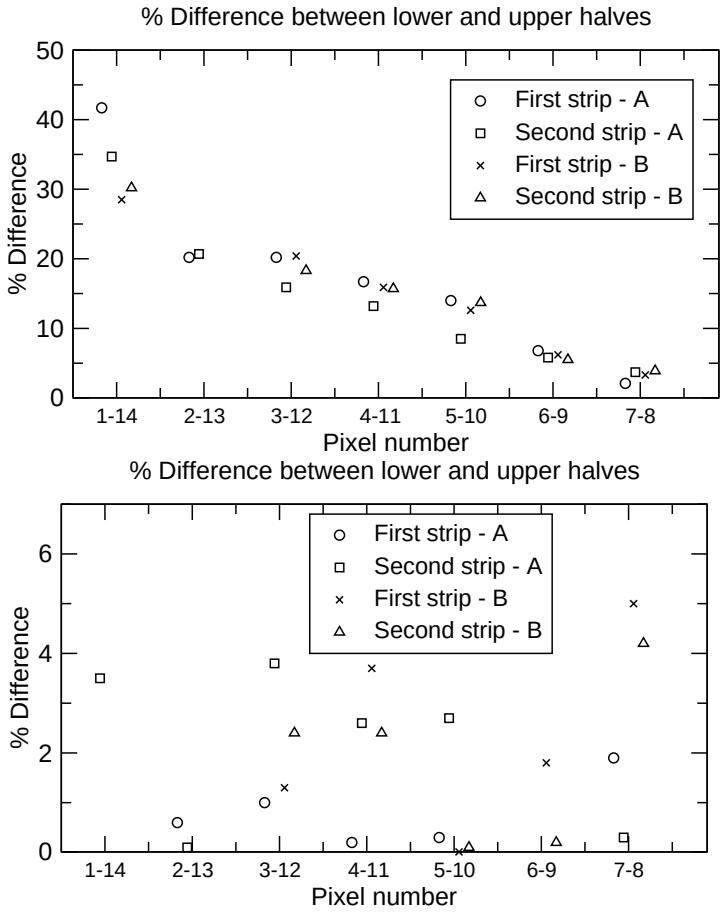

Figure 3.20: *(Top panel) Difference expressed in %, between the number of elastic events detected, at 22 MeV, by the upper and lower halves of the forward telescopes A and B, in particular, for the pixels of the two first vertical strips. (Bottom panel) The same differences represented for the case of 16 MeV.*

conclusions are obtained. On one hand, in relation to 16 MeV, the up-down differences, already shown in the bottom panel of Fig. 3.20, can be sufficiently explained with the asymmetry produced by the nominal rotation of the target. Thus, there are not signals pointing to a different rotation during the experiment. On the other hand, for 22 MeV, the up-low differences in the experimental data, presented in the top panel, are much larger than the ones introduced by the nominal rotation of the target or any different rotation (in the allowed range between 15° and 45°), according to the simulations. As a consequence, a vertical movement of the setup is expected in order to reach the best effective position at this energy.

3.3.4 Method for obtaining the best effective position

Once there is a starting point position for the setup in the sense that it is known that certain displacements may occur in order to explain, not only the left-right differences when comparing the number of elastic events detected by the forward telescopes, but also the up-low differences which cannot be explained by means of the rotation of the

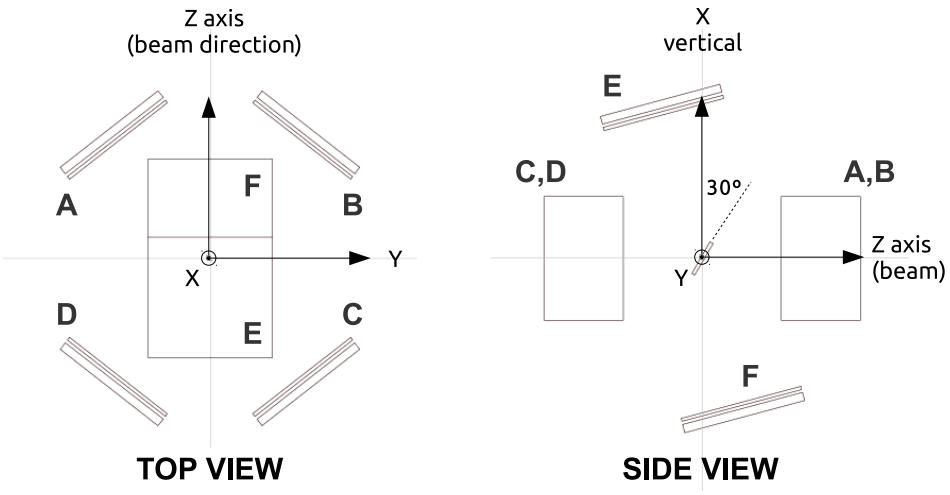

Figure 3.21: *(Left) Top view of the setup and (right) side view. The origin of the axes is located in the centre of the target.*

target, the methodology for obtaining the best position is the following:

- A set of 14 pixels (the most forward ones) of strips 1 and 2 from both telescopes A and B is chosen as in them a Rutherford-like behaviour is expected. Therefore, a total of 28 pixels are studied.
- For a given position of the telescopes, taking into account the considerations given at the beginning of subsection 3.3 about the assemblage of the detectors, a simulation is carried out (in the terms indicated above), getting as a result the ratios $d\sigma_{elastic}/d\sigma_{Rutherford}$ for each pixel.
- When the ratios for the 28 pixels are obtained, they are fitted with a line which slope should be as close as possible to zero while the differences between those ratios and the line (following the χ^2 method) should be minimum.

It is important to remark that all the possible movements of the setup are correlated, producing different assignments for the scattering and solid angles. In any case, in the search for the best effective position, these movements are treated independently. That means that, according to the starting point position, a first study is carried out in order to obtain one of the possible displacements (leaving all the rest fixed at zero) and then, this is followed by another study in which the already determined movement is taken as a basis, and so on. The nominal position of the detection system, which will be mentioned in the following studies corresponds to the position of design.

3.3.5 Determination of the effective position at 22 MeV

In the first place and following the methodology explained below, a study is made with the aim of determining the effective vertical displacement, taking into account that

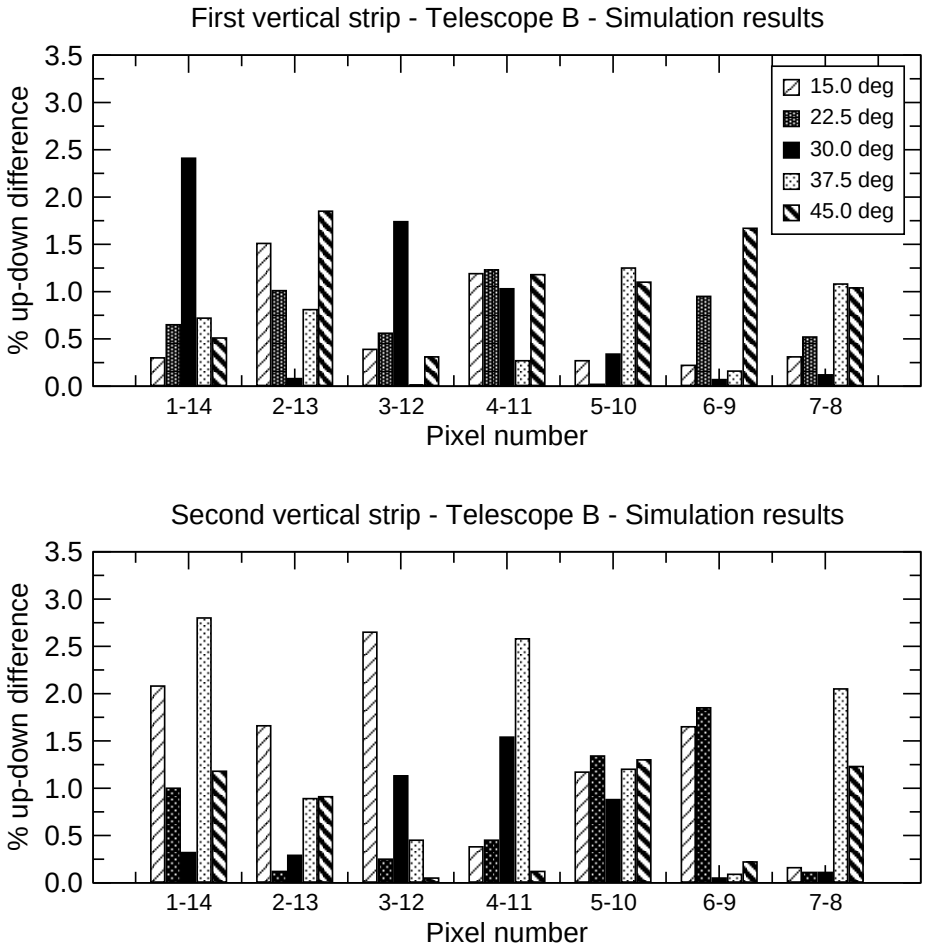

Figure 3.22: *Differences, in %, between the number of elastic events detected by the pixels in the upper and lower halves of the first (top panel) and second (bottom panel) vertical strips of the forward telescope B, for the five simulations performed. Each simulation correspond to a different rotation of the target, in particular, 15°, 22.5°, 30° (nominal position), 37.5° and 45°.*

its direction is known from the comparisons in the number of elastic events detected. In particular eleven positions are evaluated: 0.00 mm, 0.25 mm, 0.50 mm, 1.00 mm, 1.10 mm, 1.15 mm, 1.20 mm, 1.30 mm, 1.50 mm, 1.75 mm and 2.00 mm. In table 3.2 relevant information for these positions, i.e. the slope for each linear fit and the value of the χ^2 for each of them, is presented. For a better understanding of this table, the χ^2 values as well as the slopes obtained in every position are shown, respectively, in Fig. 3.23 left and right.

As it can be observed in Fig. 3.23, the vertical movement for which a minimum slope is achieved corresponds to a displacement of 1.20 mm. For this case, the χ^2 obtained is also small in comparison with other positions.

Once a vertical displacement of 1.20 mm has been determined, there is still a difference in the number of elastic events detected by the symmetric telescopes A and B as it has been already commented and shown in Fig. 3.16. For this reason, a second study is made in order to determine if these differences are due to an effective horizontal displacement. Again, 5 possible horizontal movements are evaluated: from

Vertical Displacement (mm)	χ^2 (N_f=25)	Slope
2.00	263.88	0.0034
1.75	188.96	0.0037
1.50	98.98	0.0059
1.30	107.72	0.0035
1.20	**95.77**	**0.0007**
1.15	85.72	0.0033
1.10	118.48	0.0058
1.00	104.53	0.0024
0.50	112.79	0.0046
0.25	322.30	0.0215
0.00	277.07	0.0157

Table 3.2: *Summary of the χ^2 and slope values for the linear fits of the ratios obtained for the most forward pixels of telescopes A and B, in the case of vertical displacements and not considering the rest of possible movements. This information corresponds to 22 MeV. The vertical movement for which a minimum slope is achieved as well as a reasonable χ^2 value, has been highlighted.*

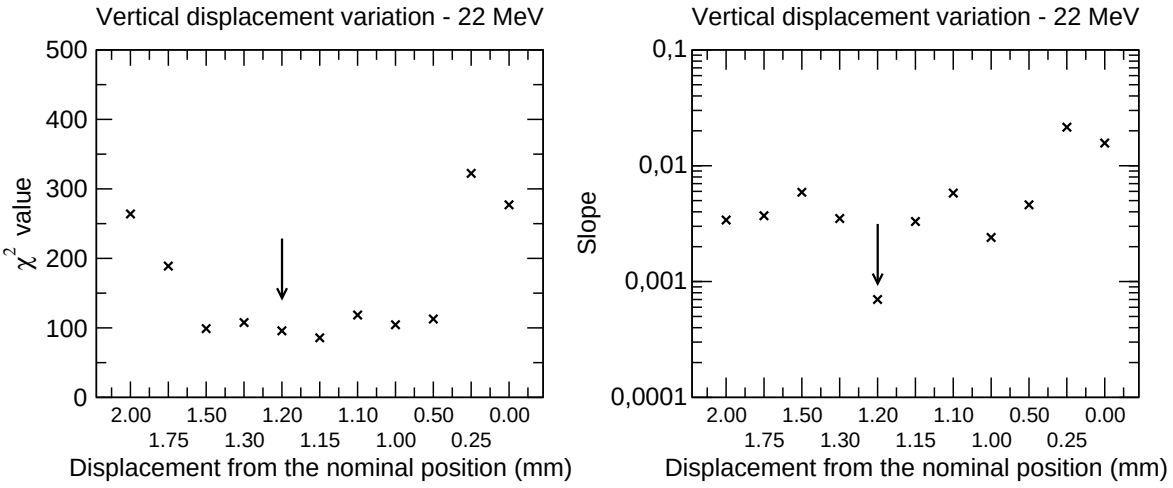

Figure 3.23: *(Left) χ^2 values obtained for different vertical displacements in the range between 0.00 mm and 2.00 mm, when no other displacements are considered. (Right) Slopes of the linear fits.*

-0.30 mm to 0.30 mm in steps of 0.15 mm. In table 3.3 the information derived from this study is summarized while, in Fig. 3.24 the χ^2 values (left) and the slopes of the linear fits (right) obtained for each position are presented.

In this case, the position in which the value of the χ^2 is minimum as well as the value of the slope of the corresponding linear fit is such that there is no horizontal displacement, that is, there is no horizontal movement that improves the assignment of scattering and solid angles. For this reason, another study should be carried out.

Horizontal Displacement (mm)	χ^2 (N_f=25)	Slope
- 0.30	199.16	0.0141
- 0.15	105.28	0.0044
0.00	**95.77**	**0.0007**
0.15	202.04	0.0017
0.30	410.82	0.0163

Table 3.3: *Summary of the χ^2 and slope values for the linear fits of the ratios obtained for the most forward pixels of telescopes A and B, in the case of horizontal displacements (keeping the vertical displacement fixed in 1.20 mm) and not considering the rest of possible movements. This information corresponds to 22 MeV. The horizontal movement for which the slope and the χ^2 value are both minimum has been highlighted.*

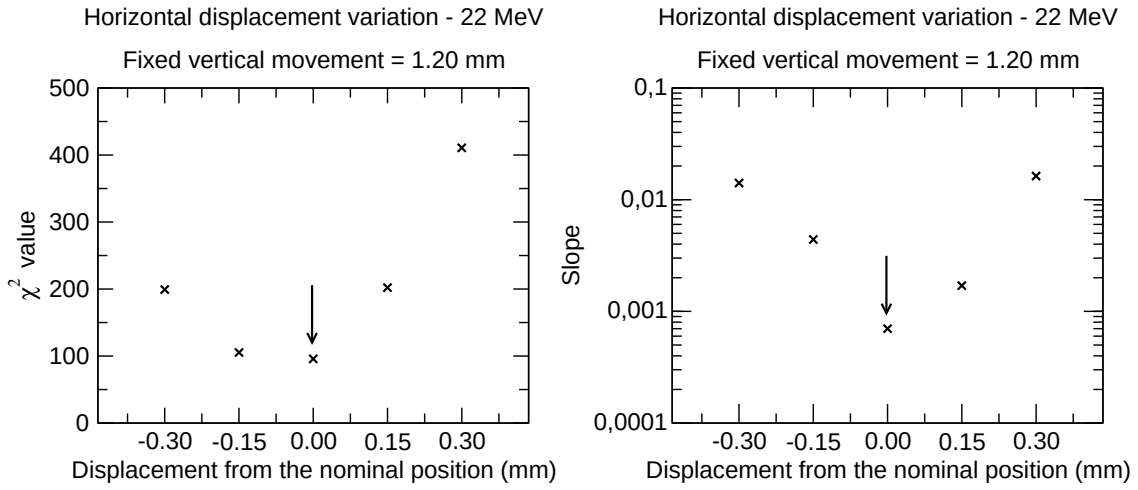

Figure 3.24: *(Left) χ^2 values obtained for different horizontal displacements in the range between -0.30 mm and 0.30 mm (for a given vertical movement of 1.20 mm). (Right) Slope values for the linear fits for these positions.*

In particular, a third movement, a turn around the vertical axis, which produces a left-right asymmetry between the elastic events detected by telescopes A and B, is tested. Six different turns are checked: -0.10°, 0.00°, 0.05°, 0.10°, 0.15° and 0.20°, considering a vertical displacement of 1.20 mm and no horizontal movement. The relevant information of this study can be found in table 3.4, and, as for the previous positions, the χ^2 values and slope for the fit in each position are presented in Fig. 3.25 (left and right respectively).

Finally, the position determined by a vertical movement of 1.20 mm plus a turn around the vertical axis of 0.05° has been chosen as the effective position as it is the case in which the value for the χ^2 is minimum as well as the slope of the line which fits the ratio for the 28 pixels evaluated. As it has been mentioned before, the ratio $d\sigma_{elastic}/d\sigma_{Rutherford}$ is calculated for each pixel dividing the number of elastic events by the number N_R of events from the simulation. As this ratio should remain approximately constant, it is expected that the behaviour of the simulated events and

↻ around vertical axis	χ^2 (N_f=25)	Slope
-0.10°	161.05	0.0060
0.00°	95.77	0.0007
0.05°	**67.73**	**0.0001**
0.10°	90.51	0.0043
0.15°	104.97	0.0020
0.20°	132.07	0.0025

Table 3.4: *Summary of the χ^2 and slope values for the linear fits of the ratios obtained for the most forward pixels of telescopes A and B, in the case of turns around the vertical axis (keeping the vertical displacement fixed in 1.20 mm and not considering any horizontal displacement). This information corresponds to 22 MeV. The value of the turn for which both the slope of the linear fit and the χ^2 value are minimum has been highlighted.*

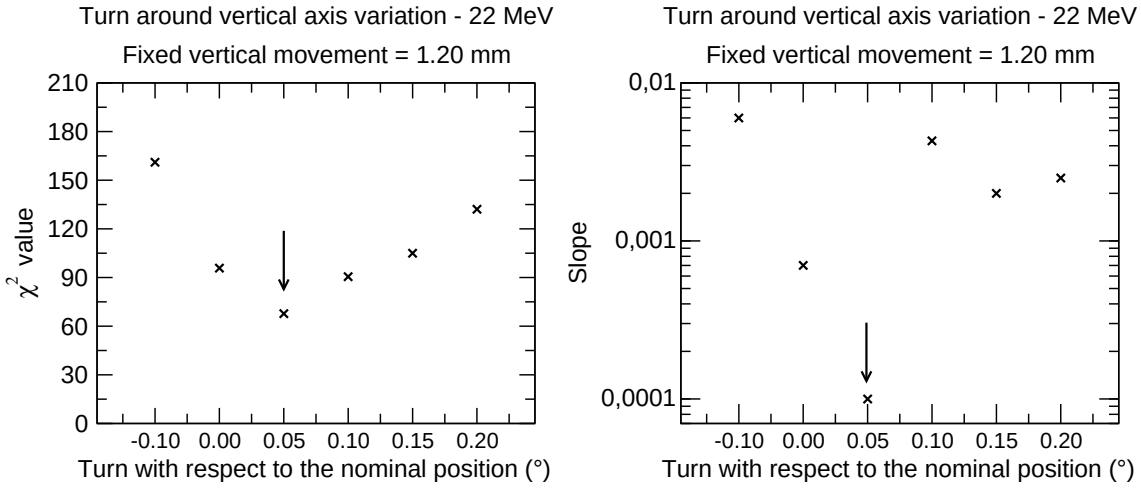

Figure 3.25: *(Left) χ^2 values obtained for different turns around the vertical axis, in the range between -0.10° and 0.20° (for a given vertical displacement of 1.20 mm). (Right) Slope values for the linear fits for these positions.*

the experimental elastic events is the same. In Fig. 3.26 the comparison between the real experimental data and the simulations results for the chosen effective position are shown for the set of pixels corresponding to the two first vertical strips of telescope A (top panel) and telescope B (bottom panel) at 22 MeV.

3.3.6 Determination of the effective position at 16 MeV

For 16 MeV, as the differences between the upper and lower halves of the forward telescopes are not as clear as for 22 MeV, a first study is performed in order to understand the differences in the number of detected events between these telescopes (left-right asymmetry) which, as it has been explained before, may be due to horizontal displace-

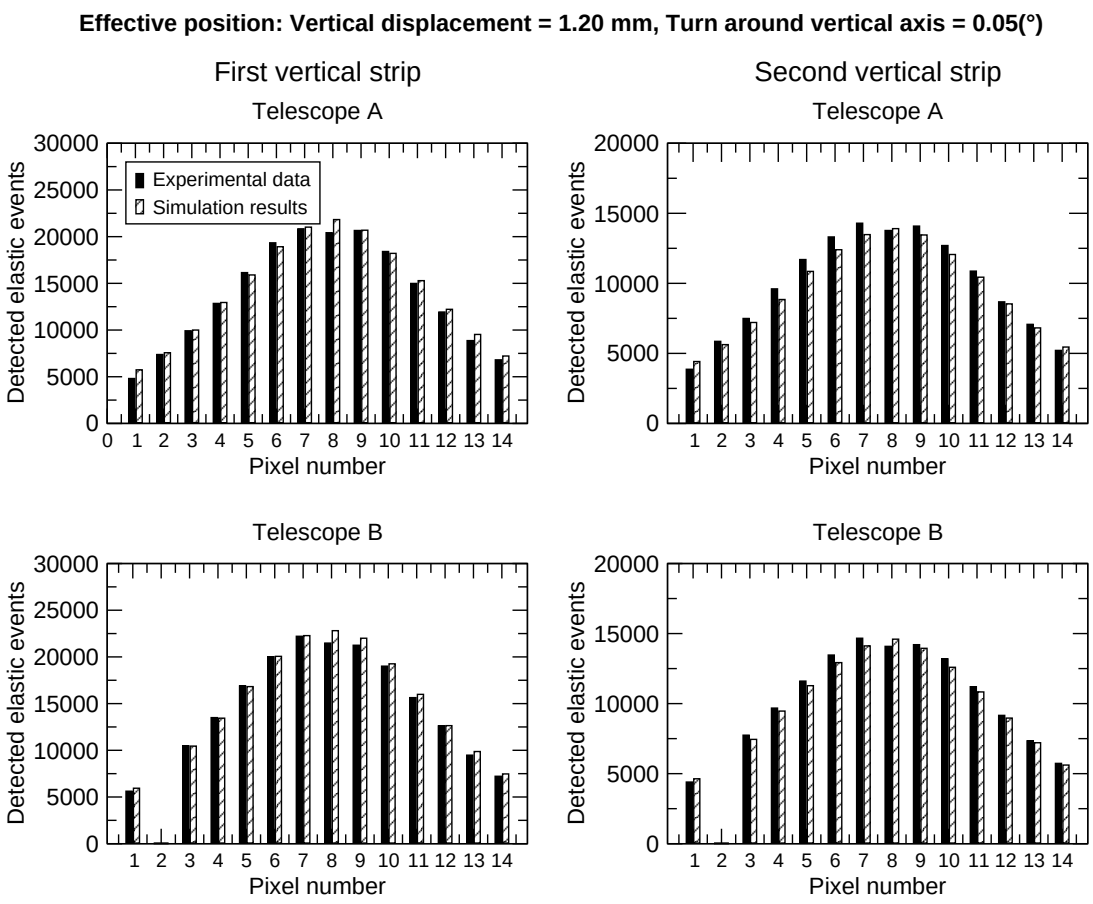

Figure 3.26: *Comparison, for the pixels in the two first vertical strips, between the experimental elastic events detected and the events obtained from the simulation in the chosen effective position, for telescope A (top panel) and B (bottom panel) at 22 MeV.*

ments or turns around the vertical axis.

Starting with the horizontal movements, six different positions have been tested, in particular -0.15 mm, 0.00 mm, 0.15 mm, 0.30 mm, 0.45 mm and 0.60 mm. In table 3.5 the values obtained for the χ^2 and slope of the linear fits are shown, while their representation can be found in Fig. 3.27.

As it can be observed, in terms of slope, the horizontal displacement would be 0.15 mm while the best value of χ^2 is obtained in for a displacement of 0.30 mm. As the difference in the number of detected events by the forward telescopes can be also explained as a turn around the vertical axis, as it has been found for 22 MeV, a second study is carried out in order to determine if there is a value for this turn which improves the assignment of scattering and solid angles. As it has been discussed before, at 22 MeV telescope B detects, in average, a 4% more elastic events than telescope A which results in a turn around the vertical axis of 0.05°. At 16 MeV the situation is the opposite, i.e. telescope A counts more than B (with a bigger difference, around 10%) and therefore it is expected that the turn should be larger and in the opposite direction.

Eight different values for the turn around the vertical axis are checked: 0.15°, 0.00°, -0.15°, -0.30°, -0.40°, -0,45°, -0.50° and -0.60°. In table 3.6 the values obtained for the

Horizontal Displacement (mm)	χ^2 (N_f=25)	Slope
- 0.15	536.34	0.0136
0.00	330.63	0.0057
0.15	136.13	0.0001
0.30	76.51	0.0013
0.45	88.47	0.0057
0.60	122.68	0.0134

Table 3.5: *Summary of the χ^2 and slope values for the linear fits of the ratios obtained for the most forward pixels of telescopes A and B, in the case of horizontal displacements in the range between -0.15 and 0.60 mm, and not considering the rest of possible movements. This information corresponds to 16 MeV.*

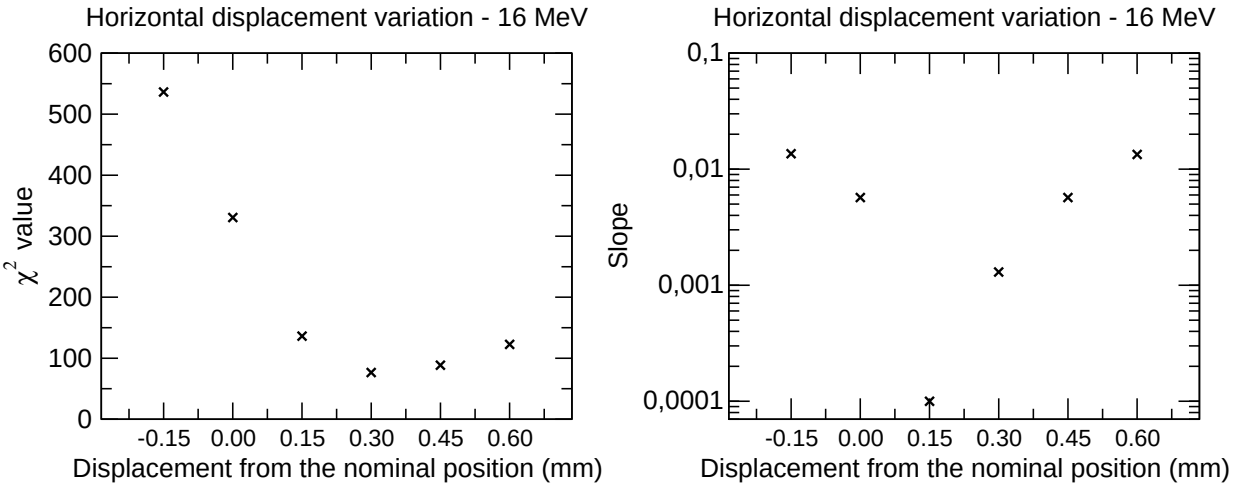

Figure 3.27: *(Left) χ^2 values obtained for different horizontal displacements around the nominal position, in the range between -0.15 mm and 0.60 mm, when only horizontal displacements are considered. (Right) Slope values for the linear fits for these positions.*

χ^2 and slope of the linear fits are shown, while their representation can be found in Fig. 3.28. In this case, the minimum value for the slope is determined by a turn around the vertical axis of -0.30°, position for which also the χ^2 remains among the best values obtained. The χ^2 value is, in addition, lower than the χ^2 values from the previous study where only horizontal displacements were considered. As expected, the turn is negative (it is positive for 22 MeV) and larger.

Once there is a movement which explains the differences in the number of detected events between the symmetric telescopes A and B, vertical movements can be studied with the aim of determining a better position. For this, 7 possible movements are checked: 0.20 mm, 0.10 mm, 0.05 mm, 0.00 mm, -0.05 mm, -0.10 mm and -0.20 mm. A summary of the χ^2 and slope values obtained for the the linear fits is presented in table 3.7, while their representation is shown in Fig. 3.29.

From this last study, it results that there is not a vertical movement that leads

↻ around vertical axis	χ^2 (N_f=25)	Slope
-0.60°	145.14	0.0226
-0.50°	78.65	0.0161
-0.45°	64.99	0.0142
-0.40°	54.31	0.0122
-0.30°	**66.82**	**0.0009**
-0.15°	144.65	0.0034
0.00°	330.63	0.0057
0.15°	624.76	0.0096

Table 3.6: *Summary of the χ^2 and slope values for the linear fits of the ratios obtained for the most forward pixels of telescopes A and B, in the case of turns around the vertical axis and not considering the rest of possible movements. This information corresponds to 16 MeV.*

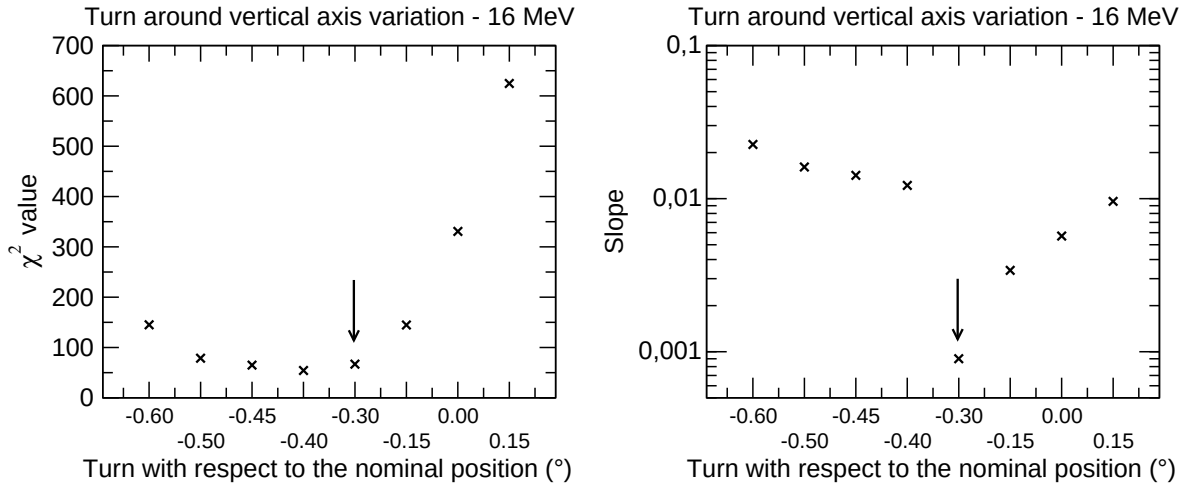

Figure 3.28: *(Left) χ^2 values obtained for different turns around the vertical axis, in the range between 0.15° and -0.60° when no other movements are considered. (Right) Slope values for the linear fits for these positions.*

to a better effective position of the setup. As a consequence, for 16 MeV the final position chosen as the effective position of the beam on target and the detectors array is determined by a turn of -0.30° around the vertical axis. The fact that it exists a difference between the number of elastic events detected by the upper and lower halves of telescopes A and B, but no vertical displacement is obtained, is consistent with the idea that the tilted position of the target is enough to explain this difference.

As it has been done for 22 MeV, in Fig. 3.30 the comparison between the real experimental data and the simulations results, for the effective position, are shown for the two first vertical strips of telescope A (top panel) and telescope B (bottom panel).

Summarizing, the effective position of the beam on target and the setup at 16 MeV results in a turn around the vertical axis of -0.30° while for 22 MeV it consists in a

Vertical Displacement (mm)	χ^2 (N_f=25)	Slope
0.20	65.45	0.0051
0.10	61.99	0.0038
0.05	68.16	0.0027
0.00	**66.82**	**0.0009**
-0.05	62.54	0.0038
-0.10	60.29	0.0033
-0.20	57.22	0.0053

Table 3.7: *Summary of the χ^2 and slope values for the linear fits of the ratios obtained for the most forward pixels of telescopes A and B, in the case vertical displacements (for a fixed value of -0.30° for the turn around the vertical axis) and not considering the rest of possible movements. This information corresponds to 16 MeV.*

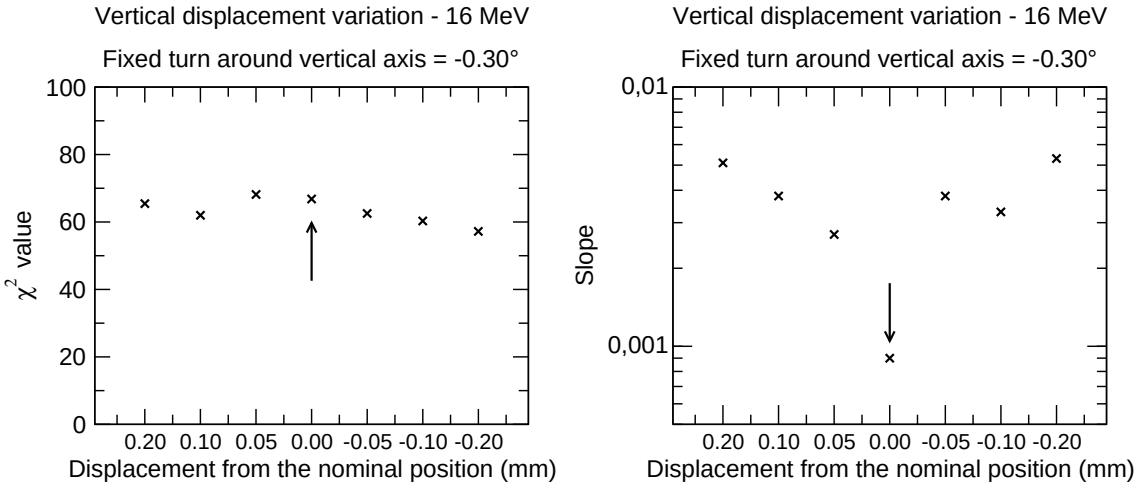

Figure 3.29: *(Left) χ^2 values obtained for different vertical displacements in the range between -0.20 mm and 0.20 mm, for a given turn of -0.30° around the vertical axis. (Right) Slope values for the linear fits for these positions.*

vertical displacement of 1.20 mm and a turn of 0.05°. The slope for the linear fit of the ratios (for the 28 pixels considered) is similar in both cases (0.0009 and 0.0001 respectively) as well as the χ^2 (66.82 and 67.73).

3.3.7 Obtaining scattering and solid angles

Once the effective positions of the beam on target and the detectors array have been found for 16 and 22 MeV, and in order to obtain the scattering and solid angles and calculate the ratio $d\sigma_{elastic}/d\sigma_{Rutherford}$ for each pixel of every telescope, simulations for the whole setup must be carried out. Each one of these simulations provide the scattering angle and the angular range of every pixel as well as the number of events N_R. N_R, as explained before, is the number of events registered by a pixel introducing,

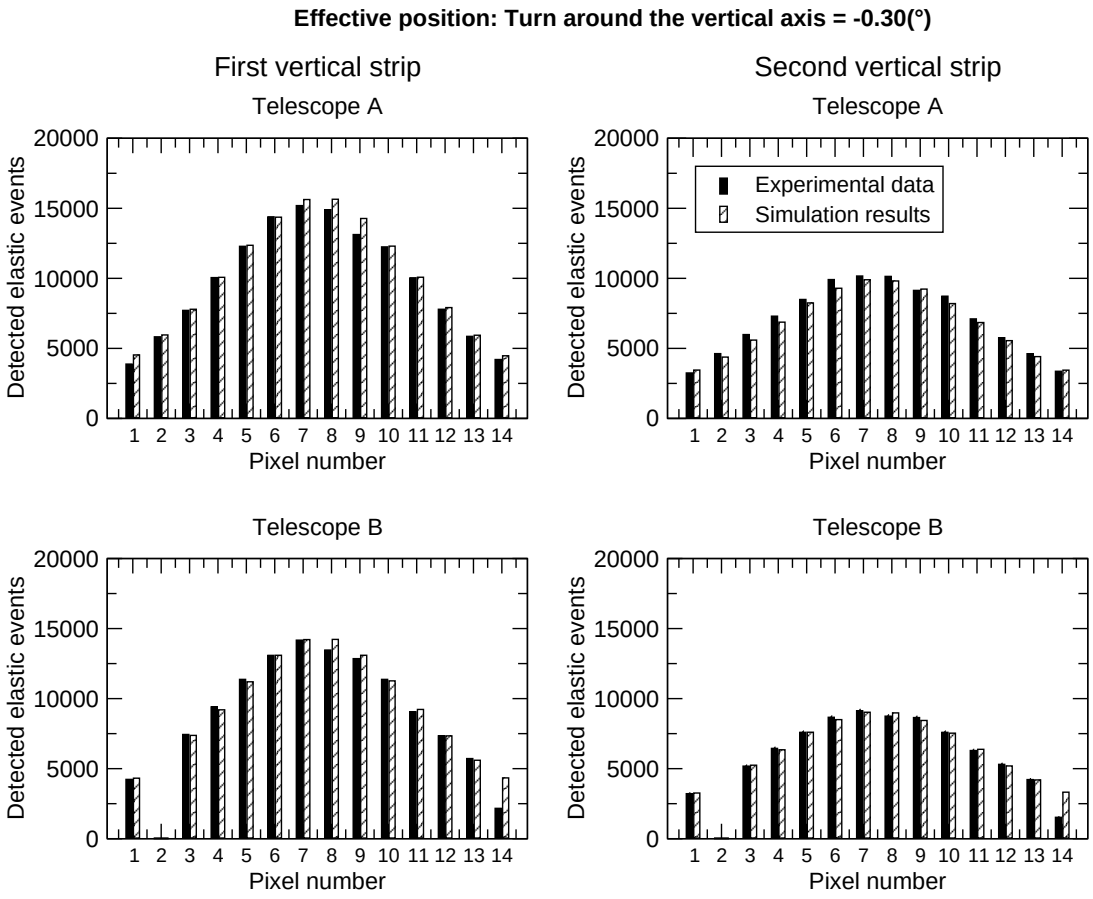

Figure 3.30: *Comparison, for the pixels in the two first vertical strips, between the experimental elastic events detected and the events obtained from the simulation in the chosen effective position, for telescope A (top panel) and B (bottom panel) at 16 MeV.*

as a input of the simulation, a Rutherford cross section.

The simulations are performed in such a way that the number N_R for every pixel is larger than 4000 which implies a maximum uncertainty of a 1.6%. It is important to have this value under control as it is taken into account in the calculation of the uncertainty of the ratio $d\sigma_{elastic}/d\sigma_{Rutherford}$. In order to obtain such a number of events there are mainly two options. The first possibility is to carry out a simulation of the whole setup, with a very large number of events. The second option is to perform several simulations, restricted to different parts of the setup, looking afterwards for a matching between them. In this case, the second option have been chosen, as it requires less computational time, and it produces smaller and more easy to handle data files. A more detailed explanation of the procedure followed for the matching of the different simulations performed can be found in appendix B.

3.4 Calculation of the ratio elastic over Rutherford cross section and its uncertainty

Once for every pixel i it is known:

- the number of experimental elastic events properly corrected in terms of the efficiency of the electronic chains, i.e. $N^i_{corrected}$,
- and the scattering and solid angles (θ_i, Ω_i) as well as the number of detected events N^i_R, considering a Rutherford cross section (from the simulations),

the elastic cross section normalised by the corresponding Rutherford cross section is calculated as shown in Eq. 3.12.

$$\frac{d\sigma(\theta_i)/d\Omega}{(d\sigma(\theta_i)/d\Omega)_{Ruth}} = K\frac{N^i_{corrected}}{N^i_R/C}, \tag{3.12}$$

being K a normalization constant which includes factors as the thickness of the target or the beam intensity, and C the matching constant between the simulation from which the value N^i_R is obtained and the simulation taken as a reference.

The uncertainty associated to the normalised cross section can be obtained using the most common formula for calculating error propagation (Eq. 3.13), i.e. the effect of variable's uncertainties on the uncertainty of a function based on them:

$$\delta(f) = \sqrt{\left(\frac{\partial f}{\partial x}\right)^2 S_x^2 + \left(\frac{\partial f}{\partial y}\right)^2 S_y^2 + \left(\frac{\partial f}{\partial z}\right)^2 S_z^2 + ...}, \tag{3.13}$$

where $\delta(f)$ represents the uncertainty associated to the function $f(x, y, z, ...)$, S_x the uncertainty of the variable x and so on.

Applying Eq. 3.13, and taking into account that the uncertainties of $N^i_{corrected}$ and N^i_R can be expressed respectively as $\sqrt{N^i_{corrected}}$ and $\sqrt{N^i_R}$, the uncertainty associated to the normalised cross section for a particular pixel i, $\delta(\frac{d\sigma(\theta_i)}{d\sigma(\theta_i)_{Ruth}})$, is calculated as shown in Eq. 3.14.

$$\delta(\frac{d\sigma(\theta_i)}{d\sigma(\theta_i)_{Ruth}}) = \frac{d\sigma(\theta_i)}{d\sigma(\theta_i)_{Ruth}}\sqrt{\frac{1}{N^i_{corrected}} + \frac{1}{N^i_R}} \tag{3.14}$$

Once the normalised elastic cross section and its uncertainty have been obtained for each pixel, the full angular range covered by the detection system is divided into intervals. For each pixel, the scattering angle (θ_i) and its uncertainty $(\delta\theta_i)$ are known so the width of the intervals has been taken as the average value of $\delta\theta_i$ for all the pixels in the setup, at each energy. Each interval is thus defined by a minimum and a maximum value of the scattering angle, θ^{min}_{int} and θ^{max}_{int} respectively. For each one of these intervals, it exists a group of M pixels which scattering angles can be found between these limits

and, for these pixels, an average normalised elastic cross section ($\frac{d\sigma(\theta_{int})}{d\sigma(\theta_{int})_{Ruth}}$) has been calculated following the general expression for the weighted arithmetic mean:

$$\bar{x} = \frac{\sum_{i=1}^{N} w_i x_i}{\sum_{i=1}^{N} w_i}, \tag{3.15}$$

where w_i are the weights. In this work, the weights have been chosen as the inverse value of the square of the normalised cross section's uncertainty:

$$w_i = \frac{1}{\delta(\frac{d\sigma(\theta_i)}{d\sigma(\theta_i)_{Ruth}})^2}. \tag{3.16}$$

As a result, the average normalised elastic cross section for each interval and its uncertainty have been obtained using Eqs. 3.17 and 3.18.

$$\frac{d\sigma(\theta_{int})}{d\sigma(\theta_{int})_{Ruth}} = \frac{\sum_{i=1}^{M}(\frac{d\sigma(\theta_i)}{d\sigma(\theta_i)_{Ruth}})/\delta(\frac{d\sigma(\theta_i)}{d\sigma(\theta_i)_{Ruth}})^2}{\sum_{i=1}^{M} 1/\delta(\frac{d\sigma(\theta_i)}{d\sigma(\theta_i)_{Ruth}})^2}, \tag{3.17}$$

$$\delta(\frac{d\sigma(\theta_{int})}{d\sigma(\theta_{int})_{Ruth}}) = \frac{1}{\sqrt{\sum_{i=1}^{M} 1/\delta(\frac{d\sigma(\theta_i)}{d\sigma(\theta_i)_{Ruth}})^2}}. \tag{3.18}$$

The scattering angle which corresponds to the interval, expressed in the equations above as θ_{int}, has been calculated from the scattering angles of the pixels contained in this interval, applying again the expression for the weighted arithmetic mean, as shown in Eq. 3.19. Its uncertainty, $\delta\theta_{int}$, has been calculated using Eq. 3.20.

$$\theta_{int} = \frac{\sum_{i=1}^{M} \theta_i/\delta(\frac{d\sigma(\theta_i)}{d\sigma(\theta_i)_{Ruth}})^2}{\sum_{i=1}^{M} 1/\delta(\frac{d\sigma(\theta_i)}{d\sigma(\theta_i)_{Ruth}})^2}, \tag{3.19}$$

$$\delta\theta_{int} = \frac{\sum_{i=1}^{M} \delta\theta_i/\delta(\frac{d\sigma(\theta_i)}{d\sigma(\theta_i)_{Ruth}})^2}{\sum_{i=1}^{M} 1/\delta(\frac{d\sigma(\theta_i)}{d\sigma(\theta_i)_{Ruth}})^2}. \tag{3.20}$$

The values obtained for the average normalised elastic cross section and the scattering angle, together with their uncertainties, for each one of the intervals, are summarized in appendix C.

3.5 Calculation of the ratios ^{6}He/^{8}He and ^{4}He/^{8}He and their uncertainties

For each pixel which have been analysed, not only the number of detected elastic events has been obtained, but also the number of ^{6}He and ^{4}He fragments registered. These fragments correspond to different reaction mechanisms which in principle can not be disentangled by means of the GLORIA detection system.

However, the study of the angular distribution of the ratios ^{6}He/^{8}He and ^{4}He/^{8}He, allows for an interpretation of the relative importance of the main reaction channels expected, as it will be explained in chapter 4. For this reason, for each one of the intervals in which the covered angular range has been divided in section 3.4, these ratios and their uncertainties have been calculated.

While in section 3.4 the scattering angle of a given interval has been expressed in the Center of Mass frame, for the ratios it has to be expressed in the laboratory frame and, consequently, the angle θ_{int} already calculated for each interval has been transformed into $\theta_{int,lab}$.

For the calculation of the ratios, the total number of fragments of ^{6}He or ^{4}He has been divided by the total number of elastic events detected by the M pixels within the interval, following Eqs. 3.21 and 3.22:

$$\frac{^6He}{^8He} = \frac{\sum_{i=1}^{M} N^i_{^6He}}{\sum_{i=1}^{M} N^i_{^8He}}, \tag{3.21}$$

$$\frac{^4He}{^8He} = \frac{\sum_{i=1}^{M} N^i_{^4He}}{\sum_{i=1}^{M} N^i_{^8He}}, \tag{3.22}$$

being $N^i_{^6He}$ and $N^i_{^4He}$ the number of ^{6}He and ^{4}He events detected by a pixel i and $N^i_{^8He}$ the number of elastic events registered by the same pixel before any correction. In the calculation of the ratios, no experimental corrections are introduced as their effects are cancelled.

The uncertainties of these ratios have been obtained applying the formula for the propagation of errors (Eq. 3.13) already presented in section 3.4:

$$\delta\left(\frac{^6He}{^8He}\right) = \frac{^6He}{^8He}\sqrt{\frac{1}{N^i_{^6He}} + \frac{1}{N^i_{^8He}}}, \tag{3.23}$$

$$\delta\left(\frac{^4He}{^8He}\right) = \frac{^4He}{^8He}\sqrt{\frac{1}{N^i_{^4He}} + \frac{1}{N^i_{^8He}}}. \tag{3.24}$$

The values obtained for both ratios, ^{6}He/^{8}He and ^{4}He/^{8}He, and the scattering angle (expressed in the laboratory frame), together with their uncertainties, for each one of the intervals, are summarized in appendix D.

4 Theoretical interpretation

In this chapter, the theoretical interpretation of the experimental angular distributions of the elastic scattering and the ^{6}He/^{8}He and ^{4}He/^{8}He ratios is presented.

Firstly, section 4.1 contains a summary of the experimental angular distributions. In section 4.2 the interpretation of the elastic channel by means of the application of the Optical Model is presented. Also, a CRC calculation is included. Sections 4.3 and 4.4 are dedicated to the ^{6}He/^{8}He and ^{4}He/^{8}He ratios and their interpretation with DWBA one-neutron and two-neutron transfer calculations.

It is important to note that this chapter is devoted to a preliminary interpretation of the experimental data through simple models. Further studies, including CRC and CDCC calculations, will be performed in the near future.

4.1 Experimental results

In Fig. 4.1, the angular distribution of the experimental ratio between the elastic cross section and the Rutherford cross section, for the colliding system ^{8}He+^{208}Pb at the energies E_{LAB} of 22 and 16 MeV, is presented. As it can be observed, below the barrier (E_B ~19 MeV) the cross section present a less pronounced reduction as the scattering angles increases than in the case above the barrier.

The ratios between the yields of ^{6,4}He and the elastically scattered ^{8}He, i.e. ^{6}He/^{8}He and ^{4}He/^{8}He, are shown at both energies in Figs. 4.2 and 4.3 respectively.

4.2 Interpretation of the elastic scattering

Firstly, a comparison with previous phenomenological potentials found in the literature have been carried out. Secondly, in order to reproduce the new elastic scattering data for the colliding system ^{8}He+^{208}Pb, the parameters defining these potentials have been adjusted, initially, for 22 MeV, as it is the energy above the barrier, where the optical

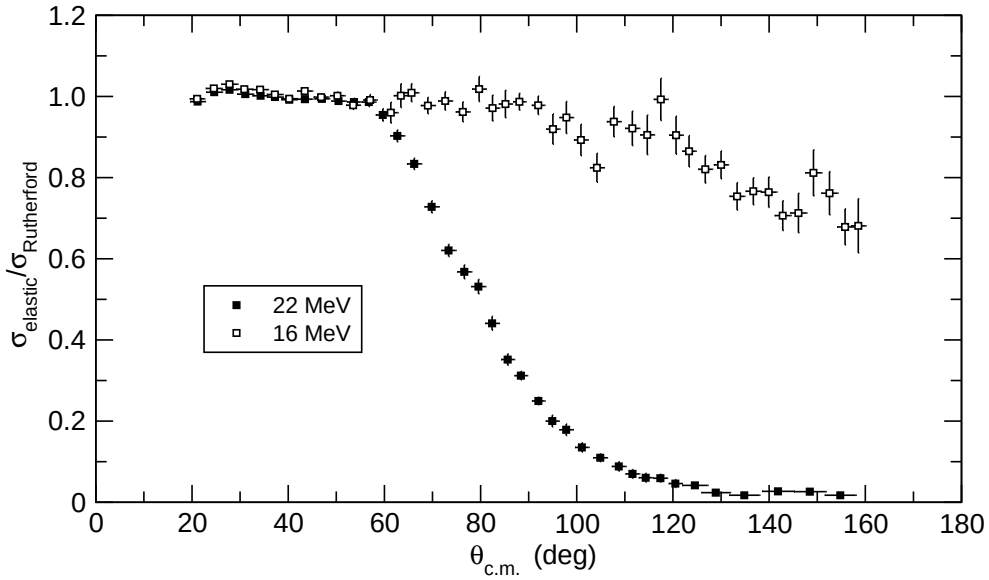

Figure 4.1: *Angular distribution of the ratio $d\sigma_{elastic}/d\sigma_{Rutherford}$ for the system $^{8}He+^{208}Pb$ at 16 MeV (open squares) and 22 MeV (filled squares).*

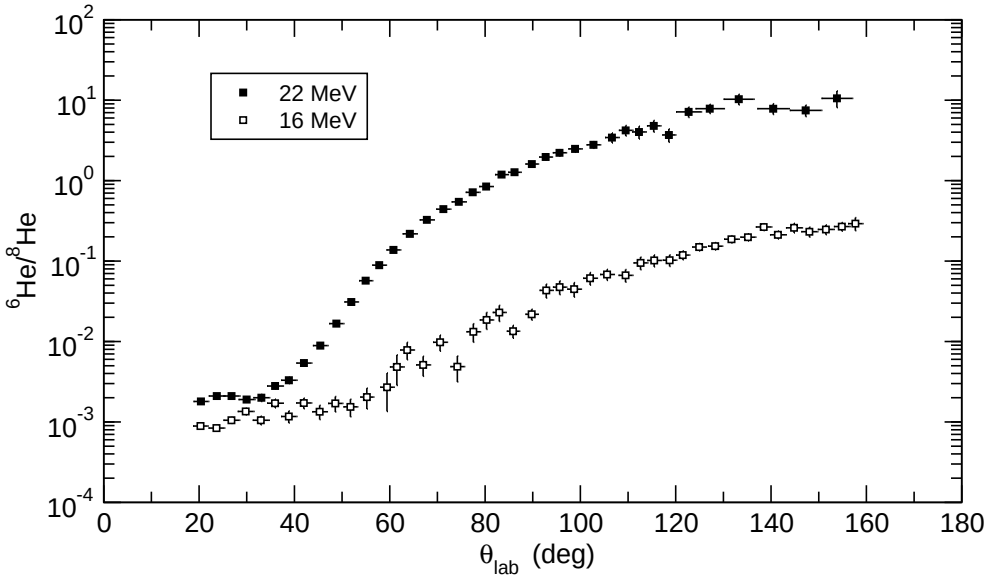

Figure 4.2: *Angular distribution of the ratio ^{6}He over ^{8}He at 16 MeV (open squares) and 22 MeV (filled squares).*

potential is more sensitive to the experimental data.

In particular, the global optical potentials describing the elastic scattering of ^{6,7}Li projectiles from [90] have been used. The global optical potential for ^{6}Li have been extracted after the fitting of a large number of experimental data sets for the elastic scattering from targets in a mass range between 24 and 208, at energies from 13 to 156 MeV, representing a total of 44 distributions and more than 2000 data points. For ^{7}Li, less data was available, being restricted to energies below 50 MeV. In any case, 25 distributions have been used (around 1000 data points). The global Optical Model (OM) parameters are presented in table 4.1.

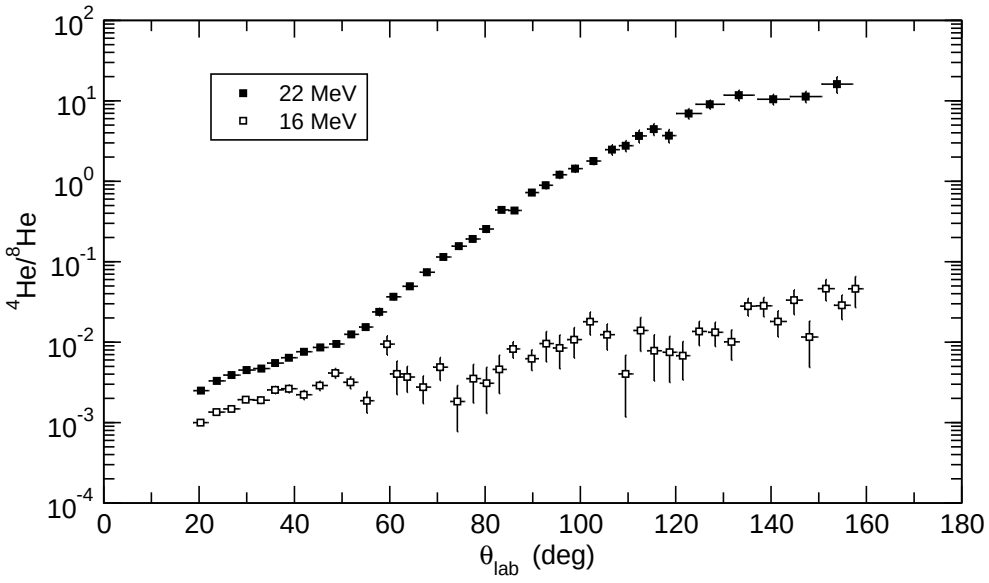

Figure 4.3: *Angular distribution of the ratio ^{4}He over ^{8}He at 16 MeV (open squares) and 22 MeV (filled squares).*

Global OM parameters for ^{6}Li					
V	r_R	a_R	W	r_I	a_I
109.5	1.326	0.811	58.16-0.328A+0.00075A^2	1.534	0.884
Global OM parameters for ^{7}Li					
V	r_R	a_R	W	r_I	a_I
114.2	1.286	0.853	40.13-0.341A+0.00093A^2	1.739	0.809

Table 4.1: *Global Optical Model parameters for describing the elastic scattering of ^{6}Li and ^{7}Li from [90]. Potential depths are expressed in MeV while radii and diffusenesses are expressed in fm. The parameter A stands for the mass number of the target.*

A first comparison between the experimental angular distribution of the ratio $d\sigma_{elastic}/d\sigma_{Rutherford}$ for ^{8}He+^{208}Pb at 22 MeV and the calculations considering the global optical potentials for ^{6}Li and ^{7}Li is shown in Fig. 4.4.

As it can be observed, the experimental data is not well reproduced, obtaining values for the reduced chi-square χ^2/N over 250. This fact reveals the differences between ^{8}He and ^{6,7}Li on the scattering from a heavy target, specially at energies above the barrier. In order to better reproduce the data, without varying the geometry of the potential (i.e. radii and diffusenesses), a search has been performed leaving as free parameters the depths of both the real and the imaginary potentials (V and W). The result is shown in Fig. 4.5 and summarized in table 4.2.

Despite χ^2/N drops substantially, mainly due to a good agreement between the experimental data and the calculations for scattering angles greater than 60°, the result can not be considered satisfactory since these potentials generate the Coulomb-nuclear rainbow of the Fresnel type interference pattern, characteristic of light stable

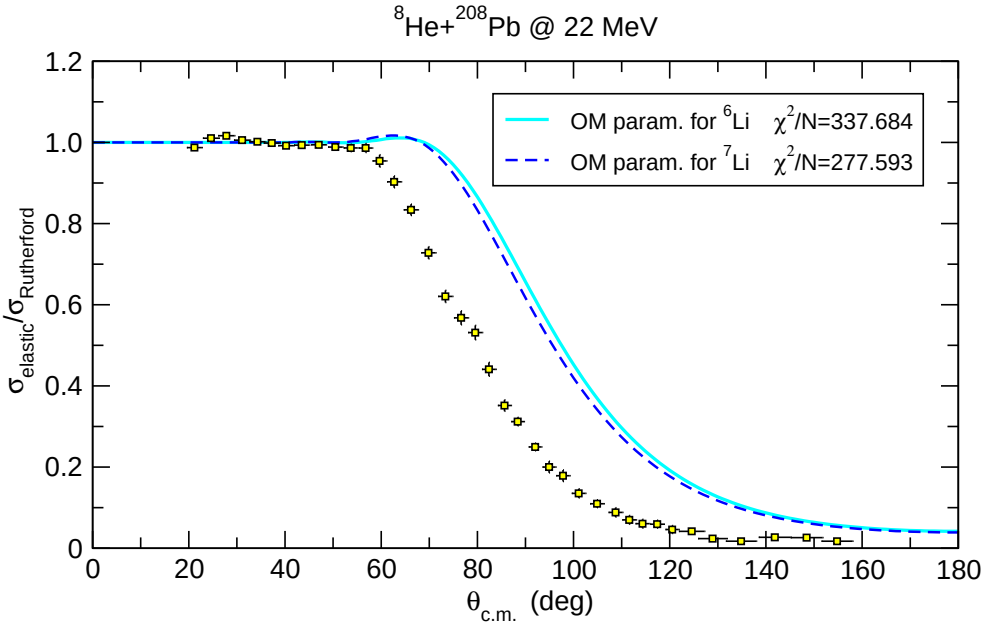

Figure 4.4: *Comparison between the angular distribution of the experimental ratio* $d\sigma_{elastic}/d\sigma_{Rutherford}$ *and the OM calculations considering the global parameters for* ^{6,7}*Li from [90].*

Starting point	V	W	χ^2 /N
^{6}Li global parameters	337.26	118.15	5.24
^{7}Li global parameters	366.58	45.55	6.48

Table 4.2: *Results of the fitting obtained starting from the* ^{6,7}*Li global potential parameters and leaving free the potentials depths* V *and* W *(in MeV).*

nuclei at this energy regime.

With the aim of adjusting the experimental data with a better χ^2, a new search have been performed. In this case, using as starting point the global potential parameters in table 4.1, all six parameters have been left free. The results are shown in Fig. 4.6 and presented in table 4.3. The name given to the sets of parameters in this table, in order to better identify them in following calculations, is also indicated. Larger diffusenesses are needed for the imaginary part, responsible for the absorption of flux from the elastic channel, as it was expected from studies for exotic nuclei with similar characteristics, as ^{6}He in [26].

The values of the diffusenesses obtained for the imaginary part of the nuclear potential suggests the existence of mechanisms responsible for absorption of flux from the elastic channel which act at large distances. The fact that the absorption starts at distances larger than those where the interference between the Coulomb and real nuclear potentials occurs, produces the vanishing of the Coulomb-nuclear rainbow.

Although the imaginary diffusenesses obtained are larger in comparison with those typical for stable nuclei, they are still smaller than the values for halo nuclei as ^{6}He

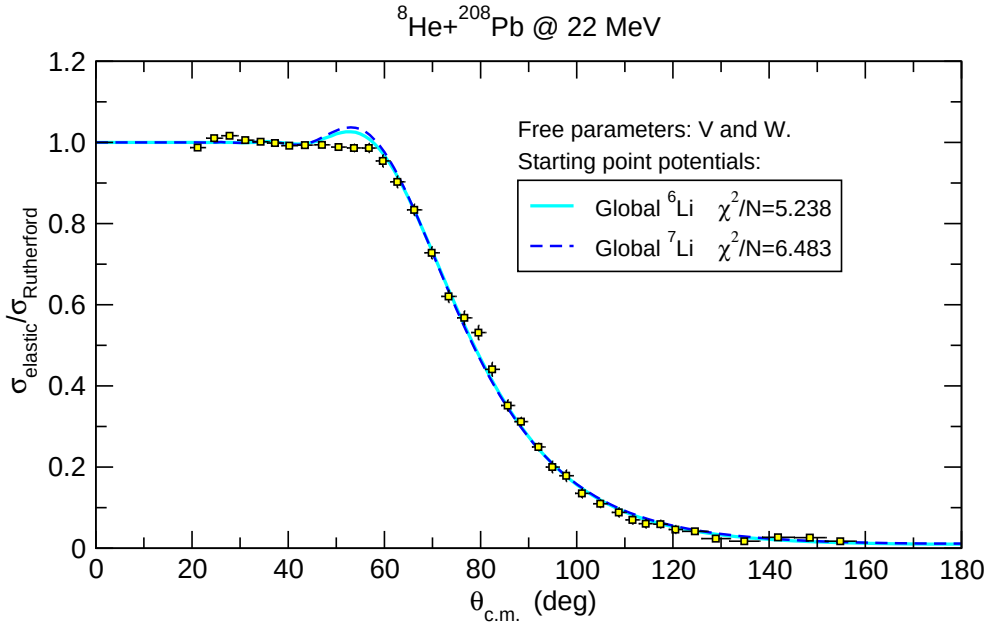

Figure 4.5: *Comparison between the angular distribution of the experimental ratio $d\sigma_{elastic}/d\sigma_{Rutherford}$ and the OM calculations fitting, leaving V and W free. Resulting χ^2/N values are shown.*

Starting point	V	r_R	a_R	W	r_I	a_I	χ^2/N	Set name
^{6}Li global	109.78	1.667	0.577	22.51	1.581	1.144	3.77	Set 1
^{7}Li global	113.46	1.657	0.583	33.51	1.501	1.147	3.77	Set 2

Table 4.3: *Results obtained starting from ^{6,7}Li global optical potentials and searching on all the parameters. Potential depths are expressed in MeV while radii and diffusenesses are expressed in fm.*

[26] where $a_I = 1.89$ fm. As a consequence it is expected that the behaviour of ^{6}He will differ from the Rutherford scattering at larger distances than ^{8}He. A direct comparison between both nuclei is presented in Fig. 4.7 where the experimental ratio $d\sigma_{elastic}/d\sigma_{Rutherford}$ has been plotted versus the distance of closest approach in a classical Coulomb trajectory, r_{max}:

$$r_{max} = \frac{d_o}{2}\left(1 + \frac{1}{\sin(\theta/2)}\right), \tag{4.1}$$

where θ is the scattering angle and $d_o = Z_1 Z_2 e^2/E$ is the distance of closest approach in a head-on collision at a given energy. For ^{6}He (left panel) the data corresponding to the elastic scattering from ^{208}Pb at 16 MeV [26] and 22 MeV [26, 25] have been plotted. A deviation from pure Rutherford scattering becomes evident at distances as large as 20 fm, beyond the typical value of 12 fm used as the strong absorption radius. In the case of ^{8}He (rigth panel), the data at 16 and 22 MeV from this work have been represented, showing that the deviation occurs for a smaller values of r_{max}, around 17 fm.

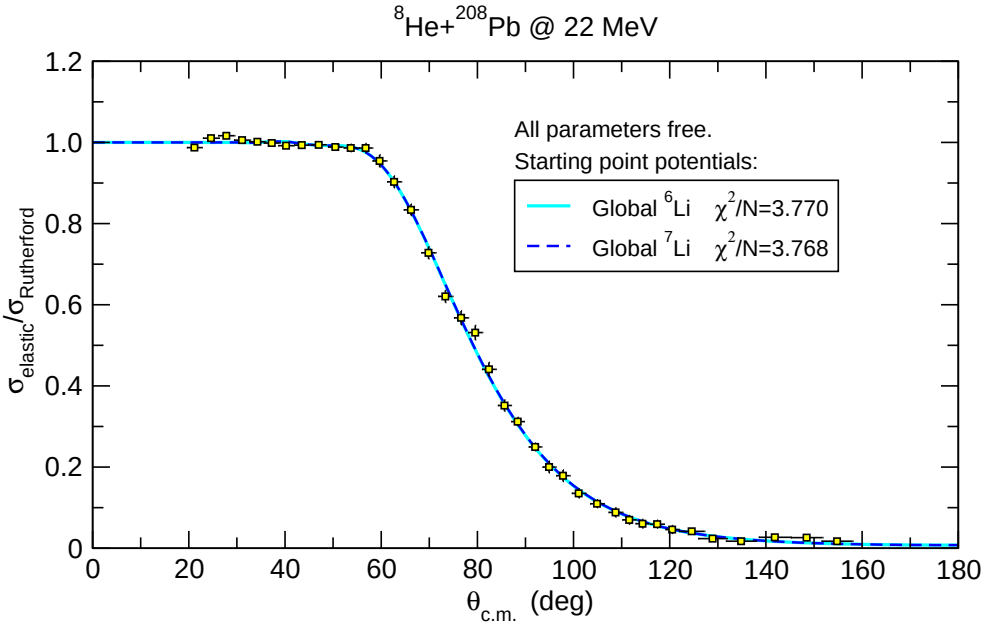

Figure 4.6: *Comparison between the angular distribution of the experimental ratio $d\sigma_{elastic}/d\sigma_{Rutherford}$ and the OM fitting leaving all the six parameters free, i.e. Set 1 and Set 2. Resulting χ^2/N values are shown.*

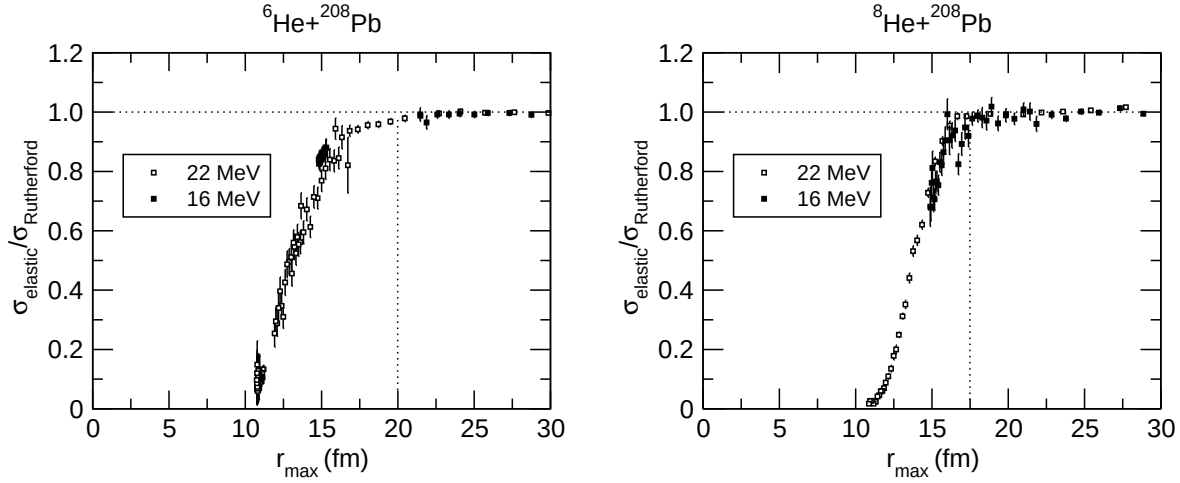

Figure 4.7: *Ratio $d\sigma_{elastic}/d\sigma_{Rutherford}$ versus the distance of closest approach for: (left) the colliding system ^{6}He+^{208}Pb at 16 MeV from [26] and 22 MeV [26, 25] and (right) ^{8}He+^{208}Pb (from this work) at the same energies.*

In [91] it is shown how a systematic trend can be found in the angular distribution of the elastic scattering of ^{6}He at energies around the Coulomb barrier. In particular, the ratio $d\sigma_{elastic}/d\sigma_{Rutherford}$ has been plotted versus the distance of closest approach at five different energies and a common trend has been found suggesting the existence of an "universal function" describing the elastic cross section as a function of r_{max}. This systematic behaviour for ^{6}He, which can be observed in the left panel of Fig. 4.7, also appears for ^{8}He, as shown in the right panel, where a common parametric curve can be found for the two different energies represented.

In addition to the OM calculations presented, a CRC calculation with coupling to the ^{208}Pb(^{8}He,^{7}He)^{209}Pb transfer channel has been performed [92]. The result is shown in Fig. 4.8 with a solid line. For this calculation it has been used a double-folded real potential considering the matter density distribution for ^{8}He from [10] and a Wood-Saxon imaginary part. The starting values of the parameters of the imaginary potential have been obtained from an optical model able to reproduce the elastic data, using a double-folded real potential plus a Wood-Saxon derivative real Dipole Polarization Potential (DPP). However, it has been found that in the CRC calculation the elastic data is properly adjusted with no real DPP and reducing the value of the imaginary depth W. For χ^2/N, a value of 3.5 has been obtained. The "bare" calculation, with no transfer couplings, is presented as a solid line in Fig. 4.8.

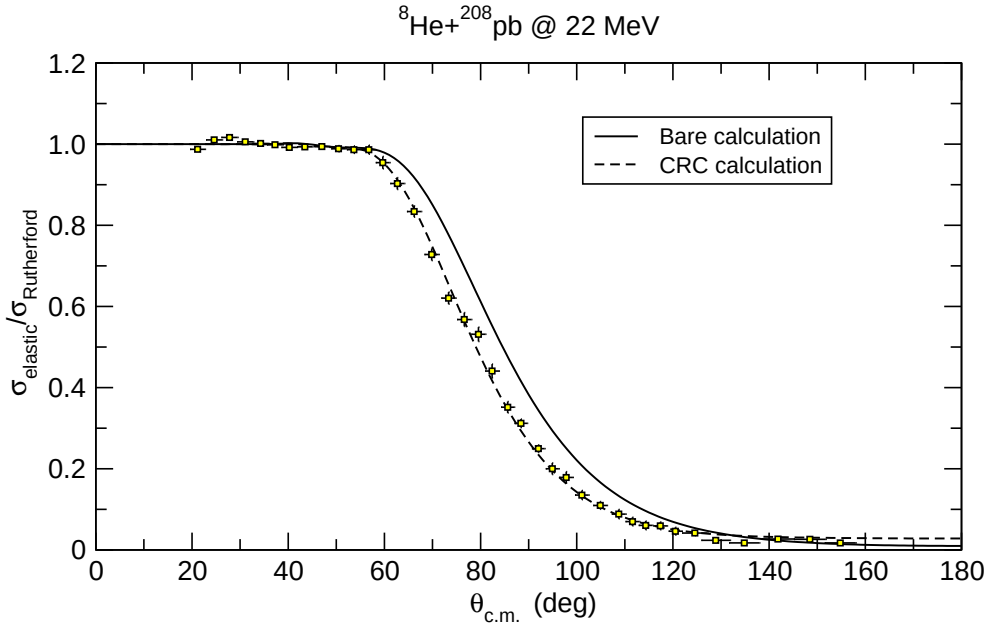

Figure 4.8: *The experimental data for the colliding system ^{8}He+^{208}Pb at 22 MeV is compared to (dashed line) a CRC calculation considering the coupling to the (^{8}He,^{7}He) channel and (solid line) without the coupling.*

It is possible to accurately reproduce the data in the CRC calculation with a real double-folded potential and introducing the coupling to the (^{8}He,^{7}He) transfer channel. Although it is necessary a significant imaginary potential, this transfer mechanism accounts for about 3/8 of the absorption needed in the OM calculation. This suggests that, for the case of ^{8}He, most of the real DPP can be accounted for by the transfer, reducing the importance of the dipole effects. Compared to ^{6}He, the results obtained suggest that the dipole effects in ^{8}He are much smaller. In ^{6}He the dipole coupling is partially responsible of the long range absorption, as shown in [25].

Once the experimental ratio $d\sigma_{elastic}/d\sigma_{Rutherford}$ has been satisfactorily adjusted at 22 MeV (taking as an starting point for the calculations the global optical potential parameters from [90]), the geometry of the optical potential is fixed. Then, a search leaving free the depths of the real and imaginary potentials, V and W respectively, should be carried out in order to properly adjust the experimental data at 16 MeV. However, it has been found that the variation of V does not affect the calculation

significantly and the search only on W is presented. The results, using as starting point the sets of parameters identified as Set 1 and Set 2, are shown in Fig. 4.9 and summarized in table 4.4.

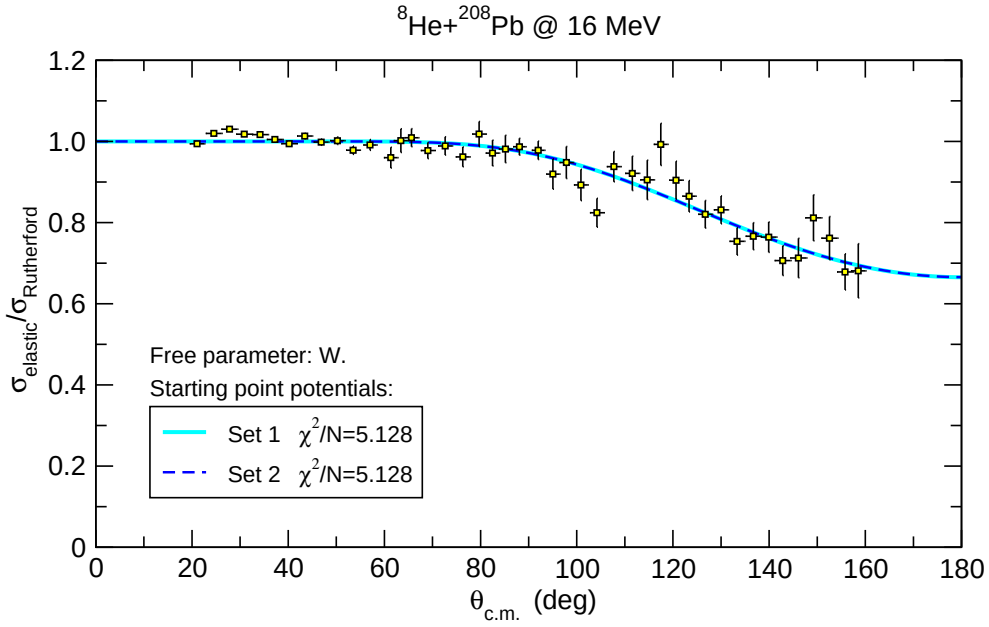

Figure 4.9: *Comparison between the angular distribution of the ratio $d\sigma_{elastic}/d\sigma_{Rutherford}$ and the OM fittings considering the parameters of Set 1 and Set 2 as a starting point and leaving free for the search the depth of the imaginary nuclear potential W. Resulting χ^2/N values are shown.*

Starting point	W	χ^2 /N
Set 1	29.72	5.13
Set 2	44.16	5.13

Table 4.4: *Results obtained starting from Set 1 and Set 2 and leaving free the imaginary potential depths W. Values are expressed in MeV. Resulting χ^2/N values are also shown.*

Unlike the behaviour observed for ^{6}He in [26] which showed a lowering in the depth of the imaginary potential for decreasing energies, in the case of ^{8}He, the values of W found for 16 MeV are larger than those for 22 MeV. This effect has been already observed for nuclei as ^{6}Li in [93] where it was suggested that the increase of W might be due to breakup effects still present at sub-barrier energies. For the case of ^{8}He it could be related as well to the strong breakup mechanisms which hold up well below the barrier, as it is discussed in the next section.

Nevertheless, a second analysis has been performed in which W and the imaginary diffuseness a_I has been left free for the search. Again, Set 1 and Set 2 have been used as starting point. The results are summarized in table 4.5 where it can be observed how, in this case, the imaginary depths decrease but for increasing values of the diffuseness.

Starting point	W	a_I	χ^2 /N
Set 1	19.19	1.233	5.12
Set 2	27.92	1.234	5.12

Table 4.5: *Results obtained starting from the parameters of Set 1 and Set 2 and leaving free the imaginary potential depth W and diffuseness a_I. Resulting χ^2/N values are also shown.*

However, the χ^2/N values obtained do not improve significantly and the general procedure adopted in this study is to fix the geometry of the potentials and search just in the depths. The parameters given in table 4.6 have been considered for the calculations presented in the next sections. The name given to these sets is also indicated.

Starting point	V	r_R	a_R	W	r_I	a_I	χ^2/N	Set Name
Set 1	109.78	1.667	0.577	29.72	1.581	1.144	5.12	Set 3
Set 2	113.46	1.657	0.583	44.16	1.501	1.147	5.12	Set 4

Table 4.6: *Results obtained starting from the parameters of Set 1 and Set 2 and searching only in the imaginary depth. Potential depths are expressed in MeV while radii and diffusenesses are expressed in fm.*

4.3 Interpretation of the ^{6}He/^{8}He ratio

In order to study the experimental ^{6}He yield, two calculations have been carried out in the framework of the Distorted Wave Born Approximation (DWBA). Firstly, one-neutron transfer calculations has been performed, considering just the ground state of ^{7}He since the contribution of the excited state is negligible (as shown in [41, 94]), taking into account that ^{7}He g.s. is not bound and decays to ^{6}He g.s. plus a neutron. Secondly, two-neutron transfer calculations has been performed considering ^{6}He on its g.s and assuming a simplified model in which both neutrons are transferred together as a di-neutron system.

4.3.1 One-neutron transfer calculations

The parameters for the potential describing the entrance channel have been selected among the ones summarized in table 4.3 for 22 MeV (Set 1 and Set 2) and in table 4.6 for 16 MeV (Set 3 and Set 4). The selection of a potential suitable for the exit channel, ^{7}He+^{209}Pb, is more complicated since, being ^{7}He unbound, no data is available for the elastic scattering of this system. For that reason, several known sets of parameters have been used for its description. In particular, the global optical parameters for ^{6}Li

and ^{7}Li projectiles, the parameters for the system ^{6}He+^{208}Pb from [26] and the ones obtained in the previous section for describing the elastic scattering of ^{8}He+^{208}Pb.

An important part of the calculation of the one-neutron transfer is the identification of the states in ^{209}Pb where the neutron coming from ^{8}He could be transferred. Previous studies show that there are only seven single-particle states strongly populated (cross sections between 1 and 10 mb/sr) [95]. In [43], direct reactions and fusion-evaporation reactions were measured for the system ^{8}He+^{208}Pb at 26 MeV. In this study, low spin single-particle states of ^{209}Pb were populated suggesting a major role of 1n-transfer. Thus, for the following calculations, just the low spin states, highlighted in Fig. 4.10, have been considered.

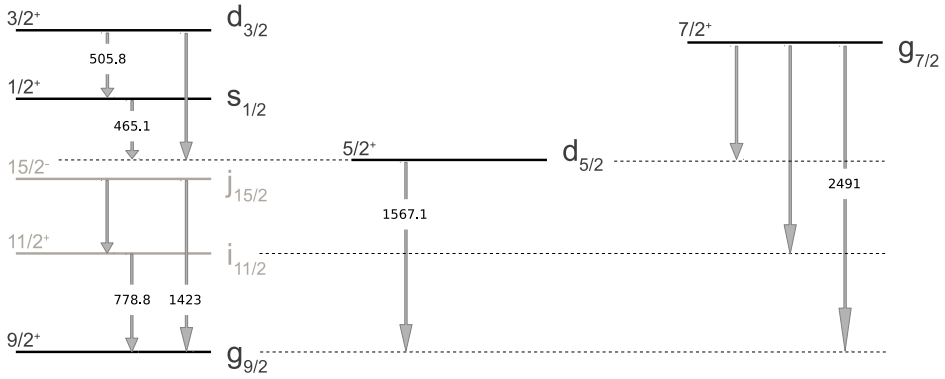

Figure 4.10: *Low spin single-particle states in ^{209}Pb from [95].*

To check this assumption, a calculation considering possible transfers to the high spin states ($1i_{11/2}$ and $1j_{15/2}$) has been carried out in order to evaluate the transfer cross sections to all the states observed in [95]. The results are shown in Fig. 4.11, demonstrating that the transfer occurs mainly to the low spin states considered in [43].

The binding potentials and spectroscopic factors are a fundamental input for this type of calculations. The particular values for the $\langle^{8}\mathrm{He}|^{7}\mathrm{He}+n\rangle$ and $\langle^{209}\mathrm{Pb}|^{208}\mathrm{Pb}+n\rangle$ overlaps have been taken from [41] and [95], respectively. The spectroscopic amplitudes (square root of the spectroscopic factors), summarized in table 4.7, have been used.

For 22 MeV, the different options for optical potentials describing the entrance and exit channel partitions have been tested and a total of ten calculations for one-neutron transfer have been carried out. The results are plotted in Fig. 4.12 where it can be seen that the curves do not converge, being strongly dependent on the model chosen for the system ^{7}He+^{209}Pb. Therefore, only a band of possible results has been provided, which is shown in Fig. 4.13.

The production of ^{6}He by means of other reactions should be also considered, in particular two-neutron transfer leading to ^{6}He on the ground state and the breakup channel, and therefore, the band in Fig. 4.13 should be regarded just as a lower limit for the production of ^{6}He. However, one can notice that the angular distribution of ^{7}He shown in this figure does not depend critically on model assumptions between 30° and 90° lab.

To compare the calculations with the experimental ^{6}He/^{8}He ratio, the calculated transfer cross sections should be divided by the absolute elastic cross section. In

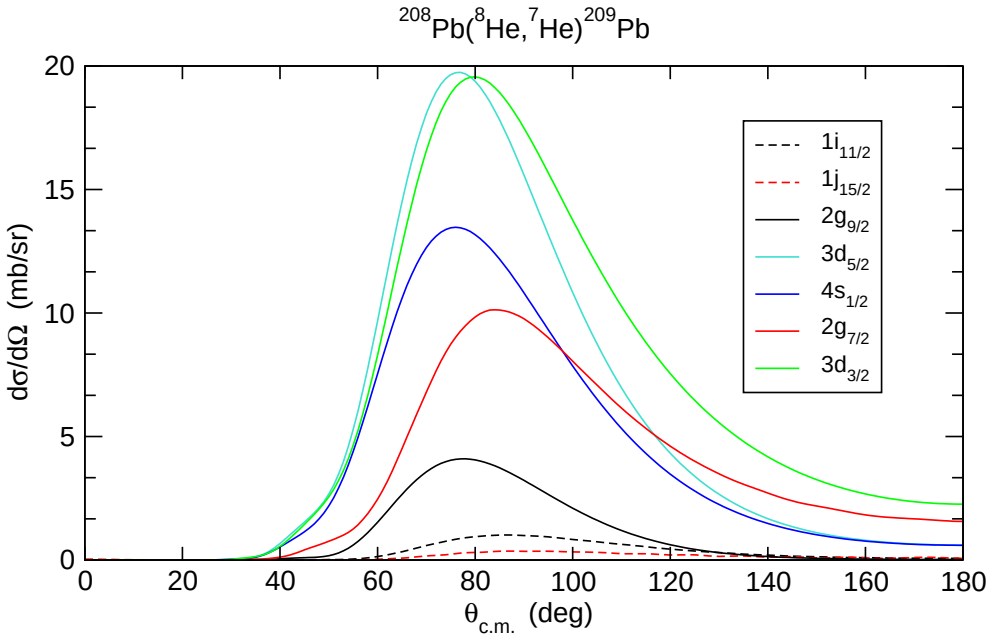

Figure 4.11: *Comparison between the differential cross sections for one-neutron transfer to different single-particle states in ^{209}Pb. The transfer will populate, essentially, the low spin levels.*

nlj	Spectroscopic amplitudes for $\langle^8\mathrm{He}\vert^7\mathrm{He}+n\rangle$
$1p_{3/2}$	1.7
nlj	Spectroscopic amplitudes for $\langle^{209}\mathrm{Pb}\vert^{208}\mathrm{Pb}+n\rangle$
$2g_{9/2}$	0.96
$1i_{11/2}$	1.07
$1j_{15/2}$	0.88
$3d_{5/2}$	0.94
$4s_{1/2}$	0.92
$2g_{7/2}$	0.97
$3d_{3/2}$	0.99

Table 4.7: *Spectroscopic amplitudes for $\langle^8\mathrm{He}\vert^7\mathrm{He}+n\rangle$ from [41] and for the ^{209}Pb single-particle states from [95].*

this point, the elastic cross sections calculated in section 4.2, which reproduce the experimental data, are used. The result is presented in Fig. 4.14 together with the experimental data. For angles in the range between 30° and 60° it is expected a contribution of the breakup channel but, at backward angles, only transfer mechanisms will be present and, for this reason, these one-neutron transfer calculations represent a lower limit for the experimental ratio and the two-neutron transfer contribution is needed to reproduce the data.

In the case of 16 MeV, the calculations for one-neutron transfer have been per-

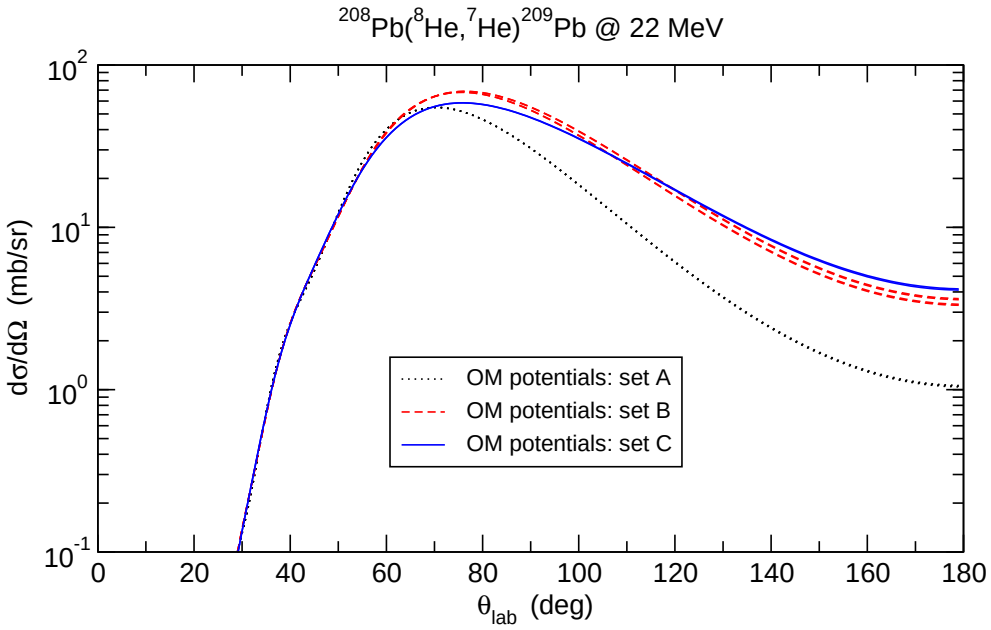

Figure 4.12: *Angular distribution of the one-transfer cross sections obtained for different combinations of optical potentials suitable for the entrance and exit channels. All the curves have been generated using, for the entrance partition, the two possible set of parameters describing the ^{8}He+^{208}Pb colliding system at 22 MeV (Set 1 and Set 2). 4.3. In set A, these same parameters have been used for the exit channel, while in set B the global optical-model potentials for $^{6,7}Li$ have been considered and in set C the parameters for ^{6}He+^{208}Pb at 22 MeV from [26].*

formed considering the following combinations of potentials: the parameters from Set 3 and Set 4 for the entrance partition and the same parameters, the ^{6,7}Li global parameters and ^{6}He ones (for 16 MeV from [26]) for the exit partition. Again, these combinations give rise to ten calculations which allow for providing the band within the one-neutron transfer cross section is expected to be found. The result is shown in Fig. 4.15.

These calculations have been compared to the experimental ^{6}He/^{8}He ratio, after properly dividing the transfer cross sections by the absolute elastic cross section, and the result is shown in Fig. 4.16. As for 22 MeV, still at 16 MeV, the two-neutron contribution is need in order to reproduce the data.

4.3.2 Two-neutron transfer calculations

As it has been mentioned before, for the two-neutron transfer calculations, a simplified model considering that both neutrons are transferred together as a di-neutron system has been used.

In order to reproduce the ^{6}He/^{8}He ratio, only the transfer producing ^{6}He in the ground state has been considered. If ^{6}He is left in an excited state, it will decay to ^{4}He and two neutrons contributing to the ^{4}He yield. This second process will be addressed afterwards.

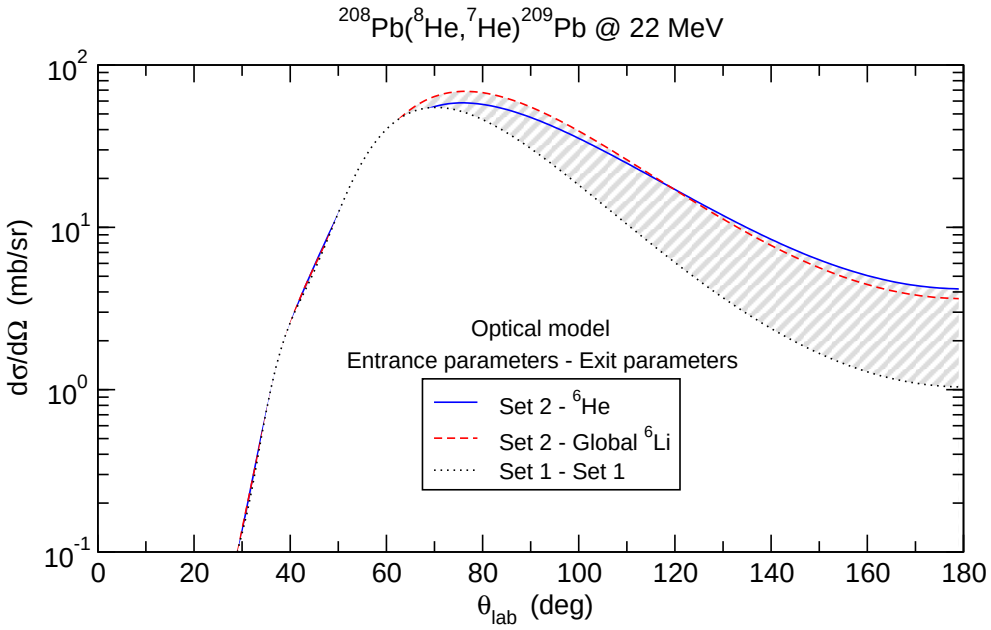

Figure 4.13: *Calculations for one-neutron transfer which provide a band depending on the model used. For the dotted line, the parameters in Set 1 have been used for describing both the entrance and exit partitions. The dashed line considers the parameters in Set 2 in the entrance channel and, for the exit channel, the global parameters for ^{6}Li from [90] and, finally, in the solid line the parameters in Set 2 the ^{6}He ones from [26] at 22 MeV have been considered for the entrance and exit partitions respectively.*

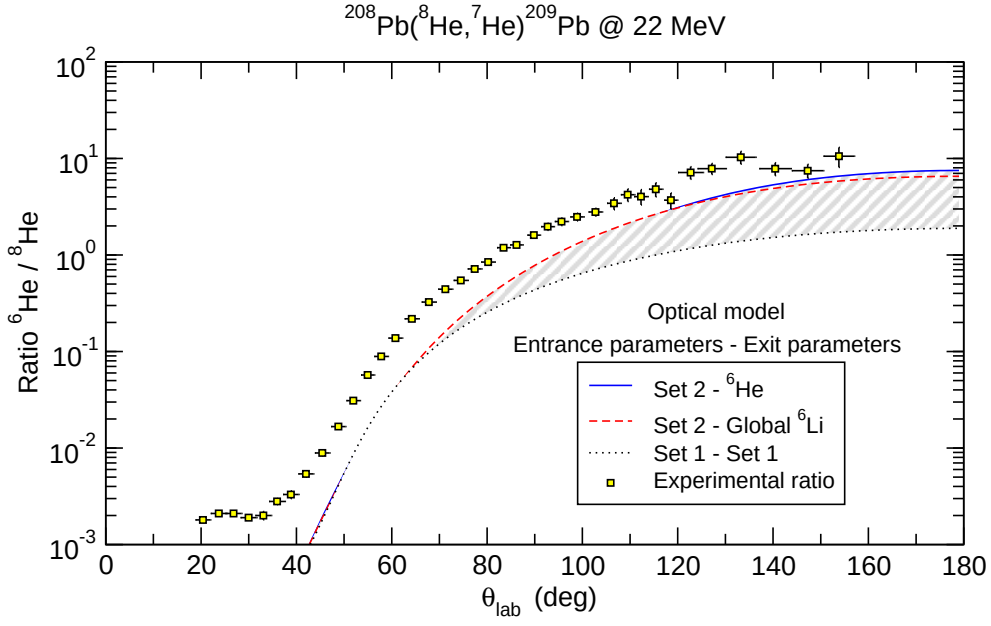

Figure 4.14: *Comparison between the experimental ^{6}He/^{8}He ratio at 22 MeV and the calculations for one-neutron transfer. The parameters describing the entrance and exit channels are the same as for Fig. 4.13.*

In order to perform the calculation, an optical potential suitable for describing the elastic scattering of ^{8}He+^{208}Pb is necessary for the entrance channel. However, in

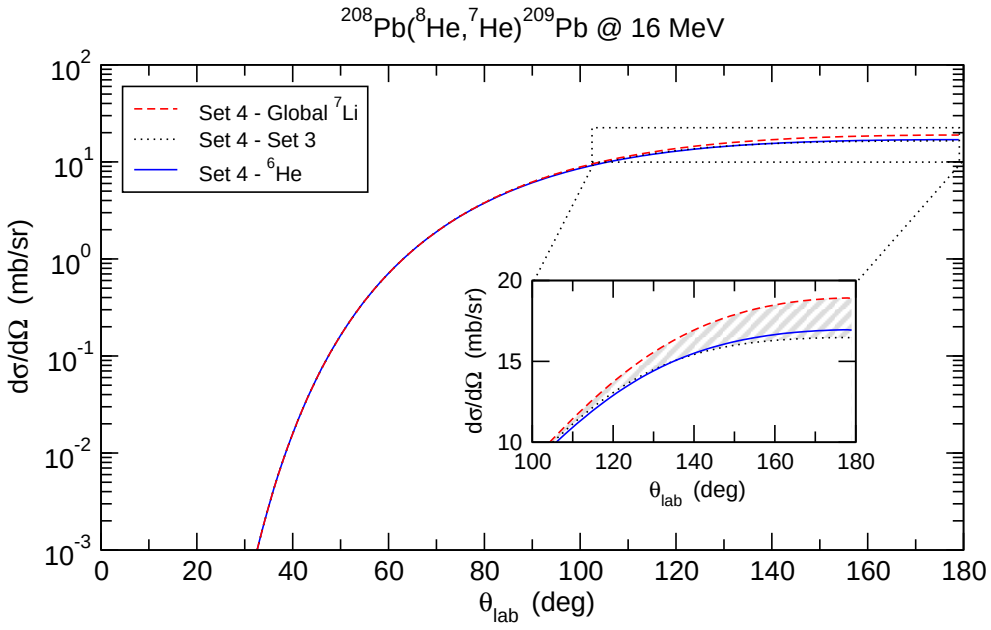

Figure 4.15: *Calculations for one-neutron transfer which provide a band depending on the model used. In all cases, the entrance partition is described by the parameters for Set 4. For the exit partition, the dotted line considers the parameters for Set 3, while the dashed and solid lines consider the global potential parameters for ^{7}Li and the ^{6}He ones respectively. The inset shows the different curves in the angular range betweeen 100° and 180°.*

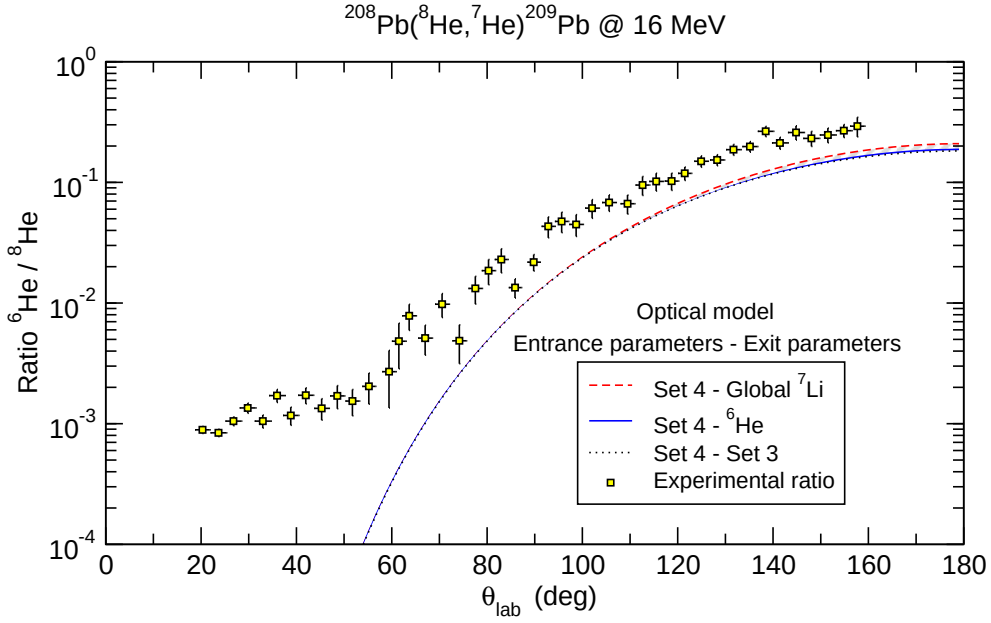

Figure 4.16: *Comparison between the experimental $^{6}He/^{8}He$ ratio at 16 MeV and the calculations for one-neutron transfer. The parameters describing the entrance and exit channels are the same as for Fig. 4.15.*

this case, selecting an optical potential for the exit channel is more straightforward as ^{6}He+^{208}Pb is a well known system. It can be considered that the behaviour of

^{6}He+^{210}Pb should be very similar. The parameters for the exit channel potential are those for ^{6}He+^{208}Pb already presented in the last section.

On the other hand, the state in ^{210}Pb where the dineutron is transferred should be determined. Following the Brink matching conditions [96], it is found that, for the transfer of uncharged particles, the maximum cross section for a given spin-parity and spectroscopic factors occurs for an effective Q-value (Q_{ef}) close to zero or even slightly negative ([25, 35]), i.e., the particle is transferred to excited states in the final nucleus with an energy around the Q-value (Q), as Q_{ef} is defined as Q minus the excitation energy of the state. Since Q for the reaction ^{208}Pb(^{8}He,^{6}He)^{210}Pb is 6.983 MeV, it has been considered that the transfer proceeds to a state in ^{210}Pb with this excitation energy.

^{6}He can be produced by one and two-neutron transfer and breakup. Assuming that for large scattering angles ^{6}He comes from transfer processes, the already calculated one-neutron transfer cross section has been summed up with the two-neutron transfer cross section, normalized by a constant, in order to reproduce the experimental data, following [25, 35]. In particular, this method has been carried out for the limiting curves of the band of possible values for the one-neutron transfer. The results obtained for 22 MeV are shown in Fig. 4.17. The values of the normalization constant vary between 18 and 26, depending on the set of potentials chosen for representing the entrance and exit channels. For the sake of comparison, a value of 6.1 was obtained in [35] for two-neutron transfer calculations in the system ^{6}He+^{206}Pb.

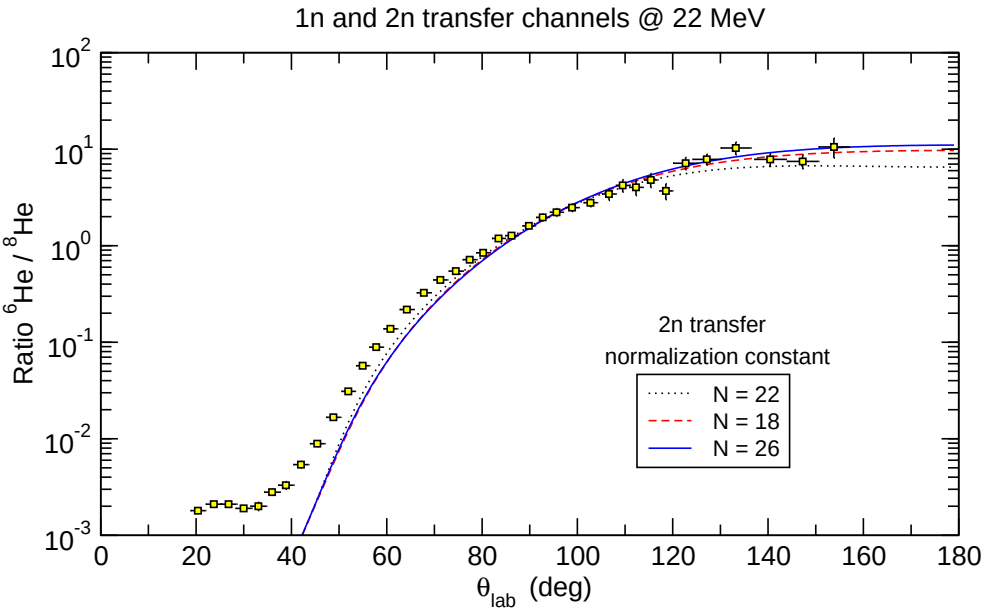

Figure 4.17: *Comparison between the experimental ^{6}He/^{8}He ratio at 22 MeV and the curves obtained adding the contributions of the one-neutron transfer for the three curves shown in Fig. 4.13 and the two-neutron transfer, normalized by a suitable constant in order to reproduce the data.*

As it can be observed in Fig. 4.17, the experimental data can be reproduced for angles larger than 75° just by means of transfer mechanisms. The contribution of the breakup process gets more importance as the scattering angle decreases, becoming the

dominant mechanism at very forward angles.

For 16 MeV, the results obtained for the sum of the one and two-neutron transfer cross sections are shown in Fig. 4.18. In this case, transfer mechanisms can reproduce the experimental data by themselves just at backward angles, larger than 100°, while for smaller angles, above 90°, other contributions as breakup should be considered in order to explain the data.

As expected, transfer processes are less probable as the energy decreases, since the colliding nuclei should be close enough for these mechanisms to act. However, the yield of ^{6}He is still large at sub-barrier energies, which indicates an important role of breakup.

From the direct observation of the experimental ^{6}He/^{8}He ratio at 22 MeV in Fig. 4.14, a change in the trend is produced at about 35° as a consequence of the transfer mechanisms. This angle corresponds to a distance of closest approach of around 23 fm, which can be understood as the value of r_{max} from which the transfer processes begin to be relevant. This distance implies, for 16 MeV, that these mechanisms should become evident at about 55°. This is consistent with the angle in which a change in the trend of the ^{6}He/^{8}He ratio at 16 MeV (Fig. 4.16) is produced due to transfer.

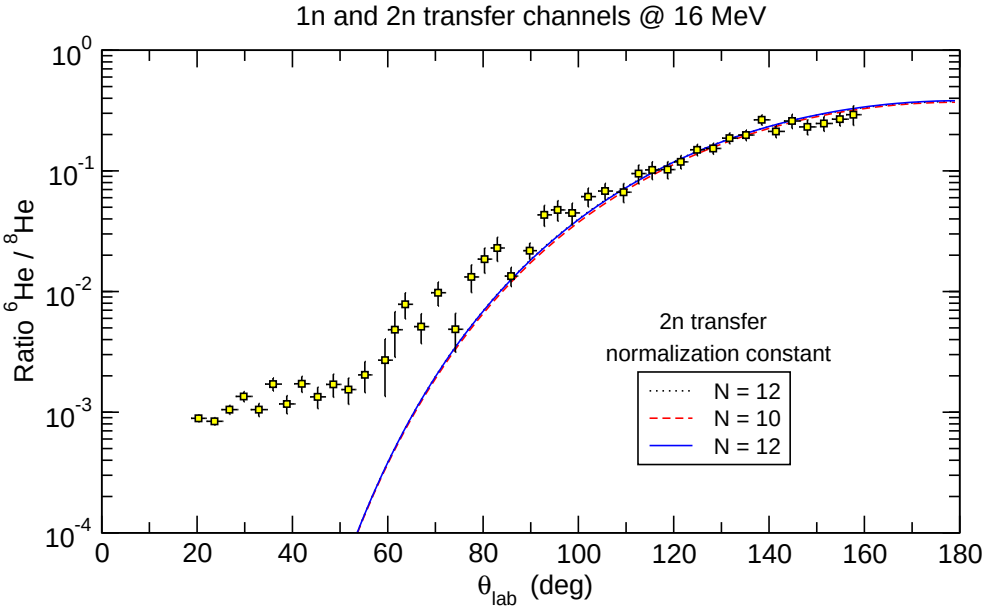

Figure 4.18: *Comparison between the experimental ^{6}He/^{8}He ratio at 16 MeV and the curves obtained adding the contributions of the one-neutron transfer for the three curves shown in Fig. 4.15 and the two-neutron transfer, normalized by a suitable constant in order to reproduce the data.*

4.4 Interpretation of the ^{4}He/^{8}He ratio

As it has been mentioned before, the transfer mechanism of two neutrons leading to ^{6}He in an excited state has not been taken into account so far, as it decays into ^{4}He and

two neutrons contributing to the ^{4}He yield. In this section, this process is studied by using DWBA calculations. The optical potential chosen for describing the exit channel is the one used for ^{6}He+^{208}Pb [26]. For the entrance channel, any of the potentials suitable for the ^{8}He+^{208}Pb colliding system at 16 and 22 MeV may be chosen.

The results of the DWBA calculations for 22 MeV are shown in Fig. 4.19. The ^{4}He/^{8}He ratio obtained is presented together with the experimental data in Fig. 4.20.

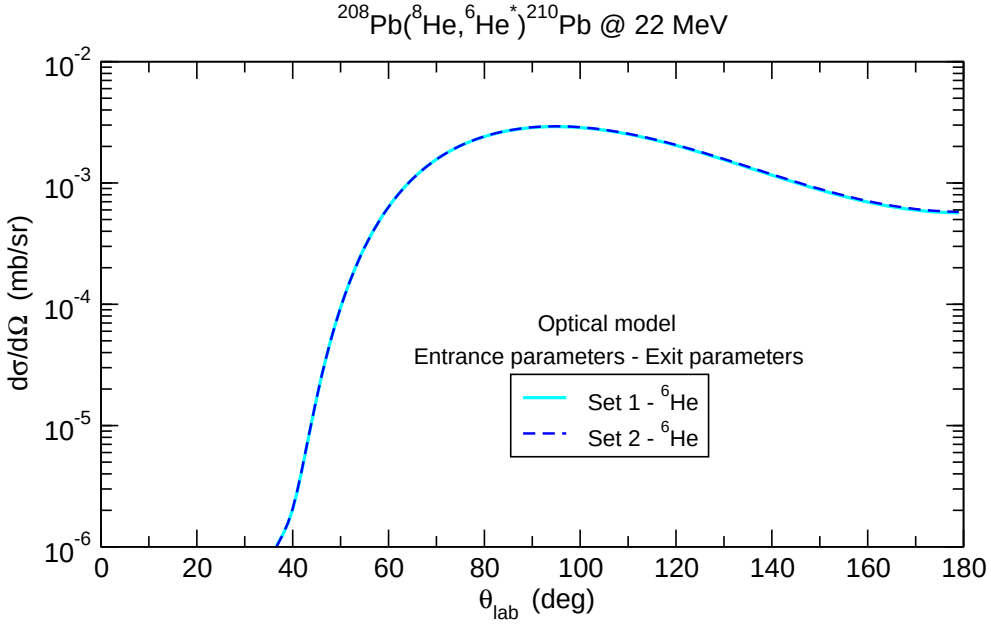

Figure 4.19: *Two-neutron transfer calculations, considering the coupling to ^{6}He*. The parameters for the exit channel are those describing the scattering of ^{6}He on ^{208}Pb at 22 MeV, while for the entrance channel, the parameters of Set 1 and Set 2 have been used.*

It is found that the DWBA calculations underestimate the data by a factor of around 10.000. In order to see whether the shape of the experimental data can be described by means of transfer mechanisms or not, these curves have been multiplied by a numerical factor. The result is shown in Fig. 4.21.

Using this procedure, the shape of the experimental distribution can be reproduced in the angular range from 75° (not at forward angles), suggesting that the production of ^{4}He at backward angles is due to transfer, as the cross sections for all the possible transfer processes have a similar bell-shape for the ^{4}He/^{8}He ratio. The rest of ^{4}He, at angles smaller than 75°, may be due to breakup processes.

For 16 MeV, the comparison between the experimental ^{4}He/^{8}He ratio and the DWBA calculations is shown in Fig. 4.22. Again, the experimental data can not be properly reproduced. The same procedure as for 22 MeV is followed. The curves in 4.22 are multiplied by a factor of around 10.000, with the aim of reproducing part of the shape of the angular distribution of ^{4}He/^{8}He. The result is shown in Fig. 4.23. As in the case of ^{6}He, the ^{4}He yield at 16 MeV can be explained, to a large extent, by means of breakup, as transfer processes are less relevant at this energy.

Following the same reasoning as for the ratio ^{6}He/^{8}He, in the experimental ratio

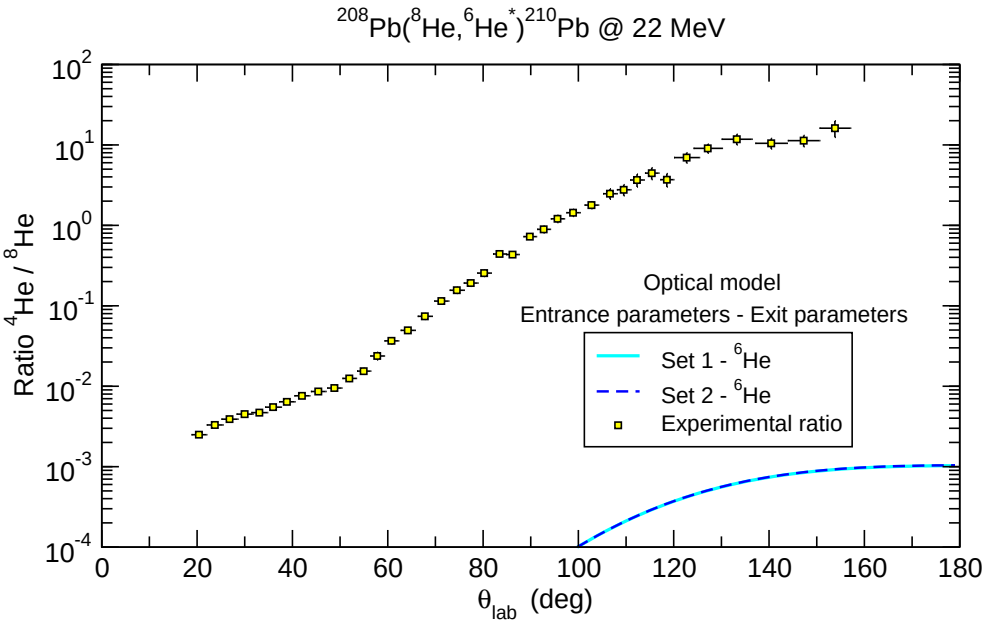

Figure 4.20: *Comparison between the experimental $^4He/^8He$ ratio at 22 MeV and the calculations for two-neutron transfer.*

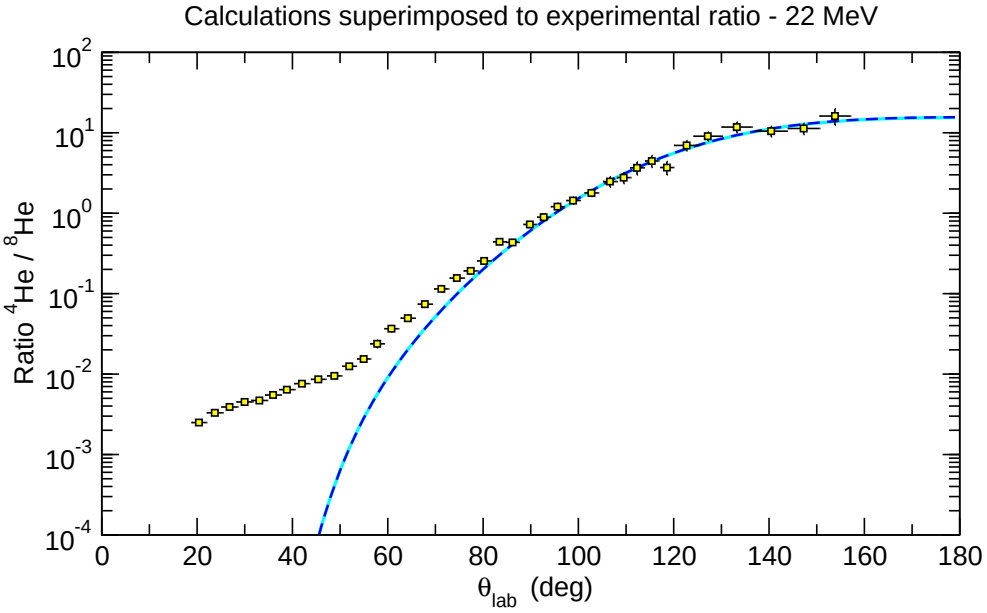

Figure 4.21: *Comparison between the experimental $^4He/^8He$ ratio at 22 MeV and the calculations for two-neutron transfer multiplied by a numerical factor in order to reproduce the shape of the experimental distribution.*

^{4}He/^{8}He, a change in the trend is produced at about 50° (see Fig. 4.20). The corresponding distance of closest approach implies, for 16 MeV, that transfer mechanisms should become relevant at about 85°, which is also in agreement with the experimental ratio at this energy (see Fig. 4.22.)

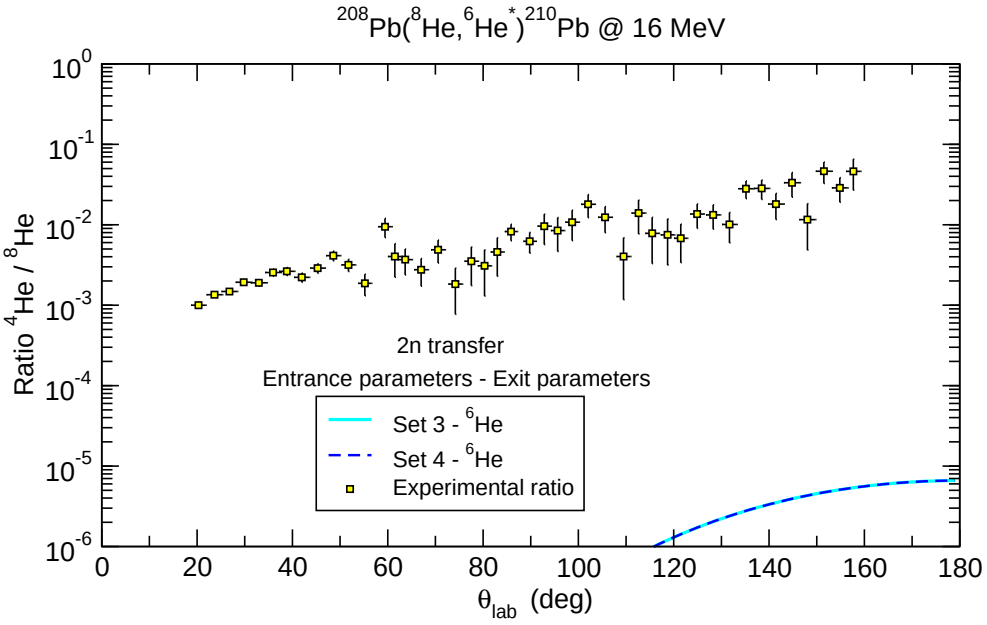

Figure 4.22: *Comparison between the experimental ^{4}He/^{8}He ratio at 16 MeV and the calculations for two-neutron transfer.*

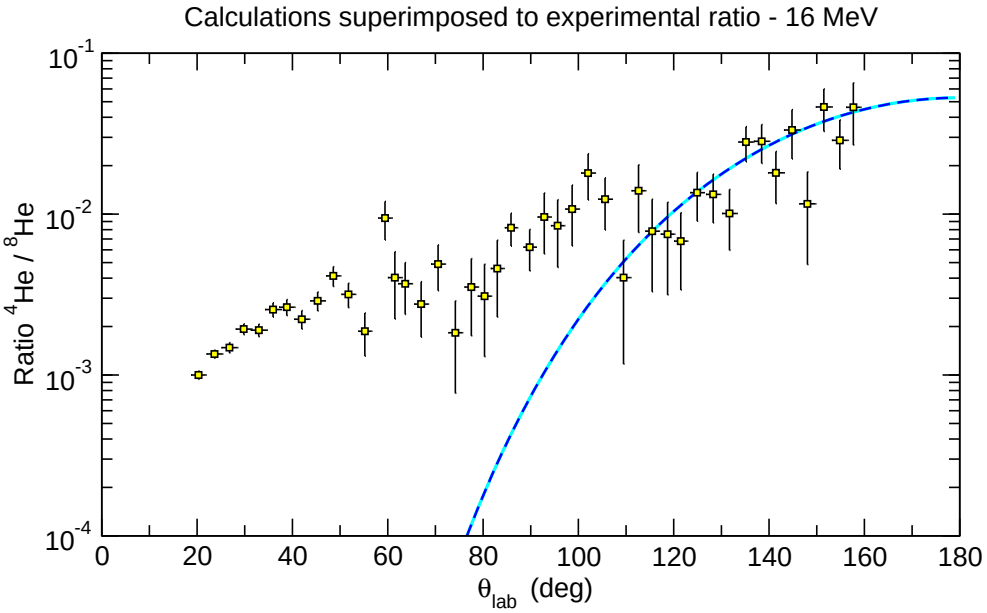

Figure 4.23: *Comparison between the experimental ^{4}He/^{8}He ratio at 16 MeV and the calculations for two-neutron transfer multiplied by a numerical factor in order to reproduce the shape of the experimental distribution.*

5 Summary and conclusions

In this chapter, a brief outline of the present dissertation is presented, together with the main conclusions that can be extracted from the analysis of the experimental data.

The objective of this thesis is the study of the elastic scattering of ^{8}He from ^{208}Pb at energies around the Coulomb barrier. The heavy nucleus ^{208}Pb is an ideal target, doubly magic, which provides a strong Coulomb field for the scattering process. This work is an extension of the investigations performed by the collaboration, in which the Grupo de Estructura de la Materia of the University of Huelva takes part, on ^{11}Li, ^{11}Be and, particularly, ^{6}He reactions at near-barrier energies. The direct comparison of the experimental data from the ^{6}He+^{208}Pb and ^{8}He+^{208}Pb experiments will allow for studying the subtle differences in the dynamics of halo and skin nuclei.

To achieve this objective, the experiment E587S has been performed at GANIL (Caen, France) in 2010. The angular distributions of the elastic channel, and the ^{6}He and ^{4}He yields from the reactions induced by ^{8}He on the ^{208}Pb target have been measured at two different energies, 16 and 22 MeV.

A new compact silicon detector array named GLORIA has been developed, as part of this work, in order to study heavy ion reactions involving radioactive beams. This detection system consists of six particle telescopes arranged in a very close geometry around a 30° rotated-target system, allowing for the measurement of reaction fragments in a continuous angular range from 15° to 165° (Lab). GLORIA has been used for the first time during the experiment E587S and has provided continuous angular distributions of elastic and reaction cross sections in a wide angular range.

Bi-dimensional calibrated spectra have been obtained from the data files acquired during the experiment, and analysed by means of PAW++ [85] and ROOT [86]. As no stable pilot beam was available in order to normalise the experimental data, a strong effort has been made in order to properly assign not only the scattering angles but the solid angle of each pixel in the setup. For this reason, Monte Carlo simulations have been performed with the code NPTool [72] determining, at each energy, the effective position of the beam spot on target and the detectors array, as the characteristics of the beam may differ.

The interpretation of the elastic scattering angular distributions have been per-

formed by means of the Optical Model and Coupled Reaction Channels calculations.

Firstly, the elastic scattering at 22 MeV have been studied. A first comparison with previous phenomenological potentials, in particular those for ^{6}Li and ^{7}Li from [90], have been carried out, revealing the differences between ^{8}He and ^{6,7}Li on the scattering from a heavy target at near-barrier energies. The main difference arises from the fact that the potentials for ^{6,7}Li generate the so-called "Coulomb-nuclear rainbow", characteristic of light stable nuclei. This effect is absent in the ^{8}He experimental data.

In order to better reproduce the experimental data, the parameters defining the optical potentials have been modified. As a result, it has been observed that larger values are needed for the diffuseness of the imaginary part, which is responsible for the absorption of flux from the elastic channel. This effect has been already observed in the case of ^{6}He [25, 26]. This suggests the existence of long range mechanisms, in such a way that the absorption starts at distances larger than those where the interference between Coulomb and nuclear potentials occurs, producing the vanishing of the Coulomb-nuclear rainbow.

The value of the imaginary diffuseness ($\sim$1.14 fm) is large in comparison with the typical value for a stable nucleus ($\sim$0.7 fm) but still smaller than those for halo nuclei as ^{6}He ($\sim$1.89 fm). As a consequence it is expected that the behaviour of ^{6}He will differ from pure Rutherford scattering at larger distances than ^{8}He. In the representation of the experimental ratio $d\sigma_{elastic}/d\sigma_{Rutherford}$ versus the distance of closest approach in coulombian trajectories this effect can be observed. While for ^{6}He the deviation from Rutherford is evident at very large distances ($\sim$20 fm), in the case of ^{8}He, it occurs roughly at $\sim$17 fm.

This representation is also interesting since, for ^{6}He, it has been found a systematic trend in the angular distribution of the elastic cross section at different energies around the Coulomb barrier, suggesting an universal function describing this mechanism as a function of the distance of closes approach [91]. This systematic behaviour has been also found in the case of ^{8}He.

A CRC calculation taking into consideration the coupling to the ^{208}Pb(^{8}He,^{7}He)^{209}Pb transfer channel have been also presented for the elastic scattering. It has been found that in this calculation the elastic data can be properly reproduced with no real Dipole Polarization Potential (DPP). Compared to ^{6}He, the results suggest that the dipole effects, which were important and partially responsible of the long range absorption in this halo nuclei, are much smaller for ^{8}He.

For fitting the elastic data at 16 MeV, the depths of the optical potentials obtained at 22 MeV have been modified. It has been found that the variation of the depth of the real part (V) does not affect the OM fit. However, the depth of the imaginary part (W) increases. The opposite behaviour was found for ^{6}He [26] in which W followed a decreasing trend for decreasing energies. However, the same effect as for ^{8}He was already observed for ^{6}Li [93] suggesting that the breakup effects were still present at sub-barrier energies. For ^{8}He it could be also due to strong breakup mechanisms which hold up well below the barrier.

For the interpretation of the experimental ^{6}He/^{8}He ratio two calculations have been performed in the framework of the Distorted Wave Bron Approximation (DWBA): one-

neutron and two-neutron transfer calculations. For the latter, a simplified model has been considered in which both neutrons are transferred together as a di-neutron. The two-neutron transfer calculations, properly normalised, have been summed up with the one-neutron transfer ones.

For 22 MeV, the one-neutron and two-neutron transfer calculations can reproduce the experimental ratio ^{6}He/^{8}He at angles larger than 75°. For smaller angles, these contributions are not enough for explaining the data so the breakup process starts to be relevant, becoming dominant at very forward angles. For 16 MeV, the calculations for the transfer mechanisms are enough to reproduce the experimental data for larger angles, from 100°. As expected, transfer mechanisms are less probable as the energy decreases since the colliding nuclei should be close enough. Moreover, for the sub-barrier energy, the ^{6}He yield is still large indicating an important role of breakup.

The angular distributions of the ^{6}He/^{8}He ratio at both 16 and 22 MeV show a change in the trend as a consequence of the onset of the transfer mechanisms. The angle corresponding to this change of trend, besides being different at each energy, corresponds to the same value for the distance of closest approach, ∼23 fm, which can be understood as the distance from which the transfer processes begin to be relevant, regardless the collision energy.

For the interpretation of the experimental ^{4}He/^{8}He ratio the two-neutron transfer leading to ^{6}He in an excited state has been considered and studied by means of DWBA calculations. It has been found that, at both energies, the calculations underestimate the data by a factor of around 10.000. However, multiplying by this factor, the shape of the experimental distributions can be reproduced. For 22 MeV, it is found that from 75°, the production of ^{4}He can be explained by means of transfer while for smaller angles the breakup processes are relevant. In the case of 16 MeV, the ^{4}He yield can be explained, to a large extent, by means of breakup, as transfer is less relevant at this energy. In fact, the change in the trend of the distribution at 22 MeV implies, for 16 MeV, that transfer mechanisms should become relevant for angles larger than 85°.

In general, a preliminary interpretation of the experimental data through simple models have been presented. Further studies will be performed in the near future, including CDCC and more refined CRC calculations.

6 Resumen y conclusiones

En este último capítulo se presenta un breve resumen de la tesis junto con las principales conclusiones que pueden extraerse del análisis de los datos experimentales.

El objetivo de la tesis es el estudio de la dispersión elástica de ^{8}He en ^{208}Pb a energías en torno a la barrera de Coulomb. El núcleo pesado ^{208}Pb es un blanco ideal, doblemente mágico, que proporciona un fuerte campo coulombiano para el proceso de dispersión. Este trabajo es una extensión de las investigaciones realizadas por la colaboración en la que participa el Grupo de Estructura de la Materia de la Universidad de Huelva, acerca de reacciones inducidas por ^{11}Li, ^{11}Be y, particularmente, ^{6}He a energías cercanas a la barrera. La comparación directa de los datos experimentales para los sistemas ^{6}He+^{208}Pb y ^{8}He+^{208}Pb permitirá el estudio de las diferencias en la dinámica de los llamados núcleos "halo" y "skin".

Para lograr este objetivo, se llevó a cabo el experimento E587S en GANIL (Caen, Francia) en 2010. Las distribuciones angulares del canal elástico y de la producción de ^{6}He y ^{4}He, procedentes de las reacciones inducidas por el ^{8}He en el blanco de ^{208}Pb, han sido medidas a dos energías diferentes, 16 y 22 MeV.

Un nuevo sistema de detectores de silicio compacto, denominado GLORIA, ha sido desarrollado como parte de este trabajo con el objetivo de estudiar reacciones con haces radioactivos. El sistema de detección consiste de seis telescopios de partículas situados en una geometría muy compacta alrededor de un blanco girado 30°, permitiendo medir los fragmentos de reacción en un rango angular continuo entre 15° y 165° (Lab). GLORIA ha sido empleado por primera vez durante el experimento E587S permitiendo obtener distribuciones angulares continuas para la sección eficaz elástica y las secciones eficaces de reacción en un rango angular amplio.

A partir de los ficheros de datos obtenidos durante el experimento se han obtenido espectro bidimensionales calibrados, los cuales han sido analizados a través de PAW++ [85] y ROOT [86]. Ya que no hubo haz piloto disponible para normalizar los datos experimentales, se ha realizado un importante esfuerzo con el objeto de asignar adecuadamente tanto los ángulos de dispersión como los ángulos sólidos para cada pixel del sistema de detección. Por este motivo se han llevado a cabo simulaciones de Monte Carlo gracias al código NPTool [72] determinando, a cada energía, la posición efectiva

del haz en el blanco y del sistema de detectores, teniendo en cuenta que las características del haz pueden variar.

La interpretación de las distribuciones angulares para la dispersión elástica se ha realizado mediante el Modelo Óptico y cálculos CRC (del inglés Coupled Reaction Channels).

En primer lugar se ha estudiado la dispersión elástica a 22 MeV. Se ha llevado a cabo una primera comparación con potenciales fenomenológicos previos, en particular los de ^{6}Li y ^{7}Li de [90], revelando las diferencias entre ^{8}He y ^{6,7}Li en la dispersión con blancos pesados a energías en torno a la barrera. La principal diferencia surge del hecho de que los potenciales para ^{6,7}Li generan el llamado "arcoiris Coulombiano-nuclear", característico de núcleos ligeros estables. Este efecto no se encuentra presente en los datos experimentales para ^{8}He.

Con el objetivo de reproducir más adecuadamente los datos experimentales, los parámetros que definen los potenciales ópticos han sido modificados. Como resultado se ha observado que se requieren valores mayores para la difusividad de la parte imaginaria, que es la responsable de la absorción de flujo del canal elástico. Este efecto ya ha sido observado en el caso de ^{6}He [25, 26]. Esto sugiere la existencia de mecanismos de reacción de largo alcance de manera que la absorción comienza a distancias mayores de aquellas en las que la interferencia entre los potenciales nuclear y Coulombiano tiene lugar. Como consecuencia desaparece el arcoiris Coulombiano-nuclear.

El valor de la difusividad imaginaria ($\sim$1.14 fm) es grande en comparación con los valores típicos para los núcleos estables ($\sim$0.7 fm) si bien inferior a los valores para núcleos halo como el ^{6}He ($\sim$1.89 fm). Como consecuencia, se espera que el comportamiento de ^{6}He difiera de la pura dispersión de Rutherford a distancia mayores que el ^{8}He. En la representación del ratio experimental $d\sigma_{elastic}/d\sigma_{Rutherford}$ frente a la distancia de máxima aproximación en trayectorias coulombianas puede observarse este efecto. Mientras que la desviación con respecto a Rutherford para el ^{6}He se hace evidente a grandes distancias ($\sim$20 fm), en el caso del ^{8}He, ocurre aproximadamente a 17 fm.

Esta representación es interesante también en otro sentido. Para el ^{6}He se ha encontrado que existe un tendencia sistemática en la distribución angular de la sección eficaz elástica a diferentes energías en torno a la barrera de Coulomb, sugiriendo la existencia de una función universal capaz de describir este mecanismo como función de la distancia de máxima aproximación [91]. Este comportamiento sistemático se ha encontrado también para el ^{8}He.

Se ha presentado además, para la dispersión elástica, un cálculo CRC teniendo en cuenta el acoplamiento con el canal de transferencia ^{208}Pb(^{8}He,^{7}He)^{209}Pb. Este cálculo es capaz de reproducir los datos elásticos suficientemente sin necesidad de un Potencial de Polarización Dipolar (DPP). En comparación con el ^{6}He, este resultado sugiere que los efectos dipolares, que eran importantes y responsables parcialmente del largo rango de absorción de este núcleo halo, son mucho menores para el ^{8}He.

Para ajustar los datos elástico a 16 MeV, las profundidades de los potenciales ópticos obtenidos para 22 MeV han sido modificadas. Se ha encontrado que la variación de la profundidad de la parte real (V) no afecta el ajuste de Modelo Óptico. Sin

embargo, la profundidad del potencial imaginario (W) aumenta. El comportamiento opuesto fue encontrado para el ^{6}He [26] donde W seguía una tendencia decreciente para energías decrecientes. El mismo efecto que para el ^{8}He había sido observado anteriormente para ^{6}Li [93] sugiriendo que los efectos de ruptura estaban todavía presentes a energías por debajo de la barrera. Para el ^{8}He ésta podría ser también la explicación, es decir que los mecanismos de ruptura se mantuvieran fuertes a estas energías.

Para la interpretación del ratio experimental ^{6}He/^{8}He se han llevado a cabo dos cálculos en el marco del DWBA (Distorted Wave Bron Approximation): cálculos para la transferencia de uno y de dos neutrones. En el segundo caso, se ha considerado un modelo simplificado en el que ambos neutrones son transferidos juntos como un di-neutron. Los cálculos de transferencia de dos neutrones, adecuadamente normalizados, se han sumado a los de transferencia de un neutrón.

Para 22 MeV, los cálculos considerando la transferencia de uno y dos neutrones reproducen el ratio experimental ^{6}He/^{8}He en ángulos mayores de 75°. Para ángulos menores, estas contribuciones no son suficientes para explicar los datos y el proceso de ruptura comienza a ser relevante, haciéndose dominante en ángulos muy delanteros. Para 16 MeV, los cálculos de transferencia son suficientes para reproducir los datos en ángulos mayores, por encima de 100°. Como cabría esperar, los mecanismo de transferencia son menos probables a medida que la energía disminuye puesto que para que ocurran los núcleos deben encontrarse suficientemente cerca. Además, para la energía por debajo de la barrera, la producción de ^{6}He es todavía importante indicando un rol importante de la ruptura.

Las distribuciones angulares del ratio ^{6}He/^{8}He a ambas energías, 16 y 22 MeV, presentan un cambio de tendencia como consecuencia de la aparición de los mecanismos de transferencia. El ángulo al que corresponde dicho cambio de tendencia, a pesar de ser distinto para cada energía, correponde al mismo valor de la distancia de máxima aproximación, $\sim$23 fm, que puede entenderse como la distancia a partir de la cual la transferencia comienza a ser relevante, con independencia de la energía de colisión.

Para la interpretación del ratio experimental ^{4}He/^{8}He se han considerado los cálculos DWBA de transferencia de dos neutrones a un estado excitado del ^{6}He. Se ha encontrado que, a ambas energías, los cálculos subestiman los datos en un factor en torno a 10.000. Sin embargo, multiplicando por este factor la forma de las distribuciones experimentales puede ser en parte reproducida. Para 22 MeV, a partir de 75°, la producción de ^{4}He puede explicarse mediante mecanismos de transferencia mientras que para ángulos menores los procesos de ruptura son relevantes. En el caso de 16 MeV, la producción de ^{4}He puede explicarse en gran medida mediante la ruptura, puesto que la transferencia es menos importante a esta energía. De hecho, el cambio de tendencia de la distribución a 22 MeV implica, para 16 MeV, que los mecanismos de transferencia comienzan a ser relevantes para ángulos mayores de 85°.

En general se ha realizado una interpretación preliminar de los datos experimentales mediante modelos simples. En un futuro próximo se realizarán estudios más detallados empleando para ello cálculos CDCC y cálculos CRC más refinados.

A

ROOT sorting code dedicated to obtain useful spectra

In this appendix, an example of the code written in ROOT in order to obtain the spectrum for a pixel in a 40 μm detector and a specific pixel in the 1 mm detector is presented. Once the spectra related to this pixel in ΔE and several pixels in E are available, they are summed up, generating the two-dimensional spectrum for the pixel in the thin detector. At this point, the necessity of a good energy calibration becomes evident.

The following example corresponds to the piece of code necessary to obtain the two-dimensional spectrum for the pixel determined by $ADC40p = 46$ and $ADC40n = 57$ considering the pixel in the E detector given by $ADC1000p = 238$ and $ADC1000n = 249$, which is the one right behind. The calibrations correspond to 22 MeV.

```
chain.Draw("2.61*adc46-472.31:2.61*adc46-472.31+9.78*adc238-664.88>>h12" ,
          abs((2.61*adc46-472.31)-(3.14*adc57-494.53)) < 300.00 &&
        "2.61*adc46-472.31 > 500.00 && 3.14*adc57-494.53 > 500.00 &&
          abs((9.78*adc238-664.88)-(9.48*adc249-861.37))<500.00 &&
((2.57*adc48-369.79)<450.00 && (2.61*adc47-507.03)<400.00 && (2.58*adc45-339.96)<450.00 &&
 (2.53*adc44-447.48)<400.00 && (2.61*adc43-396.22)<450.00 && (2.54*adc42-426.05)<350.00 &&
 (2.60*adc41-364.40)<400.00 && (2.48*adc40-341.06)<400.00 && (2.54*adc39-377.71)<450.00 &&
 (2.54*adc38-415.04)<400.00 && (2.56*adc37-408.18)<400.00 && (2.45*adc36-316.68)<400.00 &&
 (2.54*adc35-276.66)<450.00 && (2.52*adc34-365.10)<400.00 && (2.56*adc33-340.72)<450.00 &&
 (2.92*adc49-386.19)<550.00 && (2.56*adc50-314.05)<600.00 && (2.82*adc52-382.33)<500.00 &&
 (2.87*adc53-393.41)<500.00 && (2.82*adc54-424.77)<450.00 && (2.67*adc55-360.95)<550.00 &&
 (2.83*adc56-456.78)<500.00 && (2.86*adc58-464.13)<500.00 && (2.83*adc59-398.90)<450.00 &&
 (2.68*adc60-419.01)<450.00 && (2.80*adc61-462.04)<500.00 && (2.91*adc62-460.29)<450.00 &&
(2.89*adc63-489.33)<450.00 && (2.71*adc64-127.93)<800.00 && (10.11*adc240-929.49)<900.00 &&
(10.01*adc239-649.00)<1100.00 && (9.76*adc237-785.25)<900.00 && (9.91*adc236-949.98)<700.00 &&
(9.16*adc235-718.70)<900.00 && (9.72*adc234-669.43)<1000.00 && (10.11*adc233-712.34)<1000.00 &&
(9.76*adc232-1037.27)<700.00 && (9.88*adc231-690.44)<1000.00 && (9.62*adc230-917.35)<700.00 &&
(9.73*adc229-636.48)<1000.00 && (9.96*adc228-465.29)<1200.00 && (9.59*adc227-802.61)<900.00 &&
 (9.98*adc226-782.44)<900.00 && (9.65*adc225-784.78)<900.00 && (9.84*adc241-594.35)<1100.00 &&
(9.43*adc242-479.11)<1100.00 && (9.72*adc243-1048.73)<600.00 && (9.75*adc244-942.85)<700.00 &&
 (9.40*adc245-856.34)<800.00 && (9.70*adc246-921.56)<700.00 && (9.95*adc247-762.6)<900.00 &&
 (9.27*adc248-650.1)<900.00 && (9.73*adc250-957.35)<700.00 && (9.49*adc251-612.1)<1000.00 &&
(9.28*adc252-535.96)<1100.00 && (9.22*adc253-996.53)<600.00 && (10.15*adc254-577.57)<1200.00 &&
            (9.58*adc255-919.66)<700.00 && (8.86*adc256-740.41)<800.00)");
```

The first line in the code corresponds to Eq. 3.1 and generates the basic two-

dimensional spectrum. The second line represents Eq. 3.2, which guarantees that the registered events in the spectrum are related to a specific scattering angle. In the third line, Eq. 3.3 is applied, with the aim of removing further non-physical events. The fourth line represents Eq. 3.4, which restricts the spectrum to the events registered by a specific pixel in the E detector and, from the fifth line, all the instructions in the code are dedicated to interstrip effects. In particular, all the strip different to the ones which define the pixels under study are kept below a certain value of energy.

B

Matching of simulations

As it was mentioned in 3.3.7, once the effective positions of the beam spot on target and the setup have been determined at 16 and 22 MeV, some simulations must be carried out in order to obtain the scattering and solid angles and the number N_R for each pixel. In particular, every simulation is restricted to a different part of the setup so a correct matching between them is necessary in order to properly simulate the whole setup.

The simulations are performed following the next steps. A first simulation, which will be used as a basis for the rest, is carried out for the first half of a forward telescope. Subsequently, another simulation is performed for the rest of this telescope, existing, nevertheless, a region of overlap between them. In this region of overlap, there are several pixels for which the ratio $d\sigma_{elastic}/d\sigma_{Rutherford}$ should be the same, regardless of the simulation. In order to achieve the same value of the ratio in all these pixels, a constant of matching should be introduced. Later, a third simulation is made including the last pixels (more backward ones) of the forward telescope, for which the ratio is already known, as well as part of the contiguous (the bottom telescope). A new constant of matching should be calculated between this simulation and the preceding. This procedure is repeated, taking always regions of overlap between simulations, allowing for the calculation of the various constants. The process finishes once the whole angular range of the setup is covered and, therefore, all the telescopes have been properly simulated. At this point, the ratio $d\sigma_{elastic}/d\sigma_{Rutherford}$ is known for all the pixels in the setup as well as the scattering and solid angles.

Regarding the calculation of the constants of matching, several pixels in the region of overlap between simulations are considered searching for a constant common to all of them. This constant, C, must be such that the difference between the ratios calculated from a first simulation and the ratios calculated from a second one, and multiplied by C, are minimum. With the aim of giving this constant a meaning, the next reasoning is followed. A first simulation, i, is taken as a reference, in which a number M^i of events are generated. These M^i events are restricted to a range of values for both θ and ϕ, i.e. $[\theta^{min}_{cm,i}, \theta^{max}_{cm,i}]$ and $[\phi^{min}_i, \phi^{max}_i]$ respectively. In the simulation a Rutherford cross section (as shown in equation B.1) is considered:

$$\frac{d\sigma}{d\Omega}\Big|^{cm}_{Rutherford} = k\frac{1}{E_{cm}^2}\frac{1}{\sin(\frac{\theta_{cm}}{2})}. \tag{B.1}$$

Consequently, there is a value for k, namely k^i, for which equation B.2 is accomplished:

$$M^i = k^i \int_{\theta^{min}_{cm,i}}^{\theta^{max}_{cm,i}} \int_{\phi_i^{min}}^{\phi_i^{max}} \frac{d\sigma}{d\Omega}\Big|^{cm}_{Rutherford} \sin(\theta) d\theta d\phi. \tag{B.2}$$

If a second simulation, j, is performed with a number of generated events M^j in a range of values for θ and ϕ as $[\theta^{min}_{cm,j}, \theta^{max}_{cm,j}]$ and $[\phi_j^{min}, \phi_j^{max}]$, a new value for k, k^j, is obtained. In order to make this second simulation comparable to the first, it should be multiplied by a factor which relates both simulations i and j. This factor, named as X^{ij} and calculated as shown in equation B.3, should be consistent with the constant C^{ij} obtained from the pixels in the region of overlap between simulations i and j.

$$X^{ij} = \frac{k^i}{k^j} \tag{B.3}$$

Once all the simulations required for obtaining the scattering and solid angles and the number N_R of events in all the pixels of the setup have been performed, the constants of matching have been calculated, both from the overlapping pixels and as a relation between the different k values. As an example, the results obtained for the matching of the four simulations summarized in table B.1 are presented in table B.2, showing a good agreement.

Simulation	Simulated telescopes	Number of events	Range θ	Range ϕ
1	B	4.000.000	15° - 40°	30° - 150°
2	B	4.000.000	30° - 55°	30° - 150°
3	B and F	4.000.000	40° - 70°	30° - 210°
4	F	4.000.000	55° - 90°	150° - 210°

Table B.1: *Relevant information corresponding to the four simulations involved in the calculation of the matching constants presented in table B.2.*

Matched simulations	C^{ij}	X^{ij}
1 and 2	4.920	4.898
1 and 3	6.101	6.068
1 and 4	14.886	14.913

Table B.2: *Constants of matching, evaluated both from the overlapping pixels (C^{ij}) and as a relation of the different k values (X^{ij}), obtained for the four simulations summarized in table B.1.*

C

Experimental elastic cross sections

In this appendix, the values obtained for the average normalised elastic cross section and the scattering angle, together with their uncertainties, for each one of the intervals in which the full covered angular range has been divided, are presented in Tables C.1 and C.2 for 22 MeV and C.3 and C.4 for 16 MeV.

^{8}He+^{208}Pb @ 22 MeV			
$\theta_{int}(^\circ)$	$\delta\theta_{int}(^\circ)$	$\frac{d\sigma(\theta_{int})}{d\sigma(\theta_{int})_{Ruth}}$	$\delta(\frac{d\sigma(\theta_{int})}{d\sigma(\theta_{int})_{Ruth}})$
21.16	1.56	0.9873	0.0020
24.60	1.68	1.0105	0.0023
27.80	1.70	1.0164	0.0028
31.07	1.69	1.0057	0.0036
34.26	1.68	1.0017	0.0041
37.24	1.67	0.9985	0.0044
40.22	1.63	0.9920	0.0052
43.47	1.59	0.9933	0.0054
47.00	1.56	0.9940	0.0063
50.46	1.51	0.9886	0.0076
53.66	1.45	0.9863	0.0091
56.76	1.41	0.9862	0.0110
59.66	1.45	0.9544	0.0151
62.69	1.47	0.9028	0.0146
66.19	1.50	0.8339	0.0139
69.83	1.50	0.7280	0.0150
73.34	1.50	0.6205	0.0150

Table C.1: *Values of the scattering angle and its uncertainty and the average normalised elastic cross section and its uncertainty for each interval at 22 MeV.*

^{8}He+^{208}Pb @ 22 MeV			
$\theta_{int}(^\circ)$	$\delta\theta_{int}(^\circ)$	$\frac{d\sigma(\theta_{int})}{d\sigma(\theta_{int})_{Ruth}}$	$\delta(\frac{d\sigma(\theta_{int})}{d\sigma(\theta_{int})_{Ruth}})$
76.61	1.49	0.5678	0.0171
79.55	1.47	0.5314	0.0178
82.39	1.44	0.4409	0.0169
85.64	1.37	0.3516	0.0140
88.38	1.33	0.3120	0.0103
92.01	1.33	0.2496	0.0093
94.91	1.36	0.2001	0.0142
97.80	1.40	0.1786	0.0142
101.06	1.42	0.1352	0.0111
104.88	1.44	0.1097	0.0095
108.73	1.45	0.0883	0.0115
111.58	1.44	0.0698	0.0107
114.33	1.44	0.0604	0.0107
117.38	1.43	0.0593	0.0098
120.50	1.39	0.0460	0.0096
124.56	2.65	0.0417	0.0061
128.90	2.99	0.0237	0.0035
134.83	3.16	0.0172	0.0030
141.84	3.32	0.0269	0.0042
148.46	3.32	0.0262	0.0042
154.79	3.23	0.0172	0.0042

Table C.2: *Continuation of Table C.1.*

^{8}He+^{208}Pb @ 16 MeV			
$\theta_{int}(^\circ)$	$\delta\theta_{int}(^\circ)$	$\frac{d\sigma(\theta_{int})}{d\sigma(\theta_{int})_{Ruth}}$	$\delta(\frac{d\sigma(\theta_{int})}{d\sigma(\theta_{int})_{Ruth}})$
21.06	1.54	0.9942	0.0023
24.53	1.67	1.0198	0.0026
27.79	1.68	1.0302	0.0033
30.87	1.68	1.0179	0.0041
34.15	1.69	1.0169	0.0045
37.22	1.66	1.0049	0.0053
40.20	1.63	0.9944	0.0061
43.43	1.60	1.0133	0.0066

Table C.3: *Values of the scattering angle and its uncertainty and the average normalised elastic cross section and its uncertainty for each interval at 16 MeV.*

^{8}He+^{208}Pb @ 16 MeV			
$\theta_{int}(^\circ)$	$\delta\theta_{int}(^\circ)$	$\frac{d\sigma(\theta_{int})}{d\sigma(\theta_{int})_{Ruth}}$	$\delta(\frac{d\sigma(\theta_{int})}{d\sigma(\theta_{int})_{Ruth}})$
46.85	1.55	0.9983	0.0076
50.23	1.51	1.0018	0.0093
53.49	1.46	0.9783	0.0099
57.01	1.39	0.9913	0.0133
61.33	1.43	0.9601	0.0256
63.42	1.47	1.0019	0.0292
65.63	1.46	1.0091	0.0223
69.04	1.47	0.9775	0.0200
72.64	1.48	0.9889	0.0225
76.30	1.46	0.9619	0.0244
79.69	1.44	1.0182	0.0308
82.48	1.42	0.9713	0.0318
85.17	1.38	0.9813	0.0339
88.07	1.32	0.9869	0.0208
91.98	1.32	0.9782	0.0227
95.04	1.39	0.9195	0.0372
97.84	1.42	0.9481	0.0395
100.86	1.45	0.8927	0.0385
104.19	1.46	0.8243	0.0354
107.71	1.47	0.9379	0.0373
111.55	1.47	0.9213	0.0425
114.65	1.46	0.9052	0.0487
117.47	1.45	0.9927	0.0519
120.64	1.43	0.9045	0.0466
123.35	1.40	0.8650	0.0385
126.72	1.46	0.8205	0.0340
130.00	1.50	0.8314	0.0343
133.33	1.56	0.7538	0.0337
136.70	1.59	0.7664	0.0334
139.91	1.64	0.7642	0.0374
142.82	1.68	0.7063	0.0366
146.09	1.70	0.7127	0.0487
149.21	1.69	0.8117	0.0567
152.55	1.69	0.7616	0.0534
155.79	1.67	0.6784	0.0444
158.53	1.53	0.6812	0.0667

Table C.4: *Continuation of Table C.3.*

D

Experimental ^{6}He/^{8}He and ^{4}He/^{8}He ratios

In this appendix, the values obtained for the ratio ^{6}He/^{8}He and the scattering angle (Lab.), together with their uncertainties, for each one of the intervals in which the full covered angular range has been divided, are presented in Tables D.1 and D.2 for 22 MeV and D.3 and D.4 for 16 MeV. The values for the ratio ^{4}He/^{8}He are presented Tables D.5 and D.6 for 22 MeV and D.7 and D.8 for 16 MeV.

Ratio ^{6}He/^{8}He @ 22 MeV			
$\theta_{int,lab}(^\circ)$	$\delta\theta_{int,lab}(^\circ)$	$\frac{^6He}{^8He}$	$\delta\left(\frac{^6He}{^8He}\right)$
20.39	1.56	0.0018	0.0001
23.71	1.68	0.0021	0.0001
26.81	1.70	0.0021	0.0001
29.97	1.69	0.0019	0.0001
33.06	1.68	0.0020	0.0002
35.94	1.67	0.0028	0.0002
38.84	1.63	0.0033	0.0003
42.00	1.59	0.0054	0.0004
45.43	1.56	0.0089	0.0006
48.80	1.51	0.0167	0.0010
51.93	1.45	0.0310	0.0016
54.95	1.41	0.0571	0.0025
57.79	1.45	0.0890	0.0052
60.77	1.47	0.1377	0.0067
64.21	1.50	0.2180	0.0090
67.78	1.50	0.3254	0.0142

Table D.1: *Values of the scattering angle and its uncertainty and the ratio ^{6}He/^{8}He and its uncertainty for each interval at 22 MeV.*

Ratio ^{6}He/^{8}He @ 22 MeV			
$\theta_{int,lab}(^\circ)$	$\delta\theta_{int,lab}(^\circ)$	$\frac{^6He}{^8He}$	$\delta\left(\frac{^6He}{^8He}\right)$
71.25	1.50	0.4424	0.0203
74.49	1.49	0.5452	0.0292
77.40	1.47	0.7164	0.0393
80.22	1.44	0.8444	0.0508
83.45	1.37	1.1892	0.0663
86.18	1.33	1.2724	0.0562
89.81	1.33	1.6070	0.0768
92.71	1.36	1.9671	0.1655
95.61	1.40	2.2189	0.2056
98.88	1.42	2.4826	0.2242
102.73	1.44	2.7871	0.2610
106.62	1.45	3.4308	0.4836
109.50	1.44	4.2143	0.6264
112.29	1.44	4.0256	0.7202
115.39	1.43	4.7955	0.7948
118.56	1.39	3.6944	0.6941
122.70	2.65	7.1538	1.0591
127.14	2.99	7.8507	1.0184
133.22	3.16	10.2917	1.5560
140.44	3.32	7.8367	1.1888
147.26	3.32	7.4651	1.2123
153.82	3.23	10.5500	2.4683

Table D.2: *Continuation of Table D.1.*

Ratio ^{6}He/^{8}He @ 16 MeV			
$\theta_{int,lab}(^\circ)$	$\delta\theta_{int,lab}(^\circ)$	$\frac{^6He}{^8He}$	$\delta\left(\frac{^6He}{^8He}\right)$
20.29	1.54	0.00089	0.00006
23.65	1.67	0.00084	0.00006
26.79	1.68	0.00105	0.00009
29.78	1.68	0.00135	0.00013
32.95	1.69	0.00105	0.00013
35.93	1.66	0.00171	0.00021
38.82	1.63	0.00117	0.00020

Table D.3: *Values of the scattering angle and its uncertainty and the ratio ^{6}He/^{8}He and its uncertainty for each interval at 16 MeV.*

Ratio ^{6}He/^{8}He @ 16 MeV			
$\theta_{int,lab}(^\circ)$	$\delta\theta_{int,lab}(^\circ)$	$\frac{^6He}{^8He}$	$\delta\left(\frac{^6He}{^8He}\right)$
41.96	1.60	0.00172	0.00026
45.29	1.55	0.00134	0.00027
48.58	1.51	0.00170	0.00037
51.75	1.46	0.00154	0.00038
55.20	1.39	0.00204	0.00059
59.43	1.43	0.00270	0.00135
61.49	1.47	0.00483	0.00198
63.66	1.46	0.00784	0.00191
67.01	1.47	0.00512	0.00142
70.56	1.48	0.00978	0.00220
74.18	1.46	0.00487	0.00173
77.53	1.44	0.01322	0.00343
80.31	1.42	0.01856	0.00441
82.98	1.38	0.02296	0.00519
85.87	1.32	0.01343	0.00243
89.78	1.32	0.02181	0.00340
92.83	1.39	0.04320	0.00849
95.64	1.42	0.04746	0.00918
98.69	1.45	0.04480	0.00916
102.03	1.46	0.06115	0.01080
105.59	1.47	0.06811	0.01061
109.47	1.47	0.06653	0.01196
112.62	1.46	0.09497	0.01704
115.48	1.45	0.10183	0.01712
118.71	1.43	0.10250	0.01681
121.47	1.40	0.11885	0.01503
124.91	1.46	0.14955	0.01611
128.27	1.50	0.15339	0.01615
131.69	1.56	0.18687	0.01932
135.15	1.59	0.19802	0.01979
138.45	1.64	0.26518	0.02606
141.44	1.68	0.21219	0.02410
144.82	1.70	0.25926	0.03477
148.04	1.69	0.23166	0.03319
151.50	1.69	0.24710	0.03449
154.85	1.67	0.26837	0.03298
157.69	1.53	0.29231	0.05391

Table D.4: *Continuation of Table D.3.*

Ratio ^{4}He/^{8}He @ 22 MeV			
$\theta_{int,lab}(^\circ)$	$\delta\theta_{int,lab}(^\circ)$	$\frac{^4He}{^8He}$	$\delta\left(\frac{^4He}{^8He}\right)$
20.39	1.56	0.0025	0.0001
23.71	1.68	0.0033	0.0001
26.81	1.70	0.0039	0.0001
29.97	1.69	0.0045	0.0002
33.06	1.68	0.0047	0.0002
35.94	1.67	0.0055	0.0003
38.84	1.63	0.0064	0.0004
42.00	1.59	0.0076	0.0004
45.43	1.56	0.0086	0.0006
48.80	1.51	0.0095	0.0007
51.93	1.45	0.0125	0.0010
54.95	1.41	0.0154	0.0013
57.79	1.45	0.0238	0.0026
60.77	1.47	0.0367	0.0033
64.21	1.50	0.0495	0.0040
67.78	1.50	0.0740	0.0061
71.25	1.50	0.1146	0.0091
74.49	1.49	0.1563	0.0135
77.40	1.47	0.1920	0.0169
80.22	1.44	0.2550	0.0230
83.45	1.37	0.4409	0.0328
86.18	1.33	0.4333	0.0261
89.81	1.33	0.7239	0.0419
92.71	1.36	0.8920	0.0890
95.61	1.40	1.2071	0.1256
98.88	1.42	1.4360	0.1426
102.73	1.44	1.7871	0.1793
106.62	1.45	2.4769	0.3640
109.50	1.44	2.7679	0.4315
112.29	1.44	3.6667	0.6624
115.39	1.43	4.4545	0.7431
118.56	1.39	3.6944	0.6941
122.70	2.65	6.9615	1.0324
127.14	2.99	9.0597	1.1663
133.22	3.16	11.7708	1.7697

Table D.5: *Values of the scattering angle and its uncertainty and the ratio $^{4}He/^{8}He$ and its uncertainty for each interval at 22 MeV.*

Ratio ^{4}He/^{8}He @ 22 MeV			
$\theta_{int,lab}(^\circ)$	$\delta\theta_{int,lab}(^\circ)$	$\frac{^4He}{^8He}$	$\delta\left(\frac{^4He}{^8He}\right)$
140.44	3.32	10.4694	1.5654
147.26	3.32	11.3023	1.7982
153.82	3.23	16.1500	3.7214

Table D.6: *Continuation of Table D.5.*

Ratio ^{4}He/^{8}He @ 16 MeV			
$\theta_{int,lab}(^\circ)$	$\delta\theta_{int,lab}(^\circ)$	$\frac{^4He}{^8He}$	$\delta\left(\frac{^4He}{^8He}\right)$
20.29	1.54	0.00100	0.00006
23.65	1.67	0.00135	0.00008
26.79	1.68	0.00148	0.00011
29.78	1.68	0.00193	0.00015
32.95	1.69	0.00190	0.00017
35.93	1.66	0.00255	0.00026
38.82	1.63	0.00264	0.00030
41.96	1.60	0.00222	0.00029
45.29	1.55	0.00289	0.00039
48.58	1.51	0.00413	0.00058
51.75	1.46	0.00317	0.00055
55.20	1.39	0.00187	0.00056
59.43	1.43	0.00945	0.00254
61.49	1.47	0.00403	0.00180
63.66	1.46	0.00369	0.00131
67.01	1.47	0.00276	0.00104
70.56	1.48	0.00489	0.00155
74.18	1.46	0.00183	0.00106
77.53	1.44	0.00352	0.00177
80.31	1.42	0.00309	0.00179
82.98	1.38	0.00459	0.00230
85.87	1.32	0.00823	0.00190
89.78	1.32	0.00623	0.00180
92.83	1.39	0.00960	0.00394
95.64	1.42	0.00847	0.00381
98.69	1.45	0.01075	0.00441

Table D.7: *Values of the scattering angle and its uncertainty and the ratio $^4He/^8He$ and its uncertainty for each interval at 16 MeV.*

Ratio ^{4}He/^{8}He @ 16 MeV			
$\theta_{int,lab}(^\circ)$	$\delta\theta_{int,lab}(^\circ)$	$\frac{^4He}{^8He}$	$\delta\left(\frac{^4He}{^8He}\right)$
102.03	1.46	0.01799	0.00574
105.59	1.47	0.01238	0.00441
109.47	1.47	0.00403	0.00286
112.62	1.46	0.01397	0.00629
115.48	1.45	0.00783	0.00454
118.71	1.43	0.00750	0.00435
121.47	1.40	0.00679	0.00341
124.91	1.46	0.01360	0.00456
128.27	1.50	0.01327	0.00445
131.69	1.56	0.01010	0.00414
135.15	1.59	0.02805	0.00690
138.45	1.64	0.02834	0.00768
141.44	1.68	0.01806	0.00644
144.82	1.70	0.03333	0.01129
148.04	1.69	0.01158	0.00673
151.50	1.69	0.04633	0.01368
154.85	1.67	0.02875	0.00972
157.69	1.53	0.04615	0.01927

Table D.8: *Continuation of Table D.7.*

Bibliography

[1] National Nuclear Data Center. *http://www.nndc.bnl.gov*.

[2] M. Pfützner, M. Karny, L.V. Grigorenko, and K. Riisager. *Rev. Mod. Phys.*, 84:567–619, 2012.

[3] G. Pfennig, C. Normand, J. Magill, T. Fanghaenel, and G. Weber. *Karlsruher Nuklidkarte. Commemoration of the 50th Anniversary.* European Commission - Joint Research Centre - Institute for Transuranium Elements, 2008.

[4] G.R. Satchler. *Introduction to Nuclear Reactions.* MacMillan Education LTD, 1980.

[5] W.U. Schröder and R. Huizenga. *Treatise on Heavy Ion Science.* Plenum, New York, D.A. Bromley, 1984.

[6] A.C.C. Villari and J.R.J. Bennett. *C. R. Physique*, 4:595–608, 2003.

[7] A. Ozawa, T. Suzuki, and I. Tanihata. *Nucl. Phys.*, A693:32–62, 2001.

[8] I. Tanihata, H. Hagamaki, O. Hashimoto, Y. Shida, N. Yoshikawa, K. Sugimoto, O. Yamakawa, T. Kobayashi, and N. Takahashi. *Phys. Rev. Lett.*, 55:2676, 1985.

[9] I. Tanihata, H. Hamagaki, O. Hashimoto, S. Nagamiya, Y. Shida, N. Yoshikawa, O. Yamakawa, K. Sugimoto, T. Kobayashi, D.E. Greiner, N. Takahashi, and Y. Nojiri. *Phys. Lett.*, B160:380, 1985.

[10] I. Tanihata, D. Hirata, T. Kobayashi, S. Shimoura, K. Sugimoto, and H. Toki. *Phys. Lett.*, B289:261, 1992.

[11] D. Cortina-Gil, T. Baumann, H. Geissel, H. Lenske, K. Sümmerer, L. Axelsson, U. Bergmann, M.J.G. Borge, L.M. Fraile, M. Hellström, M. Ivanov, N. Iwasa, R. Janik, B. Jonson, K. Markenroth, G. Münzenberg, F. Nickel, T. Nilsson, A. Ozawa, K. Riisager, G. Schrieder, W. Schwab, H. Simon, C. Scheidenberger, B. Sitar, T. Suzuki, and M. Winkler. *Eur. Phys. J.*, A10:49–56, 2001.

[12] G.D. Alkhazov, A.V. Dobrovolsky, P. Egelhof, H. Geissel, H. Irnich, A.V. Khanzadeev, G.A. Korolev, A.A. Lobodenko, G. Münzenberg, M. Mutterer, S.R. Neumaier, W. Schwab, D.M. Seliverstov, T. Suzuki, and A.A. Vorobyov. *Nucl. Phys.*, A712:269–299, 2002.

[13] N.A. Orr. *Nucl. Phys.*, A616:155–168, 1997.

[14] M.J.G.Borge, U.C. Bergmann, R. Boutami, J. Cederkäll, P. Dendooven, L.M. Fraile, H.O.U. Fynbo, W.X. Huang, J. Huikari, Y. Jading, H. Jeppesen, A. Jokinen, B. Jonson, I. Martel, M. Meister, T. Nilsson, G. Nyman, Y. Prezado, K. Riisager, O. Tengblad, L. Weissman, K. Wilhelmsen, and J. Äystö. *Nucl. Phys.*, A746:243c–247c, 2004.

[15] H.-Jürgen Kluge. *Nucl. Phys.*, A701:495c–502c, 2002.

[16] O. Sorlin and M.G. Porquet. *Progress in Part. and Nucl. Phys.*, 61:602–673, 2008.

[17] P.G. Hansen and B. Jonson. *Europhys. Lett.*, 4:409, 1987.

[18] B. Jonson. *Phys. Rep.*, 389:1–59, 2004.

[19] T. Frederico, A. Delfino, L. Tomio, and M.T. Yamashita. *Progress in Part. and Nucl. Phys.*, 67:939, 2012.

[20] I. Tanihata, H. Savajols, and R. Kanungo. *Progress in Part. and Nucl. Phys.*, 68:215–313, 2013.

[21] T. Kobayashi, O. Yamakawa, K. Omata, K. Sugimoto, T. Shimoda, N. Takahashi, and I. Tanihata. *Phys. Rev. Lett.*, 60:2599–2602, 1988.

[22] I. Tanihata. *Treatise on Heavy-Ion Science Vol.8*. Ed. by Allan Bromdey (Plenum Publ.), 1989.

[23] A.S. Goldhaber. *Phys. Lett.*, B53:306, 1974.

[24] T. Kobayashi. *Nucl. Phys.*, A538:343c–352c, 1992.

[25] L. Acosta, A.M. Sánchez-Benítez, M.E. Gómez, I. Martel, F. Pérez-Bernal, F. Pizarro, J. Rodríguez-Quintero, K. Rusek, M.A.G. Alvarez, M.V. Andrés, J.M. Espino, J.P. Fernández-García, J. Gómez-Camacho, A.M. Moro, C. Angulo, J. Cabrera, E. Casarejos, P. Demaret, M.J.G. Borge, D. Escrig, O. Tengblad, S. Cherubini, P. Figuera, M. Gulino, M. Freer, C. Metelko, V. Ziman, R. Raabe, I. Mukha, D. Smirnov, O. R. Kakuee, and J. Rahighi. *Phys. Rev.*, C84:044604, 2011.

[26] A.M. Sánchez-Benítez, D. Escrig, M.A.G. Álvarez, M.V. Andrés, C. Angulo, M.J.G. Borge, J. Cabrera, S. Cherubini, P. Demaret, J.M. Espino, P. Figuera, M. Freer, J.E. García-Ramos, J. Gómez-Camacho, M. Gulino, O.R. Kakuee, I. Martel, C. Metelko, A.M. Moro, F. Pérez-Bernal, J. Rahighi, K. Rusek, D. Smirnov, O. Tengblad, P. Van Duppen, and V. Ziman. *Nucl. Phys.*, A803:30, 2008.

[27] M. Rodríguez-Gallardo, J.M. Arias, J. Gómez-Camacho, R.C. Johnson, A.M. Moro, I.J. Thompson, and J.A. Tostevin. *Phys. Rev.*, C77:064609, 2008.

[28] B. Jonson and K. Riisager. *Nucl. Phys.*, A693:77–89, 2001.

[29] T. Nilsson, G. Nyman, and K. Riisager. *Hyperfine interactions*, 129:67–81, 2000.

[30] R. Raabe, J. Büscher, J. Ponsaers, F. Aksouh, M. Huyse, O. Ivanov, S.R. Lesher, I. Mukha, D. Pauwels, M. Sawicka, D. Smirnov, I. Stefanescu, J. Van de Walle, P. Van Duppen, C. Angulo, J. Cabrera, N. de Séréville, I. Martel, A.M. Sánchez-Benítez, and C. Aa. Diget. *Phys. Rev.*, C80:054307, 2009.

[31] K. Hagino, A. Vitturi, C.H. Dasso, and S.M. Lenzi. *Phys. Rev.*, C61:037602, 2000.

[32] A. Lemasson, A. Navin, N. Keeley, M. Rejmund, S. Bhattacharyya, A. Shrivastava, D. Bazin, D. Beaumel, Y. Blumenfeld, A. Chatterjee, D. Gupta, G. de France, B. Jacquot, M. Labiche, R. Lemmon, V. Nanal, J. Nyberg, R.G. Pillay, R. Raabe, K. Ramachandran, J.A. Scarpaci, C. Simenel, I. Stefan, and C.N. Timis. *Phys. Rev.*, C82:044617, 2010.

[33] A. Lemasson, A. Navin, M. Rejmund, N. Keeley, V. Zelevinsky, S. Bhattacharyya, A. Shrivastava, D. Bazin, D. Beaumel, Y. Blumenfeld, A. Chatterjee, D. Gupta, G. de France, B. Jacquot, M. Labiche, R. Lemmon, V. Nanal, J. Nyberg, R.G. Pillay, R. Raabe, K. Ramachandran, J.A. Scarpaci, C. Schmitt, C. Simenel, I. Stefan, and C.N. Timis. *Phys. Lett.*, B697:454, 2011.

[34] TUNL Nuclear Data Evaluation. *http://www.tunl.duke.edu/nucldata/*.

[35] Ł. Standylo, L. Acosta, C. Angulo, R. Berjillos, J.A. Duenas, M.S. Golovkov, N. Keeley, T. Keutgen, I. Martel, M. Mazzocco, F. Pérez-Bernal, A.M. Sánchez-Benítez, C. Signorini, M. Romoli, K. Rusek, and R. Wolski. *Phys. Rev.*, C87:064603, 2013.

[36] Y. Iwata, K. Ieki, A. Galonsky, J.J. Kruse, J. Wang, R.H. White-Stevens, E. Tryggestad, P.D. Zecher, F. Deák, Á. Horváth, Á. Kiss, Z. Seres, J.J. Kolata, J. von Schwarzenberg, R.E. Warner, and H. Schelinet. *Phys. Rev.*, C62:064311, 2000.

[37] Y. Ogawa, K. Yabana, and Y. Suzuki. *Nucl. Phys.*, A543:722, 1992.

[38] J. A. Tostevin, J.S. Al-Khalili, M. Zahar, M. Belbot, J.J. Kolata, K. Lamkin, D.J. Morrisey, M. Sherrill, M. Lewitowicz, and A.H. Wuosmaa. *Phys. Rev.*, C56:R2929, 1997.

[39] M. V. Zhukov, A.A. Korsheninnikov, and M.H. Smedberg. *Phys. Rev.*, C50:R1, 1994.

[40] L.V. Chulkov, F. Aksouh, A. Bleile, O.V. Bochkarev, D. Cortina-Gil, A.V. Dobrovolsky, P. Egelhof, H. Geissel, M. Hellström, N.B. Isaev, O.A. Kiselev, B.G. Komkov, M. Matos, F.N. Moroz, G. Münzenberg, M. Mutterer, V.A. Mylnikov, S.R. Neumaier, V.N. Pribora, D.M. Seliverstov, L.O. Sergeev, A. Shrivastava,

K. Sümmerer, S.Yu. Torilov, H. Weick, M. Winkler, and V.I. Yatsoura. *Nucl. Phys.*, A759:43–63, 2005.

[41] N. Keeley, F. Skaza, V. Lapoux, N. Alamanos, F. Auger, D. Beaumel, E. Becheva, Y. Blumenfeld, F. Delaunay, A. Drouart, A. Gillibert, L. Giot, K.W. Kemper, L. Nalpas, A. Pakou, E.C. Pollacco, R. Raabe, P. Roussel-Chomaz, K. Rusek, J.A. Scarpaci, J.L. Sida, S. Stepantsov, and R. Wolski. *Phys. Lett.*, B646:222, 2007.

[42] S. Ilieva, F. Aksouh, G.D. Alkhazov, L. Chulkov, A.V. Dobrovolsky, P. Egelhof, H. Geissel, M. Gorska, A. Inglessi, R. Kanungo, A.V. Khanzadeev, O.A. Kiselev, G.A. Korolev, X.C. Le, Yu.A. Litvinov, C. Nociforo, D.M. Seliverstov, L.O. Sergeev, H. Simon, V.A. Volkov, A.A. Vorobyov, H. Weick, V.I. Yatsoura, and A.A. Zhdanov. *Nucl. Phys.*, A875:8–28, 2012.

[43] Zs. Podolyák, P.M. Walkera, H. Machb, G. de France, G. Slettend, F. Azaiez, J.M. Casandjian, B. Cederwall, D.M. Cullen, Zs. Dombradi, G.D. Dracoulis, L.M. Fraile, S. Franchoo, H. Fynbo, M. Gorska, Y. Kopatch, G.J. Lane, S. Mandal, L. Milechina, J. Molnar, C. O'Leary, W. Plociennik, V. Pucknell, P. Raddon, N. Redon, E. Ruchowska, M. Stanoiu, O. Tengblad, C. Wheldon, and R. Wood. *Nucl. Instr. and Meth. Phys. Res.*, A511:354–359, 2003.

[44] A. Navin, V. Tripathi, Y. Blumenfeld, V. Nanal, C. Simenel, J.M. Casandjian, G. de France, R. Raabe, D. Bazin, A. Chatterjee, M. Dasgupta, S. Kailas, R.C. Lemmon, K. Mahata, R.G. Pillay, E.C. Pollacco, K. Ramachandran, M. Rejmund, A. Shrivastava, J.L. Sida, and E. Tryggestad. *Phys. Rev.*, C70:044601, 2004.

[45] A. Lemasson, A. Shrivastava, A. Navin, M. Rejmund, N. Keeley, V. Zelevinsky, S. Bhattacharyya, A. Chatterjee, G. de France, B. Jacquot, V. Nanal, R.G. Pillay, R. Raabe, and C. Schmitt. *Phys. Rev. Lett.*, 103:232701, 2009.

[46] I. Martel and K. Rusek et al. Near barrier scattering of ^{8}he with heavy targets. *Proposal of experiment E875S, presented at GANIL PAC in 2008.*

[47] G.R. Satchler. *Direct Nuclear Reactions.* Clarendon Press, Oxford, 1983.

[48] Carlos A. Bertulani. *Nuclear Physics in a Nutshell.* Princeton University Press, 2007.

[49] I.J. Thompson. *Compt. Phys. Rep.*, 7:167, 1988.

[50] G.R. Satchler and W.G. Love. *Phys. Rep.*, 55:183–254, 1979.

[51] N. Keeley, N. Alamanos, K.W. Kemper, and K. Rusek. *Progress in Part. and Nucl. Phys.*, 63:396–447, 2009.

[52] J.P. Fernández García. *PhD Thesis at the Universidad de Sevilla, Spain*, 2012.

[53] Grand Accélérateur Nacional d'Ions Lourds GANIL. *http://www.ganil-spiral2.eu/spiral2.*

[54] F. Chautard. Operation status of high intensity ion beams at ganil. *Proceedings of HIAT09, Venice, Italy*, 2009.

[55] A.C.C. Villari and The Spiral Group. *Nucl. Phys.*, A693:465, 2001.

[56] L. Maunoury et al. *18th Int. Workshop on ECR Ion Sources Proceedings, College Station, TX, USA*, 1997.

[57] M. Lieuvin et al. Commisioning of spiral, the ganil radioactive facility. *Proceedings of the 18th Int. Conference on Cyclotrons and their Applications, East Lansing, Michigan*, 2001.

[58] O. Skeppstedt, H.A. Roth, L. Lindström, R. Wadsworth, I. Hibbert, N. Kelsall, D. Jenkins, H. Grawe, M. Gorska, M. Moszyński, Z. Sujkowski, D. Wolski, M. Kapusta, M. Hellström, S. Kalogeropoulos, D. Oner, A. Johnson, J. Cederkäll, W. Klamra, J. Nyberg, M. Weiszflog, J. Kay, R. Griffiths, J. Garces Narro, C. Pearson, and J. Eberth. *Nucl. Instr. and Meth. Phys. Res.*, A421:531, 1999.

[59] F. Azaiez. *Nucl. Phys.*, A654:1003c, 1999.

[60] G. Marquínez-Durán, L. Acosta, R. Berjillos, J.A. Due nas, J.A. Labrador, K. Rusek, A.M. Sánchez-Benítez, and I. Martel. *Nucl. Instr. and Meth. Phys. Res.*, A755:69–77, 2014.

[61] Y. Blumenfeld, F. Auger, J.E. Sauvestre, F. Marechal, S. Ottini, N. Alamanos, A. Barbier, D. Beaumel, B. Bonnereau, D. Charlet, J.F. Clavelin, P. Courtat, P. Delbourgo-Salvador, R. Douet, M. Engrand, T. Ethvignot, A. Gillibert, E. Khan, V. Lapoux, A. Lagoyannis, L. Lavergne, S. Lebon, P. Lelong, A. Lesage, V. Le Ven, I. Lhenry, J.M. Martin, A. Musumarra, S. Pita, L. Petizon, E. Pollacco, J. Pouthas, A. Richard, D. Rougier, D. Santonocito, J.A. Scarpaci, J.L. Sida, C. Soulet, J.S. Stutzmann, T. Suomijarvi, M. Szmigiel, P. Volkov, and G. Voltolini. *Nucl. Instr. and Meth. Phys. Res.*, A421:471, 1999.

[62] E. Pollacco, D. Beaumel, P. Roussel-Chomaz, E. Atkin, P. Baron, J.P. Baronick, E. Becheva, Y. Blumenfeld, A. Boujrad, A. Drouart, F. Druillole, P. Edelbruck, M. Gelin, A. Gillibert, Ch. Houarner, V. Lapoux, L. Lavergne, G. Leberthe, L. Leterrier, V. Le Ven, F. Lugiez, L. Nalpas, L. Olivier, B. Paul, B. Raine, A. Richard, M. Rouger, F. Saillant, F. Skaza, M. Tripon, M. Vilmay, E. Wanlin, and M. Wittwer. *Europ. Phys. J*, A25:287–288, 2005.

[63] M. Labiche, W.N. Catford, R.C. Lemmon, C.N. Timis, R. Chapman, N.A. Orr, B. Fernández-Domínguez, G. Moores, N.L. Achouri, N. Amzal, S. Appleton, N.I. Ashwood, T.D. Baldwin, M. Burns, L. Caballero, J. Cacitti, J.M. Casadjian, M. Chartier, N. Curtis, K. Faiz, G. de France, M. Freer, J.M. Gautier, W. Gelletly, G. Iltis, B. Lecornu, X. Liang, C. Marry, Y. Merrer, L. Olivier, S.D. Pain, V.F.E. Pucknell, B. Raine, M. Rejmund, B. Rubio, F. Saillant, H. Savajols, O. Sorlin, K. Spohr, Ch. Theisen, G. Voltolini, and D.D. Warner. *Nucl. Instr. and Meth. Phys. Res.*, A614:439–448, 2010.

[64] Glenn F. Knoll. *Radiation Detection and Measurement.* John Wiley and Sons, New York, 1989.

[65] Micron Semiconductor. *http://www.micronsemiconductor.co.uk/.*

[66] O. Tengblad, U.C. Bergmann, L.M. Fraile, H.O.U. Fynbo, and S. Walsh. *Nucl. Instr. and Meth. Phys. Res.*, A525:458–464, 2004.

[67] Autocad. *http://www.autodesk.es.*

[68] Catia. *http://www.3ds.com/products/catia.*

[69] S. Agostinelli, J. Allison, K. Amako, J. Apostolakis, H. Araujo, P. Arce, M. Asai, D. Axen, S. Banerjee, G. Barrand, F. Behner, L. Bellagamba, J. Boudreau, L. Broglia, A. Brunengo, H. Burkhardt, S. Chauvie, J. Chuma, R. Chytracek, G. Cooperman, G. Cosmo, P. Degtyarenko, A. Dell'Acqua, G. Depaola, D. Dietrich, R. Enami, A. Feliciello, C. Ferguson, H. Fesefeldt, G. Folger, F. Foppiano, A. Forti, S. Garelli, S. Giani, R. Giannitrapani, D. Gibin, and J.J. Gomez et al. *Nucl. Inst. and Meth. Phys. Res.*, A506:250–303, 2003.

[70] J. Allison, K. Amako, J. Apostolakis, H. Araujo, P.A. Dubois, M. Asai, G. Barrand, R. Capra, S. Chauvie, R. Chytracek, G.A.P. Cirrone, G. Cooperman, G. Cosmo, G. Cuttone, G.G. Daquino, M. Donszelmann, M. Dressel, G. Folger, F. Foppiano, J. Generowicz, V. Grichine, S. Guatelli, P. Gumplinger, A. Heikkinen, T. Hrivnacova, A. Howard, S. Incerti, V. Ivanchenko, T. Johnson, F. Jones, T. Koi, R. Kokoulin, M. Kossov, H. Kurashige, V. Lara, S. Larsson, F. Lei, O. Link, and F. Longo et al. Geant4: A toolkit for the simulation of the passage of particles. *IEEE Transactions on Nuclear Science*, 53:270–278, 2006.

[71] Geant4. *http://geant4.cern.ch.*

[72] IPN Orsay. The nptool package.

[73] R.A. Winyard, J.E. Lutkin, and G.W. McBeth. *Nucl. Instr. and Meth. Phys. Res.*, 95:141–153, 1971.

[74] S. Barlini, R. Bougault, Ph. Laborie, O. Lopez, D. Mercier, M. Parlog, B. Tamain, E. Vient, E. Chevallier, A. Chbihi, B. Jacquot, and V.L. Kravchuk for the FAZIA collaboration. *Nucl. Instr. and Meth. Phys. Res.*, A600:644–650, 2009.

[75] Canberra. *http://www.canberra.com/products/detectors/pips-detectors-particle-identificati on.asp.*

[76] Mesytec GmbH and Co. KG. *http://www.mesytec.com/.*

[77] D. Cruz. *Master Thesis at the Universidad de Huelva, Spain*, 2010.

[78] NI LabVIEW. *http://www.ni.com/labview/esa/.*

[79] Caen S.p.A. *http://www.caen.it/csite/Product.jsp?parent=11Type=Product.*

[80] CES. Creative Electronic Systems SA. *http://www.ces.ch/technology/backward-compatible.*

[81] Helmholtzzentrum für Schwerionenforschung GSI. *https://www.gsi.de/.*

[82] ORTEC. *http://www.ortec-online.com/.*

[83] H. Laurent, H. Lefort, D. Beaumel, Y. Blumenfeld, S. Fortier, S. Gales, J. Guillot, J.C. Roynette, and P. Volkov. *Nucl. Instr. and Meth. Phys. Res.*, A326:517–525, 1993.

[84] M. Senoville. *PhD Thesis at the University of Caen, Basse-Normandie, France*, 2010.

[85] CERN Program Library Office. PAW++. *Physics Analysis Workstation.*

[86] ROOT Data Analysis Framework. *https://root.cern.ch/.*

[87] J.A. Duenas, D. Mengoni, M. Assie, B. Le Crom, A.M. Sánchez-Benítez, B. Genolini, Y. Blumenfeld, S. Ancelin, N. de Séréville, T. Faul, F. Hammache, A. Jallat, V. Le Ven, E. Rauly, D. Suzuky, D. Beaumel, and I. Martel. *Nucl. Instr. and Meth. Phys. Res.*, A743:44–50, 2014.

[88] D. Torresi, J. Forneris, L. Grassi, L. Acosta, A. Di Pietro, P. Figuera, L. Grilj, M. Jakšić, M. Lattuada, T. Mijatović, M. Milin, L. Prepolec, N. Skukan, N. Soić, D. Stanko, V. Tokić, M. Uroić, and M. Zadro. *J. Phys. Conf. Ser.*, 590:012029, 2015.

[89] Mathematica. *https://www.wolfram.com/mathematica/.*

[90] J. Cook. *Nucl. Phys.*, A388:153, 1982.

[91] I. Martel, E.F. Aguilera, L. Acosta, A.M. Sánchez-Benítez, and R. Wolski. *AIP Conf. Proc.*, 1423:89, 2011.

[92] N. Keeley. *Private communication.*

[93] N. Keeley, S.J. Bennett, N.M. Clarke, B.R. Fulton, G. Tungate, P.V. Drumm, M.A. Nagarajan, and J.S. Lilley. *Nucl. Phys.*, A571:326–336, 1994.

[94] F. Skaza, N. Keeley, V. Lapoux, N. Alamanos, F. Auger, D. Beaumel, E. Becheva, Y. Blumenfeld, F. Delaunay, A. Drouart, A. Gillibert, L. Giot, K.W. Kemper, R.S. Mackintosh, L. Nalpas, A. Pakou, E.C. Pollacco, R. Raabe, P. Roussel-Chomaz, J.A. Scarpaci, J.L. Sida, S. Stepantsov, and R. Wolski. *Phys. Lett.*, B619:82–87, 2005.

[95] D. G. Kovar, N. Stein, and C.K. Bockelman. *Nucl. Phys.*, A231:266–300, 1974.

[96] D.M. Brink. *Phys. Lett.*, B40:37–40, 1972.